UNIVERSITÀ DEGLI STUDI DI CATANIA
FACOLTÀ DI SCIENZE MATEMATICHE, FISICHE E NATURALI
DOTTORATO DI RICERCA IN FISICA – XXV CICLO

Paola Ballerini

EFFECTS OF STARSPOTS ACTIVITY ON OPTICAL AND NEAR INFRARED OBSERVATIONS OF PLANETARY TRANSITS

Ph.D. Thesis

Supervisor:
Prof. A.C. Lanzafame

Coordinator:
Prof. F. Riggi

Tutors:
Prof. I. Pagano
Prof. A.F. Lanza

---

anno accademico 2012/2013

Contents

Abstract

In this thesis, I report on the effects that magnetic stellar activity of solar-type stars induces on stellar light curves involved in the photometric technique for the detection and characterization of transiting extra-solar planets that is one of the most effective detection methods, the first being the radial velocity technique.

Stellar magnetic activity is a source of noise in the study of the transits of extra-solar planets since it induces flux variations that significantly affect the transit depth determination and the derivations of planetary and stellar parameters. Surface brightness inhomogeneities, such as starspots or bright faculae, on star disc have an intrinsic dependence on wavelength and thus on the stellar colours. The colour dependence of stellar activity may significantly influence the characterization of planetary atmospheres since it produces stellar flux variations that may mimic those due to the presence of molecular or atomic species in the transmitted planetary spectra. In this thesis I focus on the effects due essentially to stellar spots present in the visible hemisphere of solar-type stars. The proposed method is a theoretical one, aiming to predict the starspot-induced effects with the use of stellar atmospheric models and I present a systematic approach to quantify the corresponding stellar flux variations as a function of wavelength bands. Therefore I consider a star with spots covering a given fraction of its disc and model the variability in both the UBVRIJHK photometric system and the *Spitzer*/IRAC wavebands for dwarf stars from G to M spectral types. Then I compare starspot-induced flux variations in these different passbands with planetary transits and quantify how they affect the determination of the planetary radius and the analysis of the transmission spectroscopy in the study of planetary atmospheres. My results suggest that the monitoring of the systems by using broad-band photometry, from visible to infrared, helps to constrain spots effects by estimating the $\mathcal{R}$ parameter, i.e. the ratio of the relative variations in the stellar fluxes at short wavelength optical bands (e.g., U or B) to near-infrared ones (e.g., J or K). Its numerical value can be used to distinguish starspot brightness dips from planetary transits in a single stellar light curve.

In addition to the perturbations in the measurement of the planetary radius, the perturbations in the transit light curve profiles due to starspots can affect the determinations of orbital parameters, i.e., the relative semi-major axis and the

inclination of the planetary orbit, that are directly derived by fitting procedure of the transit light curves. These distortions in the transit light curves have a significant impact on the derivation of stellar parameters and, above all, on the stellar density thus bothering the stellar evolutionary estimates.

The results derived from the synthetic photometric analysis are presented and discussed in Ballerini et al. (2012).

Chapter 1

Introduction

The aim of this thesis is an analysis on how solar-like magnetic activity in stars hosting planets may affect the detection and characterization of extra-solar planets through the photometric transit technique. The study of stellar magnetic phenomena is crucial in searching for transiting exoplanets since they introduce systematic effects which may induce misleading estimates of observables required to properly characterize exoplanetary systems. These considerations may also be applied to our Sun which is not to be considered as a unique star with the right requirements for hosting planets. In this Chapter I will introduce magnetic activity, firstly focusing on our own star, the Sun, with its external atmosphere which in general is assumed as the starting point and the testing bench to understand the astrophysical behaviour of the other stars' external atmosphere. I will also describe the observed magnetic activity in other stars and how it may perturb the photometric transit of an extra-solar planet.

1.1. The Sun: general properties

The Sun is classified as a G2V main-sequence star based on the spectral classfication[1]. If we look at the Hertzsprung-Russell (H-R) diagram (see Fig. 1.1), it is placed in the middle of the main-sequence band, where typically the yellow and red stars are located, and from this position we can directly derive some important properties. The Sun has a surface temperature of about 5778 K, and this is equivalent to say that it is a G2V (the label "V" refers to main-sequence

---

[1] Stars are classified on the basis of which elements are prominent in their spectra and this depends on their temperature and the popolation of those elements in the right level of ionisation or excitation.

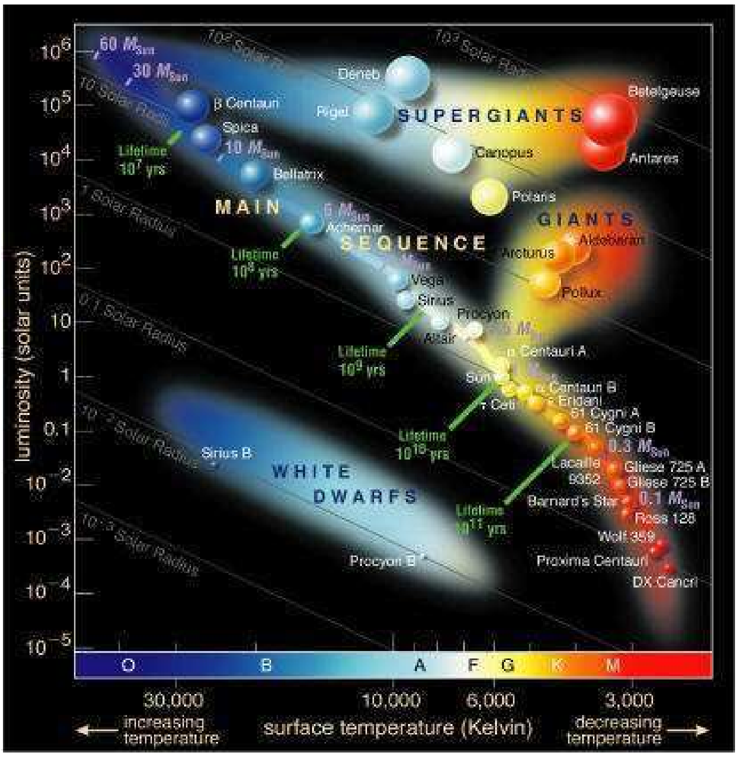

Figure 1.1: Hertzsprung-Russell diagram: luminosity, in solar units, vs. surface temperature. The diagram is dominated by the *main-sequence* band, which runs across the plot from the left top (blue stars) to the right bottom (red stars) and is crowded by stars in their hydrogen burning stage, and the *giant branch* filled by red massive stars. Other stars are clustered in the supergiants (horizontal and above the giant branch) and white dwarfs branch (parallel and below the main-sequence). In the diagram are also reported the stellar radii and masses, in solar units, and their lifetimes. The spectral types of stars are reported along the abscissa axis related to the corresponding surface temperature.

stars), a bolometric absolute magnitude[2] of about 4.72 and a luminosity $L_\odot$ =

---

[2] The *bolometric absolute magnitude* M_{bol} is the bolometric apparent magnitude of the star m_{bol}, located at a distance of 10 parsec from the Sun. In general at a wavelength λ, it is computed by the relation

$$M_\lambda = m_\lambda + 5 - 5\ log\ d,$$

where m_λ is the apparent magnitude of a star (i.e. a measure of the luminosity of a star as seen by an observer) at wavelenght λ and d is the distance of the star in parsec. M_{bol} is obtained by integrating the previous relation over all wavelengths. In general magnitudes are measured through filters which permit only certain wavelength bands to enter the detector. For example, standard filter systems are used, such as UBV (Johnson photometric system), where U (ultraviolet) indicates the permission of wavelengths covering the range [300 − 400] nm, B (blue) allows wavelengths in the range [360 − 550] nm, and V (visual) in the range [480 − 680]

$3.9{\cdot}10^{26}$ W (Karttunen et al. 2003). Due to its proximity to the Earth (mean distance $a = 1.496{\cdot}10^{11}$ m) and to its luminosity it can be studied in great details but however not all solar phenomena are still clearly understood.

The interior structure of the Sun is inferred thanks to the study of the propagation of waves on the Sun surface (helioseismology, Thompson 2004) which provides a detailed map of the inner part of the Sun, whose structure is reported in Fig. 1.2, showing an internal core, a radiative zone and a convective envelope where the energy is transported towards the outer parts and its atmosphere.

- The core is the innermost region which occupies about the $20 - 25\%$ of the solar radius[3] (García et al. 2007), where the production of energy through the nuclear burning of hydrogen occurs (i.e. the proton-proton chain, which is the principal source of energy for low-mass main-sequence stars, Karttunen et al. 2003).

- The radiative zone extends from the core to about 0.7 $R_\odot$ and within this layer the energy is transported through the propagation of radiation (Karttunen et al. 2003).

- The convective envelope extends from the radiative region up to near 1 $R_\odot$ (Christensen-Dalsgaard et al. 1991). Within this zone the lower temperatures and densities prevent the energy transport through radiation, being convective motion more effective (Karttunen et al. 2003).

The study of the solar atmosphere is crucial for the understanding of the astrophysical behaviour of those stars which show solar-like gross properties, i.e. lower main-sequence stars with shallower convective envelopes and cyclic solar-like magnetic variability.

1.2. The solar atmosphere

The solar atmosphere is the domain from which electromagnetic radiation is received. It is composed by the external layers reported in the Fig. 1.2: *photosphere*, *chromosphere*, *transition region* (which is a very thin region, not represented in the picture, separating chromosphere and corona), and *corona*. There

---

nm. There exist other photometric system (Cousin: RI, Strömgren: uvby, and so on). The apparent magnitudes observed through filters UBV are called U, B, V, similarly for Cousin and Strömgren systems (i.e. R, I, u, v, b, y magnitudes and so on). The difference between two magnitudes is defined as colour index. For instance, in the Johnson system U-B and B-V are colour indexes (Karttunen et al. 2003).

[3] The solar radius is: $R_\odot = 6.95{\cdot}10^8$ m (Cox 2000).

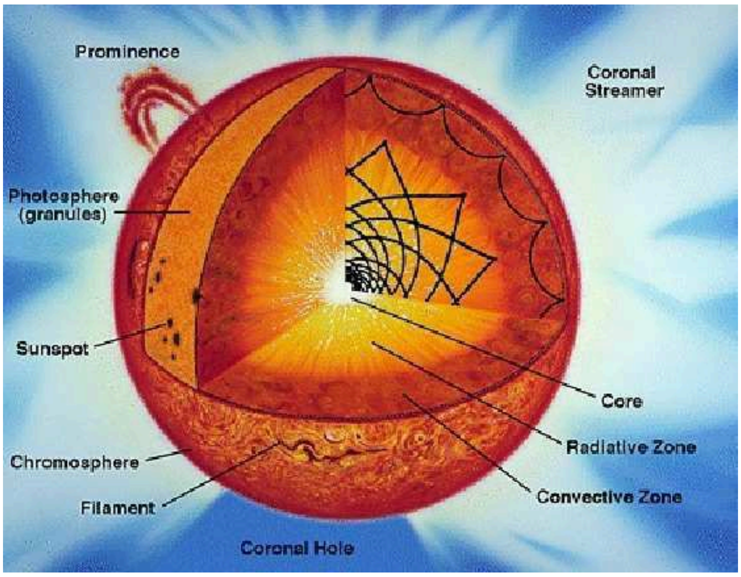

Figure 1.2: The internal and external structure of the Sun, starting with the hot core ending with the hot corona. This is also a typical structure for solar-type stars which, above the core, are expected to have a radiative one and a convective envelope, where the radiation is transported outwards, then the outer layers (photosphere, chromosphere, and corona), where we may find the most prominent manifestations of the solar and stellar activity: spots, faculae, filaments and active regions in general (some of them are reported). This picture is taken by http://hpde.gsfc.nasa.gov/LWS_Space_Weather/SpaceWeatherOverview.html.

exists a gradient of temperature from the inner to the outer layers, the temperature increases with the height above the photosphere and thus the emission of each layer is radiated in different wavelength ranges, as can be seen in Fig. 1.3. In other words, the atmosphere is not in radiative equilibrium thus requiring a non-thermal heating source. The photosphere temperature is about 10^4 K and the corona temperature reaches 10^6 K. In addition all these layers are characterized by the signatures of the solar magnetic field, i.e. the *active regions*, that are parts of the solar surface where powerful magnetic fluxes come out. These regions exhibit different morphologies with peculiar features in each atmospheric layer. In the following I will give a brief description of the significant properties of each of these zones.

1.2.1. Photosphere

The *photosphere* is the innermost layer in the solar atmosphere with a thickness of few hundred of kilometers (Stix 1989, Karttunen et al. 2003). It is observable in white light (4000 Å $< \lambda < 7000$ Å) and represents the visible surface of the Sun thus most of the information about our star comes from this layer. Its

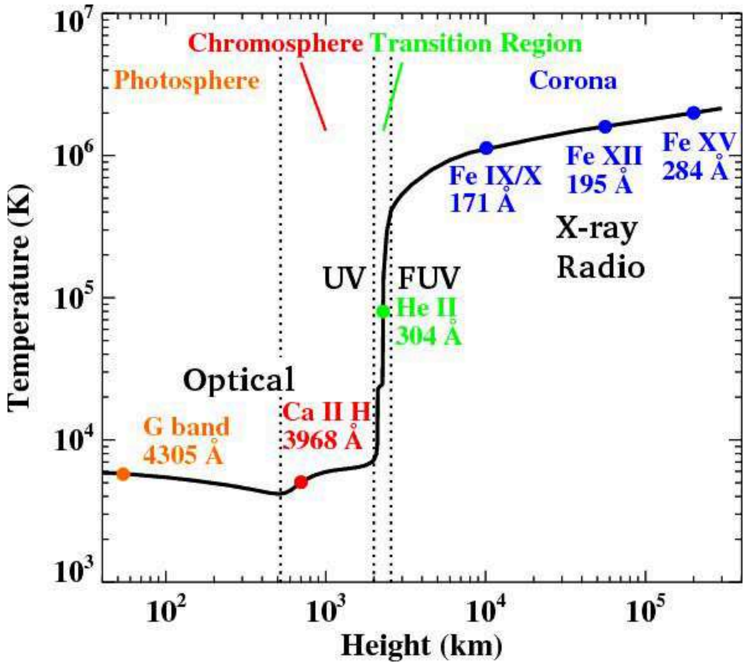

Figure 1.3: Temperature profile of the solar atmosphere above the $\tau_{5000} = 1$ (optical depth unity in the continuum at 5000 Å) surface. The G-band (a molecular band due to electronic transitions from and to rotational and vibrational sublevels of the molecule CH at 4300 Å, Steiner et al. 2001) and Ca II H lines are emitted respectively in the lower photosphere and lower chromosphere. The peak formation temperatures of the He II (304 Å) line emitted in the transition region, and Fe IX/X (171 Å), Fe XII (195 Å), Fe XV (284 Å) lines, all emitted in the inner solar corona, are 80 000 K, 1.3 MK, 1.6 MK, 2.0 MK, respectively (Yang et al. 2009).

emission arises from a layer seen at 5000 Å, where the photosphere is opaque to radiation coming from the centre (Stix 1989). For this reason it is useful to define τ_{5000} as a reference optical depth[4] (Stix 1989, Schrijver & Zwaan 2000) and it is assumed equal to unity.

If we look at the Fig. 1.4, we may note that the photosphere is not uniformly illuminated and shows some peculiarities. First of all, the the *limb-darkening effect* which is caused by the existence of a temperature gradient in the atmosphere (Stix 1989). It depends on the angle of sight of the observer, θ. The penetration

---

[4] The optical depth is a measure of the opacity of medium, namely it represents the fraction of radiation, at a specified frequency ν, absorbed while passing in an opaque medium. It is defined as

$$\tau_\nu = \int_0^d \kappa_\nu \, \rho \, dz, \tag{1.1}$$

where κ_ν is the absorption coefficient per unit mass, ρ is the medium density and d is the medium thickness.

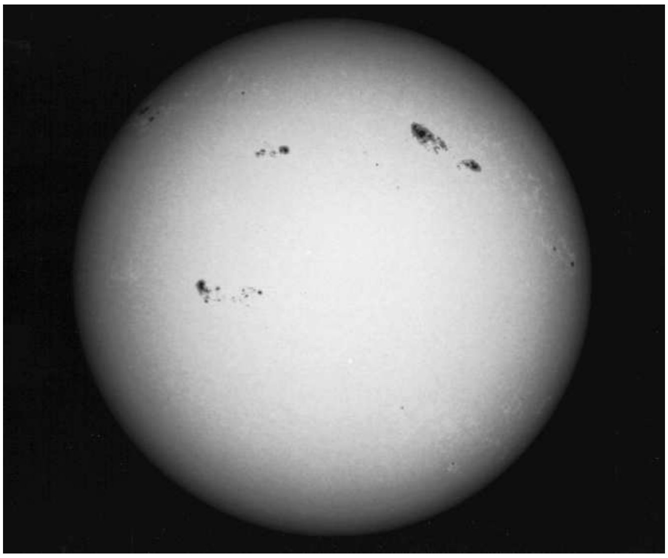

Figure 1.4: The Sun photosphere in white light. Near the edge the limb darkening is visible and scattered on the surface are clearly distinguishable sunspots and faculae.

of the observer line of sight up to unit optical depth corresponds to different photospheric depths depending on θ (Gray 2005). At the center of the disc ($\theta = 0$), the Sun appears brighter and hotter than the limb because the line of sight is perpendicular to the surface and we see deeper and hotter layers. At the edges ($\theta = 1$), the line of sight goes through shallower and cooler layers and the solar edges appear darker (Tayler 1997, Gray 2005).

The convective motion reveals itself in this layer through the *granulation*, which occurs owing to the turnover of cells of hot matter (thus brighter) that are moving upward and the cell of the cool one (thus darker) that are sinking downward. In adiabatic assumption (without heat exchange), a blob of material will tend to rise if its internal density remains smaller than the external one, $\rho_{\text{int}}(r) < \rho(r)$. The rising occurs so slowly that the internal pression, p_{int}, adjusts itself to balance the surrounding pressure, p. The instability condition is $\rho_{\text{int}}(r)$ - $\rho(r) < 0$. By using the perfect gas law[5] and the equivalence $p_{\text{int}}(r) = p(r)$, this condition becomes the *Schwarzschild criterion for convective instability*, i.e.

$$\left| \frac{dT}{dr} \right| > \left| \left(\frac{dT}{dr} \right)_{\text{ad}} \right| .$$

---

[5] The perfect gas law is

$$\rho = \frac{\mu P}{RT}, \tag{1.2}$$

where μ is the average molecular weight per particle and R is the gas constant. The quantity μ is a function of P and T and depends on the degree of ionization of the more abundant elements (hydrogen and helium).

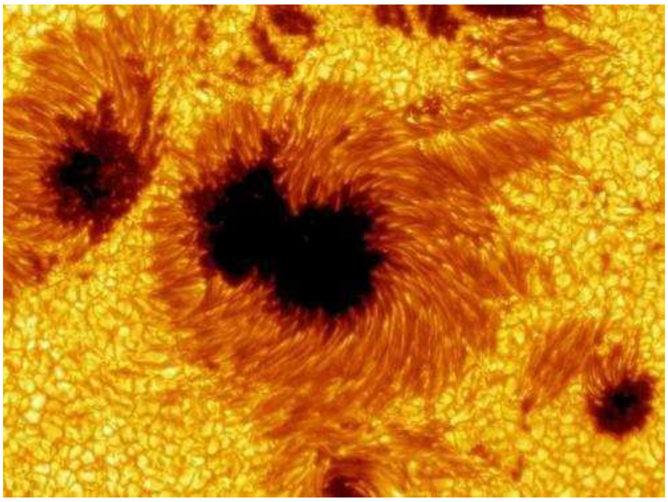

Figure 1.5: A zoomed view of sunspots. They are made up of the dark area, *umbra*, surrounded by the brighter *penumbra*. The picture is taken from http://www.astronomygcse.co.uk/AstroGCSE/New%20Site/Topic%201/sun/sunspots.htm.

When a rising blob becomes heavier than its surroundings, it begins to sink and returns to its initial position (Schrijver & Zwaan 2000). This complicated morphology gives, to the Sun surface, a constantly variable pattern with measured velocities of about 2 km/sec and a typical length-scale of about 700 km (Tayler 1997). There exists also a larger scale convection, known as *supergranulation*, with typical velocities and length-scales of 0.3 km/sec and $3.5{\cdot}10^4$ km, respectively (Tayler 1997). The other prominent properties are *spots* (see Fig. 1.2 and Fig. 1.4), and *faculae*, that are all patches of strong concentration of the solar magnetic field and deserve some attention.

Sunspots

Sunspots are the most evident sign of the solar activity with magnetic fluxes in the range $5{\cdot}10^{20} \lesssim \Phi \lesssim 3{\cdot}10^{22}$ Mx and the passage of a large spots group on the solar surface may induce a relative decrease in the optical flux of $\sim 3.3{\cdot}10^{-3}$ (Fröhlich & Lean 2004). A sunspot looks like a ragged patch in the solar surface which consists of a dark interior region, *umbra*, surrounded in general by a less dark one, *penumbra* (see Fig. 1.5). The temperature difference between the quiet solar photosphere (5778 K) and the umbra (typically about 4000 K, see Noyes 1982, Foukal 1990, Tayler 1997) is responsible of their darkness, since they radiate less energy than the actual photosphere. The penumbra has intermediate temperatures between umbra and the normal photosphere (Tayler 1997). Furthermore photospheric umbrae show a not uniform surface: there are brighter umbral dots in contrast with the umbral background, with sizes of the order of $1''$ or smaller, lasting typically from 30 min to 1 h, and an irregular pattern (Schrijver & Zwaan

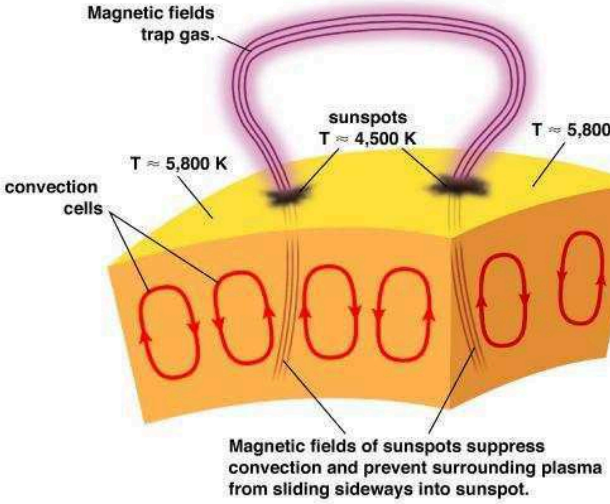

Figure 1.6: Solar magnetic loops sketch. Charged particles follow the magnetic field lines across the Sun. In regions of strong magnetic fields the convection is inhibited producing pairs of sunspots. The north and the south poles of the pairs are connected by the magnetic field loops far above the solar surface. The picture is taken from http://ircamera.as.arizona.edu/NatSci102/NatSci102/lectures/suninterior.htm.

2000). In many cases, bright features or extended filaments, observed as bright bridges, appear in the umbral areas and change from spot to spot.

The constant observation of sunspots has revealed that they are photospheric depressions if seen near the limb (effect known as *Wilson effect*). The unity optical depth at 5000 Å is at a lower geometrical level in the umbra (Wilson depression) because of the lower temperature that decreases the density at a given geometric depth.

In general sunspots occur in pairs, the two components having opposite polarity (*bipolar groups*, Stix 1989). These structures may be explained as the rising up of a magnetic field loop above the surface; this loop connects the components of a pair (see Fig. 1.6). Furthermore spots on opposite hemispheres of the Sun have opposite polarity (Stix 1989). During their lifetime the number and the position of sunspots above the Sun surface changes with time. The cyclic variation of the sunspot number has been object of intense studies pointing out the presence of a solar cycle connected to a variation in the general solar magnetic field. In the early phase of a solar cycle, sunspots are seen at a latitude of about 40°, then the region of spots occurrence migrates towards the equator (Stix 1989); the position of sunspots as a function of time is highlighted by the so-called *butterfly diagram*, as that in Fig. 1.7. Each solar cycle is characterized by the inversion of the magnetic field and thus of polarity of sunspots in the two hemispheres. Every 11 years the spot polarity is reversed and thus a complete solar cycle lasts

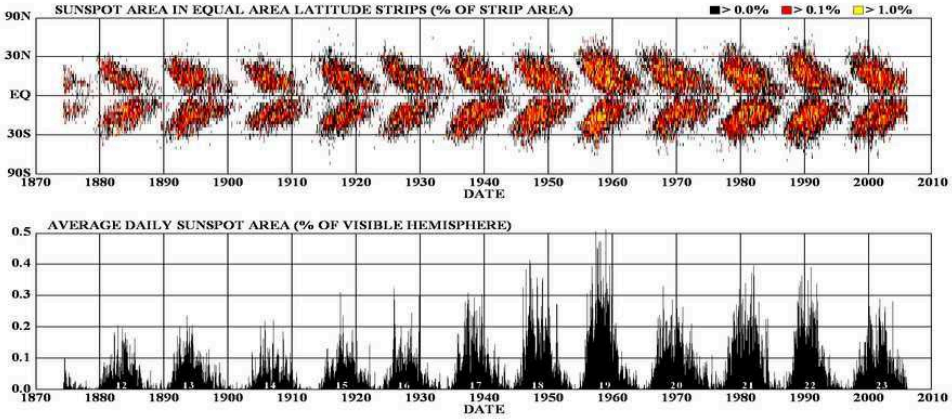

Figure 1.7: Daily sunspot area averaged over individual solar rotation. The picture is taken from http://www.nasa.gov/vision/universe/solarsystem/solar_cycle_graphics.html.

22 years.

The observation of sunspots has also revealed an important property of the Sun, i.e. the *differential rotation*. The Sun is not a rigid body thus its rotation is not the same at all latitudes. In fact the equator rotates with a velocity higher than that of poles thus the rotation period of the Sun at the equator is 27.7 days while it is 28.6 days at a latitude of 40°. This property may be responsible for the amplification of the solar magnetic field. For further details see Schrijver & Zwaan (2000).

Dark features smaller than sunspots are the solar *pores*, visible in white light, which can be considered as temporary stages in the sunspots evolution. They are as dark as the umbra but without penumbra with an average lifetime of about 1 day.

Solar faculae

Faculae are bright structures surrounding sunspots (see Fig. 1.8). They are extended concentrations of strong magnetic flux tubes with a field strength of about 1.5 kG that appear brighter than the quiet photosphere since they are hotter. They are long-lasting than spots and their average lifetime ranges from 10 to 80 days (Stix 2002). These magnetic structures are best observable in white light near the solar limb, in the core of strong spectral lines, such as Ca II H&K resonance lines, and in Hα on the whole solar disc and, in general, precede and follow the formation of new sunspots. They show a centre-to-limb variation since the contrast between solar faculae and the quiet photosphere is more enhanced near the limb than at the centre of the solar disc and their brightness depends on the size, the position on the stellar disc and wavelength. Thus while at the

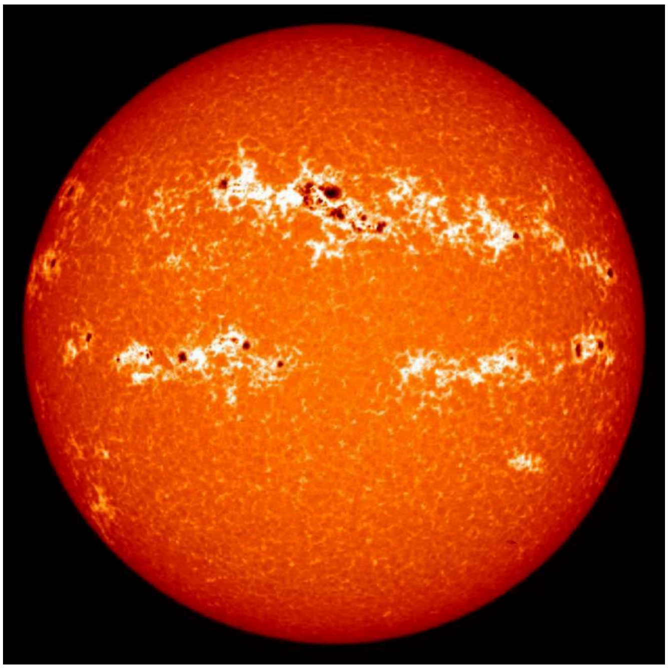

Figure 1.8: An image of the Sun taken from the LASP-built NSF Precision Solar Photometric Telescope (PSPT). White extended regions are faculae and red-black regions are sunspots. This picture is taken from http://lasp.colourado.edu/home/science/solar-influences/sun-and-climate/.

centre of the disc they are identified as points (Mehltretter 1974) with a size of about $\approx 0.2''$ (Muller & Keil 1983), at the limb they are localized in granules. In the case of the Sun, their presence increases the relative solar irradiance of $\sim 10^{-3}$ (Fröhlich & Lean 2004) even in period of solar maximum activity, that is when the number of sunspot is maximum. This means that facular brightness may offset, at a larger extent, the lack of energy radiated by the spotted photosphere (Foukal et al. 2006). For this reason the number of faculae are expected to depend on the solar activity. The excess of facular brightness depends on wavelength through the empirical relation

$$R(\lambda) = 0.53\ \lambda^{-1},$$

where $R(\lambda)$=(ΔI/I(λ))/(ΔI/I), found by Chapman & McGuire (1977) and it may be derived as the derivative of the Planck function in the limit of the Wien approximation:

$$\frac{\Delta I}{I} = \frac{\Delta B}{B} = \frac{hc}{k}\frac{\Delta T}{T^2}\lambda^{-1}.$$

This means that the facular contrast decreases with increasing wavelengths, thus its contribution is significant in the bluer bands whereas is lowered in the near-infrared ones.

The enhanced brightness of faculae is explained as due to the fact that they

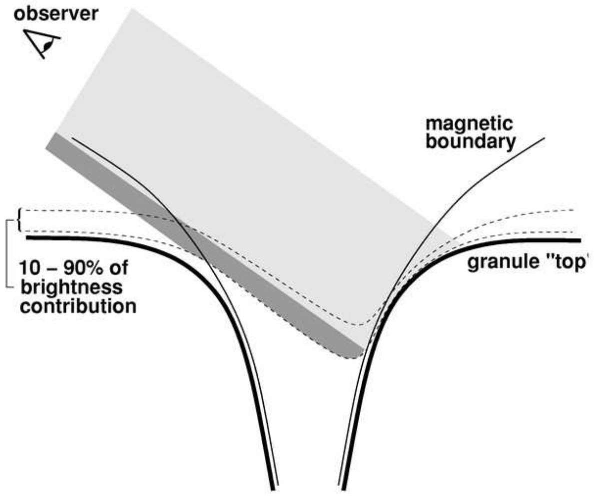

Figure 1.9: Sketch of a magnetic flux tube (region between thin solid lines) and adjacent granule (thick solid lines) illustrating the origin of facular brightening. The dominant part of the continuum radiation (80%) is formed in the region enclosed by the dashed lines. The brightness increase of faculae is mainly produced by a thin layer near the limbward interface between the magnetic flux concentration and the hot nonmagnetic granule. The dark path intensity is formed in the cooler regions of the centreward granule and inside the flux concentration. The dark shaded regions indicate the effective line of sight for the facular brightening and for the dark path (Spruit 1976, Keller et al. 2004, Nordlund et al. 2009).

are depressions among the photosphere granules and the low granular opacity allows us to see deeper in the solar surface. The intergranular lanes may be depressed up to 350 km below the mean height. Owing to the low density and opacity of granules, toward the limb and thus skewer lines of sight, we may observe the hot walls of granules from which the facular brightness enhancement originates. The increase in brightness is produced by a thin layer (∼30 km) of steep density gradient at the interface between the magnetic atmosphere and nonmagnetic granules. In general dark lanes appear near the centre of faculae. Moving limbward, from granule to facula, the line of sight intersects first a bright granule top, then cool matter above the granule and inside the magnetic flux concentration, and finally the hot wall of the granule on the further side of the magnetic flux concentration (see Fig. 1.9). Magnetic field strength changes may account for scratched pattern in the granule bright sides, owing to variations in the density and opacity. Weaker magnetic fields mean higher density and larger opacity, thus the radiation coming from regions with weak magnetic fields, i.e. higher and cooler regions, makes these locations appear darker (Nordlund et al. 2009).

In active regions faculae are arranged in enhanced network, that is a coherent distribution, while outside the active regions this bright network forms the quiet network. The observations of faculae and network reveal a complex structure called *filigree grains*, made up of round points and extended regions, with size of the order of about 300 km (Schrijver & Zwaan 2000), which seem to appear typically in the intergranular lanes (Stix 1989).

1.2.2. The outer layers

Outside the photosphere the solar atmosphere is composed by several layers: the *chromosphere*, the *transition region*, and the *corona* (Noyes 1982, Zirin 1988, Stix 1989, Golub & Pasachoff 1997, Schrijver & Zwaan 2000).

- The chromosphere is about 10 000 km thick (Tayler 1997). Within this region the temperature reaches a minimum (~4000 K) then begins to rise slowly till 10^4 K (see Fig. 1.3). The chromospheric spectrum shows a large number of strong emission lines, normally absorbed in the photosphere: Hα (656.3 nm), Ca II H&K (396.85 nm and 393.37 nm, respectively), and Mg II h&k (280.3 nm and 279.6 nm, respectively).

- The transition region is about few kilometers thick and is located between the relatively cool chromosphere ($\approx 10^4$ K) and the hot corona ($\approx 10^6$ K). It can be interpreted as a temperature regime rather than a physical and geometrical layer (Stix 1989). Its spectrum is observed in the UV and EUV wavelength regions and includes a plethora of emission lines due to the presence of ions at several temperatures: Si III (189.2 nm) formed at about $8 \cdot 10^4$ K, C IV (154.82 nm) and Si IV (139.37 nm) formed at about 10^5 K, O V and O VI (121.8 nm and 103.2 nm, respectively) formed at about $3 \cdot 10^5$ K.

- The corona is the outermost atmospheric layer with a temperature of the order of 10^6 K extending far from the visible surface of the Sun into space (few solar radii). Its emission is radiated in white-light (consisting of photospheric light scattered by electrons in corona and by interplanetary particles), in soft X-rays (continuum), in UV and optical spectral lines, and in radio waves. Some of the coronal emission lines come from the wavelength range between 331.8 nm and 1079.8 nm, e.g. from Ca XII to Ca XV, from Fe XI to Fe XV, from Ni XIII to Ni XVI.

1.2.3. Origin of solar magnetic activity

So far I have introduced the solar magnetic activity describing its manifestations over the Sun surface. In this section, I will briefly explain the origins of the magnetic structures, i.e. the *solar dynamo effect*. The dynamo process is a complex mechanism involving essentially three elements that allow it to work: the magnetic field, the differential rotation and the convective motion. All these elements have to cooperate in order to make the observed magnetic field self-consistent, explaining all the properties of the solar magnetic activity, e.g. the 11-year period of the sunspot cycle, and the equator-ward drift of the active latitudes seen in the butterfly diagram (see Fig. 1.7).

The solar dynamo mechanism may be described in five stages (as reference see the panels in Fig. 1.10). Starting with a phase of low activity (the first stage), the solar field is relatively weak ($\sim$1 G) and of dipolar shape. The field lines emerge from the surface at latitude of about $\pm 55°$, extending well out into the corona and returning back to the opposite polar cap. In the second stage the submerged field is drawn by the Sun differential rotation (i.e. the change in rotation rate as a function of latitude and radius within the Sun) becoming stronger. If R_{m}[6] $\gg 1$, the field lines remain frozen with the plasma rotation at different rates to be stretched out (see Fig. 1.10(a)). The initial meridional field lines gain an east-west direction, becoming essentially toroidal at lower latitudes and changing polarity at the equator, see Fig. 1.10(b). The intensification of the toroidal magnetic field takes some time to reach a given level and it is thought that the time needed to reach this threshold value increases toward the equator. When a critical value of intensification is achieved the magnetic field erupts to the photosphere forming active regions at a particular latitude at which the magnetic field increase stops. This would explain the occurrence of sunspots at high latitudes in the earlier stages of their evolution (see Sect. 1.2.1). The formation of active region is assumed to be due to two effects: the magnetic buoyancy[7] and the kinking of flux tubes by twisting them. This twisting may act on not uniform structures of the field due to convection causing a further intensification of flux

---

[6] The dimensionless quantity $R_{\mathrm{m}} = l_0 v_0/\eta$ is the *magnetic Reynolds number*, where v_0 is the typical plasma speed, l_0 is the typical length-scale of plasma motion, and η defines the magnetic diffusivity, i.e. a measure of the tendency of a magnetic field to diffuse. R_{m} gives a measure of the coupling between the plasma flow and the magnetic field. In the solar photosphere generally $R_{\mathrm{m}} \gg 1$ and the coupling is strong, whereas usually in laboratory experiments $R_{\mathrm{m}} \ll 1$ and the coupling is weak.

[7] For a flux tube, the horizontal equilibrium is expressed by the relation

$$P_{\mathrm{e}} - P_{\mathrm{i}} = \frac{B^2}{8\pi}$$

where P_{e} and P_{i} are the external and internal gas pressure, respectively, and B is the magnetic field intensity assumed to be uniform across the flux tube. Locally intensified field region is expected to have a lower gas pressure if it is in dynamical equilibrium with its surroundings. If the flux tube and its surroundings are at the same temperature ($T_{\mathrm{e}} = T_{\mathrm{i}}$), the internal gas density results to be lower than the external one ($\rho_{\mathrm{i}} < \rho_{\mathrm{e}}$) and a buoyant force is generated that leads the flux tube to rise till the solar photosphere.

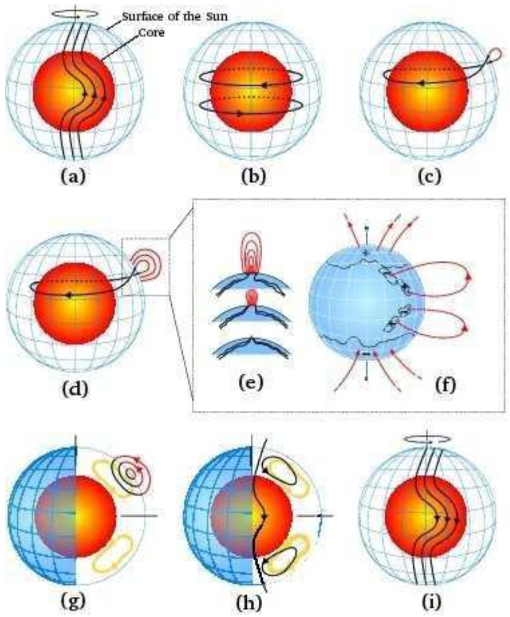

Figure 1.10: Sketch of solar dynamo process. Red inner sphere is the Sun radiative core and blue grid the solar surface. Between them is the solar convection envelope where the dynamo process resides. **(a)** Stretching of poloidal field caused by the Sun's differential rotation near the bottom of the convection envelope. **(b)** Toroidal field produced due to the stretching by differential rotation. **(c)** Intensification of toroidal field, rising of buoyant loops to the surface, twisting as they rise due to rotational influence. Two sunspots may arise from the footpoints of these loops. **(d, e, f)** Additional flux emerges (d, e) and spreads (f) in latitude and longitude from decaying spots (Babcock 1961). **(g)** Meridional flow (yellow circulation with arrows) carries surface magnetic flux poleward, causing polar fields to reverse. **(h)** Some of this flux is then transported downward to the bottom and towards the equator. These poloidal fields have sign opposite to those at the beginning of the sequence. **(i)** This reversed poloidal flux is then sheared again near the bottom by the differential rotation to produce the new toroidal field opposite in sign to that shown in (b). This picture is taken from http://www.hao.ucar.edu/research/lsv/lsvDynamoBackground.php

tubes and resulting in separate braided flux ropes with intensity at least an order of magnitude higher than that of the toroidal field (few hundred gauss). These flux ropes give rise to bipolar active regions as they reach the photosphere, see Fig. 1.10(c). In particular, each emerging flux ropes will generate a bipolar region with a preceding and following magnetic polarity (p- and f-portions, respectively), switching the polarity at the equator as the toroidal magnetic field does. The fourth stage explains the neutralization and reversal of the Sun poloidal field by observing that the f-portions of active regions tend to stay at higher latitudes whereas the p-portions at lower latitudes. As an active region evolves its f-portion moves towards the closest pole whereas the p-portion moves towards the equator.

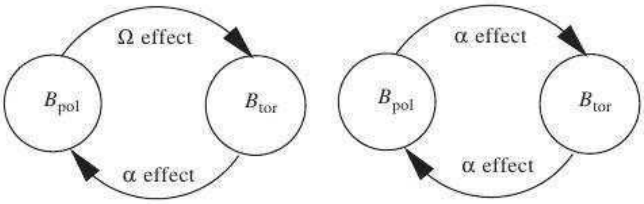

Figure 1.11: Regeneration of poloidal and toroidal fields in two dynamo. *Left*: $\alpha\Omega$ regime. *Right*: α^2 regime (Brandenburg & Subramanian 2005).

This process results in the neutralization of f-polarities with the existing polar field, while the p-polarities in the two hemispheres cancel out at the equator latitude, see Fig. 1.10(d, e, f). The poleward migration is ensured by the presence of a surface meridional flow which generates a surface reversed polar field, see Fig. 1.10(g). In the fifth stage, the newly formed poloidal field is already reversed and this occurs every 11 years before the onset of the next stage 1. A remnant component of these poloidal fields is transported down to the bottom of the convection envelope by the downward flow at high-latitudes and then towards the equator, with the opposite polarity compared to the beginning of the magnetic field sequence (Fig. 1.10(h)). This submerged field starts to experience the Sun differential rotation that stretches the field lines producing spots by the toroidal fields but with opposite polarity of the former analogous phase (Fig. 1.10(i)). The dynamo process proceeds in a similar manner to the preceding one but with the opposite polarity.

The solar dynamo effect is usually referred as to the $\alpha\Omega$ regime, meaning that the conversion between poloidal to toroidal field happens through the differential rotation, i.e. Ω-effect, then the opposite conversion occurs through the twisted convective turbulences, i.e. α-effect. In other stars there may exist other two dynamo regimes: the α^2 regime where an α-effect is responsible of the whole magnetic stellar cycle (see Fig. 1.11) and the α^2-Ω effect which is an intermediate regime between the first two.

For further details I refer to Foukal (1990), Rosner & Weiss (1992), Tobias (2002), Choudhuri (2007), Charbonneau (2010).

Photospheric models

Our observations and known physical laws are the bases on which the photospheric models are constructed. In this Section I will briefly describe the basic assumptions on which these models are constructed and how the resulting photospheric spectrum depends on the effective temperature, gravity, metallicity and direction. The atmospheric models of photospheres are at the base of the method which will be described in Sect. 2.1 and their primary assumptions are:

1. Plane parallel geometry, for which all the physical variables change as functions of one spatial coordinate (z) and this is valid since the photosphere thickness appears to be much less than the solar radius. This allows us to neglect, to a first approximation, inhomogeneous structures, such as granulation and sunspots.

2. Hydrostatic equilibrium[8], which means that the photosphere is subjected to two balancing forces, i.e. its own gravity and gas pressure.

3. Perfect gas law (see Eq. 1.2), which is assumed to be applicable in the photosphere.

The iterative procedure for the improvement of such models starts with an estimation of the vertical temperature profile, $T(z)$, which serves to compute the density distribution through the hydrostatic equation. Assuming a photospheric chemical composition, the opacity sources in this layer may be found as functions of ρ and T. In a configuration of thermodynamic equilibrium, i.e. assuming to be in *LTE*[9], the opacities are ruled by the degrees of gas ionization and excitation, calculated by using the Saha[10] and Boltzmann[11] equilibrium equations. Therefore at each depth the photosphere is described by a unique physical temperature

---

[8] The hydrostatic equilibrium equation is expressed as

$$dP(r) = -\rho(r)\ g(r)\ dr, \tag{1.3}$$

where $P(r)$ is the gas pressure, $\rho(r)$ is gas density, and $g(r)$ is the gravitational acceleration, all at a radial distance r from the Sun centre.

[9] LTE stands for Local Thermodynamic Equilibrium which is applied to small quantities of the model photosphere.

[10] The Saha equation gives the relative number of atoms in two ionization stages as a function of electron density, n_e, and temperature, T,

$$\frac{n_{j+1} n_e}{n_j} = \frac{u_{j+1} g_e}{u_j} \left(\frac{2\pi m_e k T}{h^2}\right)^{3/2} e^{(-\frac{I_j}{kT})},$$

where n_j and n_{j+1} are the number density of atoms in the ionization level j and $j+1$, respectively, u_j and u_{j+1} are the partition function of the two stages, g_e is the statistical weight of electron, m_e is the electron mass, I_j is the ionization potential from state j to $j+1$, and k is the Boltzmann constant.

[11] The Boltzmann equation describes the fraction of atoms excited to the n-th level, N_n, relative to the total number of atoms at the ground level, N, as a function of temperature, T,

$$\frac{N_n}{N} = \frac{g_n}{u(T)}\ exp\left(-\frac{\chi_n}{kT}\right),$$

where g_n is the statistical weight, $u(T) = \sum g_i\ exp(-\chi_i/kT)$ is the partition function, χ_n is the excitation potential required for the n-th level.

which determines the degree of ionization and excitation of the involved species. In order to obtain the emergent flux we have to solve the LTE radiative transfer equation which describes the variation of intensity with optical depth,

$$\mu \frac{dI_\nu}{d\tau_\nu} = I_\nu - S_\nu, \tag{1.4}$$

where $\mu \equiv \cos\theta$ being θ the angle between the normal to the solar surface and the line of sight, I_ν is the specific intensity at a frequenzy ν, τ_ν is the optical depth (see Eq. 1.1), $S_\nu = \epsilon_\nu/\kappa_\nu$ is called the *source function*, i.e. the ratio between emission ϵ_ν and the absorption coefficient κ_ν, both at a frequenzy ν. A formal solution of Eq. 1.4 may be obtained if we integrate from $\tau_\nu = 0$ (where we observe) to $\tau_{0\nu} = \infty$ (deep into the Sun), thus the total emergent flux at the direction μ is

$$I_\nu(0,\mu) = \frac{1}{\mu}\int_0^\infty S_\nu(\tau_\nu)\ exp(-\frac{\tau_\nu}{\mu})\ d\tau_\nu, \tag{1.5}$$

that is the specific intensity at the solar surface. To integrate this relation we have to know how the source function depends on optical depth in order to estimate the temperature profile as a funcion of optical depth (a direct determination of the temperature profile with τ_ν may be deduced by the photospheric limb darkening). In LTE conditions we assume that $S_\nu = B_\nu$, where B_ν is the black body radiation, thus the Eq. 1.5 may be inverted and the temperature profile as a function of optical depth, $T(\tau_\nu)$, may be derived at a specified wavelength (for further detail, see Stix 1989, Foukal 1990, Gray 2005).

1.3. Stellar activity

Among the main-sequence stars, the magnetic activity is expected to be found from the F-type to the M-type stars, i.e. from stars with thin convective envelopes to those with very deep convective regions (e.g., M5-type stars with mass smaller than 0.3 $M_\odot$, Schrijver & Zwaan 2000), see Fig. 1.12. The UV observations of main-sequence stars may help us to detect high temperature chromospheres and coronae, in several spectral type stars. In fact, spectral emission lines of C III ($\lambda\lambda$977, 1175) have been observed in FUSE spectra of A-type sources (Simon et al. 2002) whereas spectral emission lines of Ca II H&K are revealed in spectra of F0-type stars (Warner 1966, 1968). This allows us to actually extend the class of magnetic active stars now starting from A4-type stars down to the coolest M-type ones. As regards the stars evolved from the main-sequence, the indication of their magnetic activity is more complicated to be established at first sight. Such analyses were carried out by studying the Ca II H&K emission lines but significant outcomes were also obtained in other wavelength bands, i.e. in the UV and X-rays through the observation of IUE and Einstein observatories, respectively (Schrijver & Zwaan 2000). The chromospheric activity of ~500 evolved

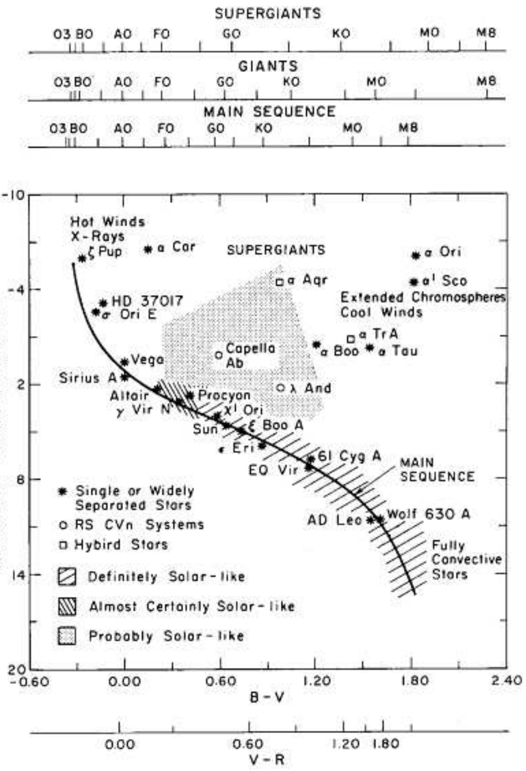

Figure 1.12: An H-R diagram with magnetically active stars, divided in group of solar similarity. Regions where massive winds and hot coronal plasma are seemingly absent are indicated. The indicated names are related to the most frequently sources (Schrijver & Zwaan 2000).

stars was carried out by Wilson (1976), by estimating the strength of the core emission of chromospheric Ca II H&K lines. These studies have been extended by Middelkoop (1982) and led to the observation of other 335 evolved stars. As an example, our Sun comes out to be a slowly rotating star with a moderate magnetic activity (Schrijver & Zwaan 2000) and we are principally interested to solar-like stars. This class of objects is a very broad set since it includes from late F- down to late G-type dwarfs, since the Sun has crossed several stellar evolutionary phases before the main-sequence stage. In principle, solar-like stars should also include subgiants concerning to the Sun in its pre main-sequence stage (Güdel 2007).

Throughout the H-R diagram we can distinguish several classes of stars that exhibit magnetic variability: *rotating variables* (BY Draconis, Algol, RS Canum Venaticorum, FK Comae), flare stars or UV Ceti type (dKe, dMe), *pre main-sequence stars*, PMS (T Tauri, AB Doradus).

The first class includes main-sequence, giant and subgiant stars with spectral types from B- to M-type, belonging both to single (*BY Dra type* and *FK Com* *type* stars) and close binary stars (*Algol type*, *RS CVn type*). Their brightness variability is caused by permanent or semi-permanent surface features (e.g. an uneven temperature distribution) on the surface, such as starspots (Vogt 1975), that are periodically observable due to the star rotation. The period of their variability may range from less than 1 to about one month with an amplitude up to 0.5 mag. For instance, the Sun may be considered a low-amplitude rotating variable (Percy 1978).

The second class includes stars of spectral type dKe and dMe[12] which exhibit a sudden rise of brightness lasting from few minutes to at most few hours and then return to quiescent level through a smoother trend. The brightness increase may reach about 5 magnitudes in U-band (Eason et al. 1992). The intense emission lines in their spectra suggest that are chromospherically very active (Melikian et al. 2011).

The third class includes pre-main-sequence very young objects, typically associated with dark and dusty molecular clouds (Schrijver & Zwaan 2000), with a mass of about $1M_\odot$. Their spectra show excess continuum emission, remarkable in the UV and IR, and a low excitation emission (Petrov 2003).

Historically, to have indications of the magnetic activity of a star as a function of time, an activity parameter was defined, the *S-index*, based on the spectroscopic emission lines of Ca II H&K and expressed as

$$S = \alpha \frac{H+K}{V+R}, \tag{1.6}$$

where H and K represent two photometric channels, with a passband of 1 Å centering on the Ca II H&K lines respectively, V and R are two other windows, with a passaband of 25 Å separated by 250 Å measuring the violet and red continuum on both side of the Ca II doublet, and α is a calibration factor. For long time the study of the temporal variations of this index was the primary method of revealing stellar magnetic activity and of indentifying solar-like cycles in other stars (Tayler 1997). In addition, the measuring of the S-index was also the primary goal of the *Mt. Wilson project*[13], aiming at the systematic study of stellar activity, that started in the middle of 1960s by observing about a hundred of main-sequence stars, then it was extended till the end of 2003 obtaining over 350 000 photometric observations of about 2500 stars. More recently the S-index has been converted into the quantity $R'_{\mathrm{H}K}$, which is a chromospheric activity index (Noyes et al. 1984, Baliunas et al. 1995, 1996, Henry et al. 1996, Wright

---

[12] The label *d* refers to dwarf stars, the label *e* refers to the presence of emission lines in the star spectra.

[13] See the website http://www.mtwilson.edu/hk/History/.

et al. 2004) and is expressed as (Noyes et al. 1984)

$$R^{'}_{\mathrm{HK}} = \frac{F^{'}_{\mathrm{HK}}}{\sigma T^{4}_{eff}},$$

where $F^{'}_{\mathrm{HK}} = F_{\mathrm{HK}}$ - F_{phot} is the chromospheric flux in the Ca II H&K lines (F_{HK} is the total flux in the Ca II H&K lines and F_{phot} is the photospheric stellar flux), and $\sigma T^{4}_{\mathrm{eff}}$ is the bolometric total stellar flux. The $R^{'}_{\mathrm{HK}}$-index is thus the fraction of the bolometric flux radiated by the star as chromospheric emission in the Ca II H&K lines.

The analysis of temporal variations of the activity index is crucial to derive some prominent stellar parameters, among which the stellar age and rotation. For example, it is securely established that, in solar-type stars, the magnetic activity decreases as stars age and that it is strictly connected with the loss of angular momentum and with the stars slowing down during the main-sequence phase. This means that young stars display relatively higher activity levels and faster rotations, whereas old stars, just like the Sun and even older, exhibit lower activity levels with slower rotations (Berdyugina 2005). Therefore it is possible to connect the stellar magnetic activity with the star rotation velocities through the *rotation-activity* relation and with the stellar ages through the *rotation-age* relation. For further details I refer to Wilson (1966), Noyes et al. (1984) for the first relation and to Skumanich (1972), Charbonneau et al. (1997) for the second one.

In addition, the magnetic activity of a star is not only identified with the variations in the chromospheric emission lines but also with the analyses of the stellar flux in other range of wavelengths, for example in X-ray (Pizzolato et al. 2003) and UV emissions (Ayres et al. 1995). Both emissions show also a correlation with the flux in Ca II H&K emission lines and this suggests a strong connection among the different layers of the outer stellar atmospheres.

1.4. Detection methods for extra-solar planets

According to the IAU definition an extra-solar planet is a celestial body orbiting a stellar object, or what remains of a star, with a mass ranging from that of Pluto (0.002 $M_{\oplus}$) to that needed for thermonuclear fusion of deuterium (13 $M_{J} \simeq 4100$ $M_{\oplus}$) (Mason 2008). Those objects with mass of the order of that of Pluto are classified as “dwarf planets”, whereas “brown dwarfs” are those objects with a mass involving at the most the thermonuclear fusion of deuterium. Finally, there exist “sub-brown dwarfs” which are free-floating bodies with masses lower than that required to the fusion of deuterium.

The first detection of an extra-solar planet occurred in the 1992, when two planets orbiting a pulsar star - the remnant of a massive star - were discovered

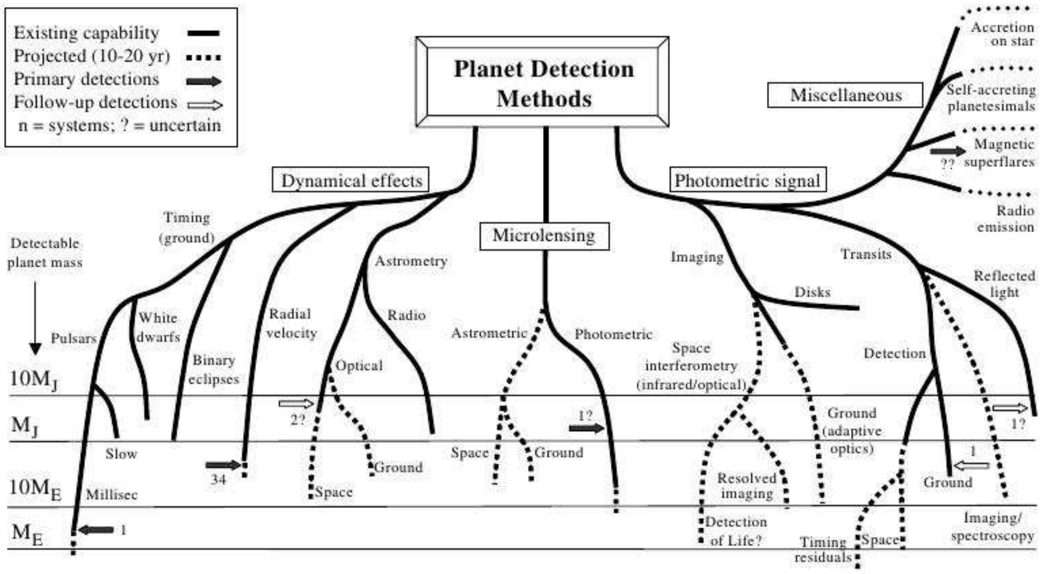

Figure 1.13: Detection methods for extra-solar planets. The lower horizontal lines refer to the current planetary detectable limit of masses reached by the corresponding method measurement (solid lines), and those which are expected in the next 10 − 20 years (dashed lines). Solid arrows indicate the actual detections according to the estimated masses, whereas open arrows indicate further measurements of previously-detected systems. “?” refers to unconfirmed detections (Perryman 2000).

(Wolszczan & Frail 1992). However this discovery did not gain much attention probably because this kind of stars are very different from the Sun. In the 1995, some years after that first claim, the discovery of the planet 51 Pegasi b (Mayor & Queloz 1995) orbiting around a solar main-sequence star (now classified as a G2.5IV star, Montes et al. 2001) occurred and this marked the starting point of the exoplanetary sciences. Our current knowledge has lead to the detection of 843 planets identified in 665 planetary systems and 126 multiple planet systems[14] and has pointed out the great variety of extra-solar planets if compared to planets in the Solar System.

Fig. 1.13 shows the totality of the extra-solar planets detection methods. They are divided in direct and indirect detection methods. The former methods are based on the direct observations of an exoplanet which may be difficult for several reasons. The last methods are basically devoted to reveal the presence of extra-solar planets looking for their influence on the parent stars. The most significant direct method is the the direct *imaging*. The most important indirect methods are the *radial velocitiy* technique, the *astrometry*, the *microlensing tech-*

---

[14] See the Extrasolar Planets Encyclopaedia, http://exoplanet.eu/, updated to November 7th, 2012.

nique, the *pulsar timing* technique, and the planetary *photometric transit* method which will be discussed in the following section. For further details for the other detection methods I refer to Irwin (2008), Doyle (2008), Ollivier et al. (2009), Perryman (2011).

1.4.1. Planetary photometric transits

A planetary transit occurs when an extra-solar planet passes in front of its parent star, temporary blocking a fraction of the starlight, if there are no additional perturbing bodies in the system, and crossing the line of sight between the star and the observer. As examples, the relative flux reduction due to the transit of Jupiter in front of the Sun is 0.01, the analogue quantity for the Earth is 10^{-4}. This is a periodic event in the course of the planet orbit and we call transit, or *primary eclipse*, the passage of the planet in front of the star, while an occultation, or *secondary eclipse*, occurs when the planet disappears behind the star. This technique is effective for close-in and small-period planets; for instance, the probability of detecting the transit of Jupiter or the Earth is 0.1% and 0.5% respectively, whereas for a more close-in planet, such as 51 Pegasi b, the probability increases to 10% (Eggenberger & Udry 2010) and in general we expect to detect Jupiter-like planets from ground surveys and Earth-like objects only from space. To date the transiting planets are more than 250 units and these detections are very significant since they allow us to characterize these planets in a unique way. From the other techniques we can put constraints on the planet masses (only lower limits from the radial velocity), the orbital shapes and sizes. With the transiting planets we can derive precise orbital parameters, the planet radius and gain more insight of their temperature structure and their atmospheres (Brown 2008). In Fig. 1.14 is shown the transit light curve of the planet WASP-10 b along with a sketch of this event. The stellar flux reduction (ΔF) produced by the primary eclipse is given by the ratio of the planet to star areas so that the relative flux reduction is expressed as

$$\frac{\Delta F}{F_0} = \left(\frac{R_{\mathrm{p}}}{R_\star}\right)^2, \tag{1.7}$$

where F_0 is the out-of-transit stellar flux, R_{p} is the planet radius, and $R_\star$ is the stellar radius. Thus we can infer a rather precise estimation of the planetary radius through the observation of a photometric transit of a planet if stellar radius is known. If there exist some astrophysical effects that perturb systematically the relative flux reduction of a planetary transit, $\Delta F/F$, by e.g. introducing temporal or wavelength dependences, in principle we may infer incorrect estimations of the planetary radius, even if the stellar radius is known. Moreover the identity in the Eq. 1.7 holds true when neglecting the limb-darkening effect that influences

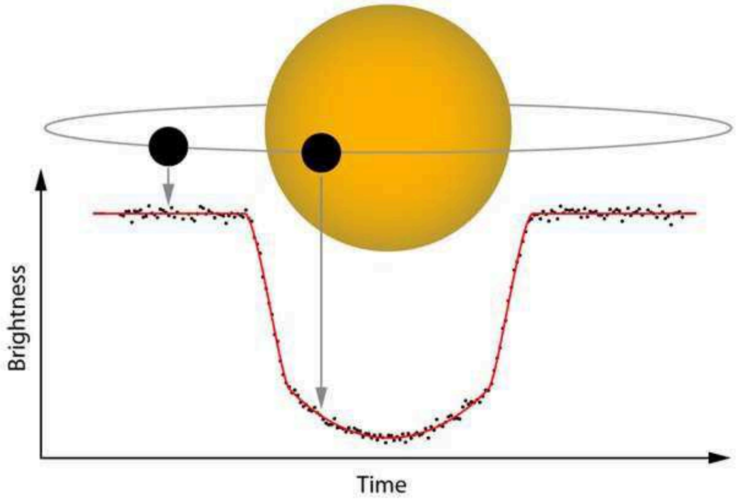

Figure 1.14: When the planet WASP-10 b passes in front of the star WASP-10, it induces a brightness decrease useful to measure the planet size.

the transit profile (see e.g., Seager & Mallén-Ornelas 2003, Czesla et al. 2009), as this effect introduces a colour dependence in the transit depth depending on the inclination respect to an edge-on orbit (Doyle 2008); this will be discussed in Sect. 1.4.2.

A significant parameter is also the maximum duration of the transit, t_{T}, which is the time required by the planet to cross the width of the stellar disc and, for a central transit (i.e. when the planet passes over its parent star along a line coincident to the stellar equator), may be suitably expressed by

$$t_{\mathrm{T}} = 13\,\frac{R_\star}{R_\odot}\,P_{\mathrm{orbit}}^{1/3}\left(\frac{M_\star}{M_\odot}\right)^{-1/3}, \tag{1.8}$$

where t_{T} is in hours, P_{orbit} is the orbital period in years and $M_\star$ is the stellar mass (Brown 2008). For a not central transit we expect that the duration is reduced by the factor $\sqrt{1-b^2/R_\star^2}$, where b is the impact parameter, namely the minimum distance between the planet and the star centres. For a solar-type star, a Jupiter-like planet may take 30 hours to complete a transit, an Earth-like planet 12 hours, and a close-in extra-solar giant planet (CEGP) about $2-4$ hours. A geometrical illustration of a planetary transit is given in Fig. 1.15. Moreover the planetary transit technique offers the opportunity of estimating the inclination angle of the planetary orbital plane, i, and deriving a more precise measure of the mass planet when combined with the radial velocity curve. Therefore the synergy among the different detection methods is a very precious tool that may help us to better characterize the great variety of the observed planetary systems, reducing the possible occurrence of false alarms (Brown 2003), such as grazing eclipsing binary stars (Brown 2008, Doyle 2008). For instance, the first transiting

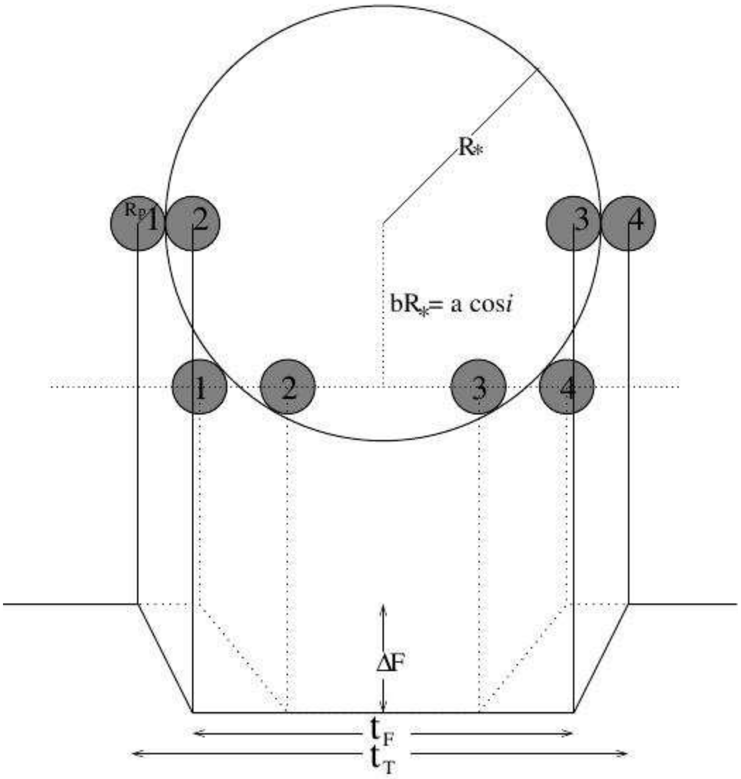

Figure 1.15: Illustration of the significant quantities in a transit light curve. In the *bottom* the solid and dotted lines refer to two different light curves whose geometry is described on the *top*. Some important properties are indicated: ΔF, $t_{\rm T}$, and $t_{\rm F}$, which is the elapsed time duration between the ingress and egress phases (i.e. the duration of the flat part of the transit). These phases start and finish in correspondence of the reported contact points between the planet and the star: from left to right they are indicated by the numbers 1, 2, 3, 4. Also reported are $R_\star$, $R_{\rm p}$, b and the orbital inclination angle, i. The two light curves on the *bottom* are obtained for two different b, and therefore i values (since $cos\ i = bR_\star/a$), Seager & Mallén-Ornelas (2003).

planet, HD 209458b (Charbonneau et al. 2000, Henry et al. 2000, Mazeh et al. 2000), was at first detected with the radial velocity and its transiting nature was revealed through a photometric follow-up. The opposite path was adopted for the OGLE candidates in the $2002-2003$. This survey selected photometrically a series of interesting planet candidates which then were analysed in spectroscopic programs (Udalski et al. 2002a,b,c, Udalski 2003).

Another significant parameter directly derived by fitting the transit light curve is $a/R_\star$, the normalized separation between the star and the planet, where a is the semi-major axis of the relative orbit. This parameter may be used to derive intrinsic information on the star providing important constraint for the characterization of a transiting planetary system. Following the line of reasoning of Sozzetti et al. (2007) and using the third Kepler's law, we can infer the stellar density $\rho_\star$ from the relation (Seager & Mallén-Ornelas 2003)

$$\frac{M_\star}{R_\star^3} \propto \left(\frac{a}{R_\star}\right)^3,$$

where the left-hand side is the stellar density and all the quantities are expressed in CGS units. Estimates of $\rho_\star$ provide constraints on the stellar evolution and luminosity (spectral type classes, Seager & Mallén-Ornelas 2003), sizes, and together with stellar effective temperature, it is used to derive the position of the star on the H-R diagram and hence its age from the isochrones.

Several large surveys are being carried out or planned to find transiting extra-solar planets and this large number of surveys will supply a great amount of light curves to be analysed. Light curve fits to transits events are largely used aiming to derive a precise characterization of the planet and its parent star and yelding significant constraint on planetary formation theory. This type of analyses requires fast computation of eclipse model (Mandel & Agol 2002). Assuming that the stellar and planetary bodies are well described with spheroidal shape, that the stellar limb darkening is well constrained (in most cases the quadratic law results to be convenient), the decrease in the stellar flux during a transit may be represented by the total or partial superimposition of the two discs (Pál 2008). The analytical description of transit light curves requires to be analysed by using fitting procedures. Most of the data modelling algorithms use the partial derivatives of the model function with respect to the model parameters (e.g., Levenberg-Marquardt fitting method, Press et al. 1992) in order to estimate the light curve variations directly from the change in the orbital elements. The use of partial derivatives has the advantage of speeding up the fitting procedure, just as described by Pál (2008). To estimate how the starspot-induced variations in the transit profiles may affect the derivation of orbital elements, I will introduce an application of the Pal's procedure in Sect. 2.1.4 and the relevant results will be reported in Sect. 3.2.2. The author presents the partial derivatives of the flux decrease function assuming a quadratic limb-darkening law. The relative apparent flux of an eclipsed star with a quadratic limb darkening may be written as $f = 1 - \Delta f$, where Δf is the flux decrease function (assuming that the out of transit flux is equal to 1). The author found an analytic form of Δf where the term depending on limb-darkening coefficients (LDCs) (γ_1 and γ_2) is separated by those depending on the geometry (R_p, $a/R_\star$, b, and E, i.e. the mid-transit time) and by using the Fisher matrix method (Finn 1992) they obtained the uncertainty and correlations between the fitted parameters. The correlation between the LDCs results to be dependent on the impact parameter b and so does the correlation of $a/R_\star$ with respect to b, if a standard parametrization of transiting light curve is chosen, namely $R_\mathrm{p}/R_\star$, $a/R_\star$, b, and E. Nevertheless with this parametrization the correlation between $a/R_\star$ and b results to be dependent on the planetary radius since it tends to unity if the planetary radius is decreased. Thus, in case of very small planets, the fitting methods could give distorted results. If the parametrization reported in Bakos et al. (2007) is adopted ($R_\mathrm{p}/R_\star$, b^2, $\zeta/R_\star$, E) no correlation between b^2 and $\zeta/R_\star$ is found, where

$$\frac{\zeta}{R_\star} = n\frac{a/R_\star}{\sqrt{1-b^2}}. \tag{1.9}$$

The proposed analytical analysis of light-curve parametrization reveals faster than to the analogous analysis carried out with Monte-Carlo methods and may be extremely useful in the implementation of the Levenberg-Marquardt algorithm.

Brightness contrast between star and planet

The detection of photometric transit signal due to extra-solar planets is strongly dependent on the brightness contrast between the planet and its host star, and the enviroment of the exoplanetary systems. Fig. 1.16 illustrates the wavelength dependent brightness contrast between some Solar System planets and the Sun. In the visible wavelengths, the Earth is about 10^{-9} times less bright than the Sun (at 0.5 μm in Fig. 1.16), whereas this contrast reduces to about 10^{-6} at infrared wavelengths (at about 10 μm in Fig. 1.16) allowing us to directly detect the radiation coming from the planet. Accordingly, to increase the contrast effect between the planet and its hosting star, observations in specific wavelength regions, such as infrared wavebands, are needed. Furthermore we have to take into account also the instrinsic planetary spectrum which is composed by two components (distinguishable in Fig. 1.16): one is due to the reflection of the starlight by the planet and the other is due to the intrinsic thermal emission of the planet itself. These emission components may be more intense in some wavelength regions rather than in others. For instance, in the case of an Earth-like planet orbiting a main-sequence solar-like star, the first component dominates the spectrum in the visible and near-infrared wavelengths (from 0.1 to 4 μm), the second component in the infrared region beyond 4 μm. We expect also that the brightness contrast depends on the nature of the stellar and planetary objects, namely on the star and planet effective temperatures, their main distance and the planetary atmospheric properties. In fact the distance between the planet and its parent star contributes to the radiative equilibrium of the planet. More distant exoplanets from their stars will have lower effective temperatures and viceversa.

Furthermore, as the Sun is surrounded by a debris or dust disk, we might expect that similar environments are also present around the other solar-like stars. This kind of disks permeate the equatorial plane where planetary orbits lie and emit a radiation of its own which may be revealed also in the infrared wavelength. This emission is far from being negligible because the spatially integrated emission

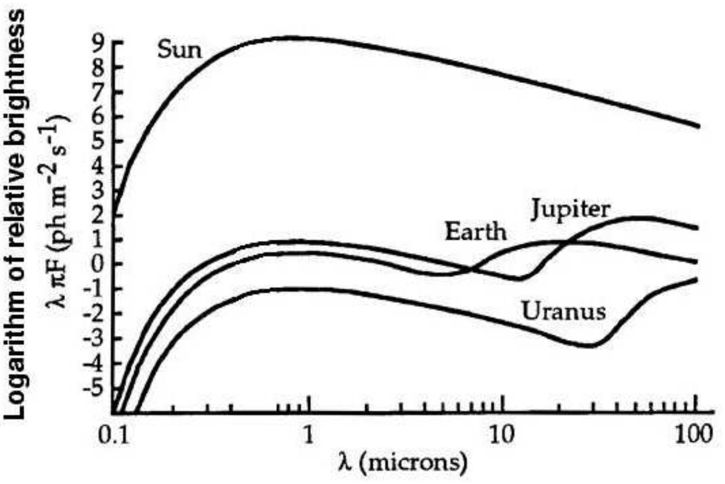

Figure 1.16: Comparison of the relative brigthness of the Sun, Earth, Jupiter and Uranus, in logarithmic units, vs. wavelengths.

over the whole disk may be about 300 times greater than that of the Earth in the case of our Solar System at a wavelength of 10 μm (Ollivier et al. 2009). In summary a photometric detection of an extra-solar planet may be favoured in the infrared wavelengths even considering these perturbative effects, if observations are carried out in specified infrared wavebands.

Transiting planets around M-dwarfs

The current research in the field of extra-solar planets is aiming at the detection of smaller and smaller planetary masses down to the Earth-mass limit, in order to identify the so-called *Super-Earth* planets with $\sim$1.5 Earth radii and $1 - 10$ Earth masses (Seager & Deming 2010). This kind of objects is expected to be favourable detected around stars that are smaller and colder than the Sun, namely M-dwarfs[15] (Butler et al. 2004, Nutzman & Charbonneau 2008, Deming et al. 2009). The reason why these stars should be surveyed are manifold:

1. M-dwarfs appear to be very common both in the Solar neighbourhood (Deming et al. 2009) and in the Milky Way ($\sim$75% of all stars). In fact a new catalog of bright M-dwarfs has recently been published by Lépine & Gaidos (2011) with 8889 M-dwarfs with J < 10. Given the M-dwarfs abundance in our Galaxy we might expect that these red stars harbour a huge number of planetary systems with more close-in and lower mass planets

---

[15] The M-dwarfs are main-sequence stars whose spectra show TiO bands and other molecular signature,s such as CaH, VO, FeH and CrH (Kirkpatrick et al. 1993), with masses ranging from about 0.5 $M_{\odot}$ to less than 0.1 $M_{\odot}$ (Tarter et al. 2007).

than those orbiting solar-like stars (Tinetti et al. 2011).

2. Planetary transits are deeper and thus easier detectable. This is ensured by the smaller stellar radii; an Earth-sized planet produces a 1.3 mmag transit depth if orbiting a M4V star, a 8.4 mmag if orbiting a M8V star and 0.084 mmag if orbiting a G2V star, i.e. the Sun (Deming et al. 2009).

3. The planet-to-star contrast is larger than that of the Earth-Sun system. In the Rayleigh-Jeans limit, this quantity depends on the relative surface area and the brightness temperature of the star and the planet (Tinetti et al. 2011). For a M4V star this contrast is 0.012%, for a M8V star it is about 0.11%, and for the Earth-Sun system the contrast is only 0.00044% (Deming et al. 2009).

   Among the extra-solar planets orbiting M-dwarfs, the scientific interest is also focused on those planets transiting in the habitable zone[16], around M-dwarfs. Owing to the lower luminosity of smaller stars, the habitable zones are closer to the stars if compared with solar-like stars (Nutzman & Charbonneau 2008, Tinetti et al. 2011) and the M-dwarf surveys may help us to investigate these planetary systems for the reasons below.

   - Planetary transits are more likely to occur since the habitable zone transit probability changes as $T_{\rm star}^{-2}$ (Nutzman & Charbonneau 2008, Deming et al. 2009). Since the transit probability depends also on the ratio $R_\star/a$, the probability for a planetary transit in the habitable zone of a low mass star is from about 2.3% to 5%, that is higher than the 0.5% probability for an Earth to transit a Sun-like star (Seager & Deming 2010).
   - Planetary transits are more frequent in the habitable zone. A planet at a distance of about 0.074 AU from a M5 star would transit once every 14.5 days while the Earth takes 1 year to orbit the Sun (Nutzman & Charbonneau 2008). This would be useful for detection by ensuring fewer hours of observation with sufficient orbital coverage (Deming et al. 2009).

All these points give support to the concrete opportunity to analyse photometrically this class of astrophysical objects in the search for habitable Earth-sized planets. In fact the observations of M-dwarfs hosting planets in the optical and near-infrared wavebands is the main scientific objective of a number of

---

[16] The habitable zone orbit is the orbital distance around a star where the planet temperature is such as to allow liquid water (Seager & Deming 2010), namely the planet receives the same insolation flux as that of the Earth from the Sun (Nutzman & Charbonneau 2008).

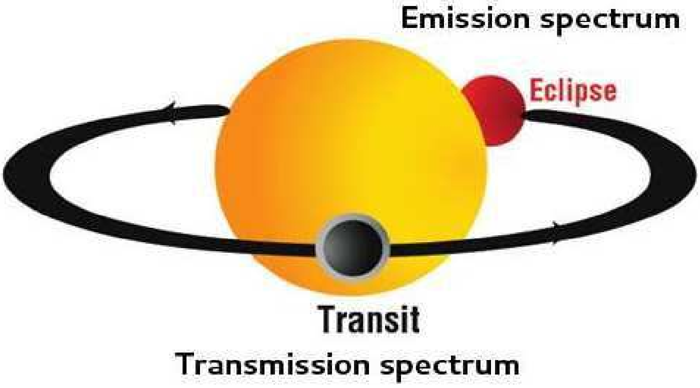

Figure 1.17: Transit and eclipse geometry for a transiting planet. The grey circular corona around the planet during the transit mimics the presence of an atmosphere.

ground-based projects, e.g., *MEarth* (see, Nutzman & Charbonneau 2008) and it is part of the program of the James Webb Space Telescope (*JWST*) project (Gardner et al. 2006).

Planetary atmospheres

Given the heterogeneity of the planetary atmospheres visible in our Solar System, to think at it as unique would be rather restrictive. We expect that, as in our Solar System, also in the other planetary systems there exist planets having an atmosphere and their characterization is the primary focus of some forthcoming space missions (Tinetti et al. 2011, Swain 2012a,b). In this sense the transit depth of a planet may provide significant evidences of the presence of a planetary atmosphere and also of its chemical composition. This characterization is made possible analysing the stellar spectra through two different configurations: *transmission* or *emission spectroscopy* (see Fig. 1.17). The first approach implies the study of the stellar spectrum during the transit (Seager & Sasselov 2000, Brown et al. 2001, Hubbard et al. 2001, Charbonneau et al. 2002): the starlight filters through the planet atmosphere carrying the signatures of molecules or atoms present in the planetary environment. The second approach analyses the reflected planetary spectrum during the secondary eclipse (Charbonneau et al. 1999, Cameron et al. 1999) that may provide information on the thermal emission of the planet and on the associated signatures (Perryman 2011). Both in these configurations a chemical composition, temperature and density of the atmosphere may be inferred (Tinetti et al. 2011). Even at intermediate phases, varying fractions of the planet disc are illuminated during the orbit and the corresponding modulation of brightness may help us to gain more knowledge about the longitudinal brightness distribution, its dynamics and

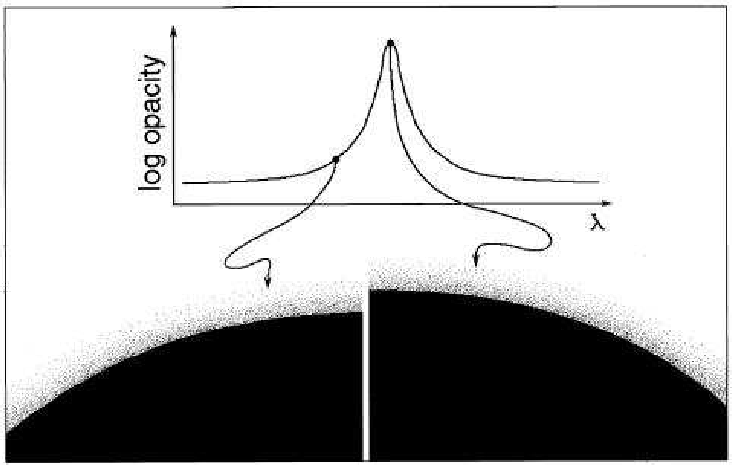

Figure 1.18: Dependence of the apparent radius of a planet on the wavelength selected for the observation. Wavelengths corresponding to large opacity provide larger radii, those corresponding to lower opacity provide smaller radii (Brown 2008).

thus how the absorbed stellar radiation is distributed between the day-side to the night-side of the planet (Tinetti et al. 2011). The spectroscopic follow-up of the exoplanets has revealed the wavelength dependence of the planet atmosphere observations since the atmospheric attenuation depends on the wavelength region in which the observations are performed, being more or less effective according to the wavelength region (see Fig. 1.18). The planet effective cross-sectional area will vary according to the opacity of the atmosphere and the apparent radius of the planet will be dependent on the altitude where the atmosphere becomes more rarefied (for a more detailed treatment see Appendix C). A most widely used approach to constraining the properties of planetary atmospheres is that of measuring the transit depth in different passbands observed simultaneously (e.g. from optical to infrared). The selective absorption of the stellar radiation by the molecular species, present in the planetary atmosphere, may produce a variation in the apparent radius of the planet versus the central wavelength of the passband and can be used to detect them (e.g., Désert et al. 2011a,b, Croll et al. 2011), thus the development of new methods to quantify the atmospheric opacity of an exoplanet is becoming crucial.

In addition the absorption features present in the spectroscopic follow-up studies of exoplanets enable us to identify specified elements in some atmospheres. For example, the atmosphere of the exoplanet HD 209458 b contains sodium (Charbonneau et al. 2002, Barman 2007, Burrows et al. 2007), hydrogen (Vidal-Madjar et al. 2003), and possibly carbon and oxygen (Vidal-Madjar et al. 2004). The sodium feature was observed by Charbonneau et al. (2002) with *HST*/STIS spectrograph in the wavelength range $581.3 \leq \lambda \leq 638.2$ nm producing a relative change in eclipse depth of about $(2.32 \pm 0.57) \times 10^{-4}$ and expected in theoretical atmospheric models of transmission spectra (Barman 2007) or reflection spectra in infrared wavebands (Burrows et al. 2007). Tentative searches were made to detect molecular signatures of CO, H_2O and CH_4 without a firm identification in infrared bands both in transmission and reflection spectroscopy (Brown et al. 2002, Richardson et al. 2003b,a, Deming et al. 2005). In the UV wavebands, *HST* observations of HD 209458 b have revealed atomic hydrogen features stronger than expected (the $Ly\alpha$[17] depth is about the 15%) for an atmosphere of a planet covering only the 1.5% of the star disc. The results of Vidal-Madjar et al. (2003) show that hydrogen atoms fill a large area around the star (beyond the Roche lobe[18] of the system) probably because of its escaping from the planet atmosphere. In the infrared wavebands the analysis of stellar spectra is very useful to establish the molecular content of the planetary atmosphere since it helps us to characterize the atmosphere during the occultation phase. Furthermore the infrared spectra have become a well-established field of transmission spectroscopy, since this domain includes the most important spectral signatures of the main atmospheric moleculae (Tinetti et al. 2007a, Swain et al. 2008, Pallé et al. 2011), such as CO_2, H_2O, CH_4 and NH_3 (Leger et al. 1996) even if still controversial (Ehrenreich et al. 2007, Désert et al. 2009, Sing et al. 2009, Gibson et al. 2011). To detect molecular signatures in planetary spectrum, both in transmission and reflection, in principle the observed spectrum is compared with atmospheric models including some interesting molecular species. Swain et al. (2008) compare their observed transmitted spectrum of HD 189733 b in infrared bands with simulated transmitted spectra that include contributions of interesting molecular species. With this approach they find signatures of the absorption of H_2O and CH_4. Thus, in principle, if the agreement between the observed points with their error bars and the theoretical spectra is good we can infer the related chemical composition, whereas if there are some departures some additional absorption features are required. Furthermore Swain et al. (2008) take into account the presence of cool spots on the visible hemisphere of the planet since the parent star is magnetically active. Thus the authors derive a correction factor assuming a starspots coverage of 4% in model spectra. This means that for active stars the presence of surface inhomogeneities introduces some not negligible bias. This issue will be detailed discussed in Sect. 1.4.2.

---

[17] The Lyman α line is an emission spectral line of hydrogen atom radiated when the electron drops from the $n = 2$ to $n = 1$ orbital, where n is the principal quantum number. In hydrogen atom it occurs at 121.6 nm.

[18] The Roche lobe is the region of space around a star in a binary system within which orbiting material is gravitationally bound to that star.

Current and planned space missions

Among the infrared facilities used for observations of transiting extra-solar planets, the InfraRed Array Camera (IRAC) has provided a large amount of photometric data, even if it was not launched for exoplanet research. It is one of the focal plane instruments on board on the *Spitzer Space Telescope* (SST). It is a four channel camera that gathers simultaneous broadband images at specified wavelengths, 3.6, 4.5, 5.8, 8.0 μm in two adjacent $5.2' \times 5.2'$ fields of view (FOV). The two shorter wavelength channels are built using indium and antimonium (InSb), whereas the two longer wavelength channels have detectors that have been specially treated with arsenic (Si:As). Each pair of detectors introduces incorrect systematic errors that may compromise the measurements obtained by infrared observations. The shorter wavelength channels[19] exhibit *pixel-phase effects* (Reach et al. 2005, Charbonneau et al. 2005, Morales-Calderón et al. 2006, Knutson et al. 2008) due to the telescope jitter and a significant intra-pixel variation in the sensitivity of the detector. The solution is thus to model and remove these effects (Désert et al. 2009) by decorrelating measured flux with the X or Y coordinate, or the radial distance from the pixel centre. There is not a universal correction method, each investigator chooses the decorrelation method that reduces the noise in their own data (Seager & Deming 2010). The pixel-phase effect may be present even in the longer wavelength channels but with a much less extent. In their turn the longer wavelength channels show non-linear trend with time, that is a gradual increase in intensity corresponding to an increase in the gain of the instrument response which is flux dependent (Deming 2009). This effect, called the *ramp effect* (Deming et al. 2006, Knutson et al. 2007a), is caused by the trapping of electrons by the detector impurities material (see Agol et al. 2010 for further details) reaching up to ∼10% for the least illuminated pixels over 33 hr (Agol et al. 2010), and increase over time (Machalek et al. 2008). What happens is as follows: the first photons are captured by ionized impurities and do not contribute to the signal, the additional radiation tends to saturate the charge trap and the signal readout reaches an asymptotic level (Deming 2009). In addition, the channel 5.8 μm can show an inverse ramp trend, i.e. the intensity decreases with time (Machalek et al. 2008). The ramp effect is not crucial for bright and high-contrast systems, since the time scale for the ramp to reach its maximum value is in general considerably longer than the typical eclipse duration. It may be more relevant for fainter and low-contrast systems since these

---

[19] Because of the cryogen depletion (about April 2009), only these two shorter wavelength channels are operating at full sensitivity (Deming 2009), since the observatory is being kept cooled at ∼35 K (*Warm Spitzer*, see the website http://ssc.spitzer.caltech.edu/warmmission-/propkit/som/).

uncertainties become significant if compared to eclipse depth (Deming 2009). The identification of all these instrumental systematics and artifacts is primarily due to the astronomers' necessity of separating planetary from stellar light in the time domain at small photometric levels (e.g., the IR contrast for a hot-Jupiter orbiting a Sun-like star is 10^{-4}, Seager & Deming 2010). In this context exoplanet investigations have proved to be very useful in defining the nature of the source of telescope systematic errors. Their correction is particularly relevant for future infrared missions, such as *JWST*, since the same Si:As technology, present in the last two *Spitzer*/IRAC channels, will be adopted for MIRI (Mid-Infrared Instrument, see Gardner et al. 2006). The *JWST* is a large (6.6 m), cold (< 50 K) infrared space observatory planned to be launched in the next decade which will cover the wavelength range from 0.6 to 28.5 μm. It will provide spectroscopic (NIRSpec, Near-InfraRed Spectrograph, and MIRI) and imaging data (NIRCam, Near-InfraRed Camera, and TFI, Tunable Filter Imager) with a telescope FOV of 166 arcmin^2.

The observation of stars hosting planets in the optical and near-infrared wavebands will be the focus of several space-borne telescopes, e.g. *EChO* (Exoplanet Characterization Observatory) and *FINESSE* (Fast Infrared Exoplanet Spectroscopy Explorer). The proposed ESA mission, *EChO* (Tessenyi 2010, Tinetti et al. 2011), is a space-borne telescope that will observe the visible-infrared spectra ($0.4 - 16$ μm) to characterize the physical properties of exoplanet atmospheres, searching for molecular spectral features and bio-markers. A significant part of the mission will be devoted to the observation of the atmospheres of super-Earth planets orbiting M-dwarf stars for the aforementioned reasons. The *FINESSE* telescope is a proposed NASA mission and space observatory which will gather near-infrared spectroscopic data ($0.7 - 5$ μm, Swain 2012b) of over 200 known exoplanets during a period of two years, with the goal of gaining understanding of what is the chemical composition of their atmospheres, and how our solar system fits into the larger family of planets (Swain 2012a,b).

1.4.2. Phenomena affecting photometric measurements

During a planetary orbit, some active regions may arise or pass on the observable star disc (starspots or faculae, completely analogous to the solar ones, see Sect. 1.2.1). These surface inhomogeneities produce brightness stellar variabilities (a.k.a. *rotational modulations*) that may interfere with the photometric detection of transiting planets. More active is the star, more noisy will be the detection. The actual effect is that they alter the transit depth (reducing or increasing it) by introducing errors in the determination of orbital, stellar and planetary parameters, among which the most significant is the planetary radius. This may have a significant impact on the derivation of the dependence of the planetary radius on wavelength (Pont et al. 2008, Czesla et al. 2009, Sing et al. 2009, Agol et al. 2010, Berta et al. 2011, Sing et al. 2011a,b, Désert et al. 2011a). The occurrence of such events is quasi-periodic since starspots or bright faculae rotate with the star rotational period, whereas extra- solar planets orbit with a timescale of their own. In the case of the Sun, dark spots have timescales ranging from weeks to months (Lanza et al. 2003, 2007), whereas a typical duration for planetary transits may range from a few hours to a few tens of hours. However comparable timescales are realistic and the distinction between the two situations may not be straightforward.

All the sources of microvariability in active stars can hamper the measure of planetary transits and this can be a problem for targets with a solar-type or slightly higher magnetic activity level, i.e. main-sequence stars from late F to dM stars. Therefore the search for planetary transits in presence of stellar activity requires techniques to filter out or fit the microvariability of the star. They are essentially based on the observations of the flux variations outside transits along time intervals of at least two or three stellar rotations (cf., e.g., Aigrain & Irwin 2004, Moutou et al. 2005, Bonomo & Lanza 2008, Bonomo et al. 2009).

Starspots

Starspots are peculiar regions with a high concentration of stellar magnetic field characterized by a lower effective temperature than the surrounding photosphere, thus they are darker than the rest of photosphere. Their passage onto the visible hemisphere of the star is similar to what we see on the Sun when a spot is visible on its surface where induces a variation in the total solar irradiance of about the 0.003% (Fröhlich & Lean 2004). On the Sun we can observe much details of such an event, the same is obviously not possible for much more distant stars, therefore we may figure them out through models and simulations (see bottom panel of Fig. 1.19).

The presence of starspots on the stellar surface affects the transit light curve in two ways. If during the transit the planet completely or partially occults the spot hiding temporarily a cooler fraction of photosphere to the observer, this is observable as a sort of brightness rise in the transit profile. Alternatively, if the planet does not occult the spot which remains on the star surface all the transit long, this produces a reduction of the stellar flux level in and out of the transit. In this last situation the absolute variation of flux ($\Delta F = F_{\rm it} - F_{\rm oot}$, where $F_{\rm it}$ is the in-transit stellar flux and $F_{\rm oot}$ is the out-of-transit stellar flux) does not change but the same does not happen if we want to quantify the relative variation of stellar flux ($\Delta F/F_{\rm oot}$). Such an event is very minute ($< 10^{-4}$ for an active star, like HD 189733, see Pont et al. 2008) but it has to be taken into account given the current detectors accuracy ($10^{-4} - 10^{-5}$ for *HST*/ACS observations).

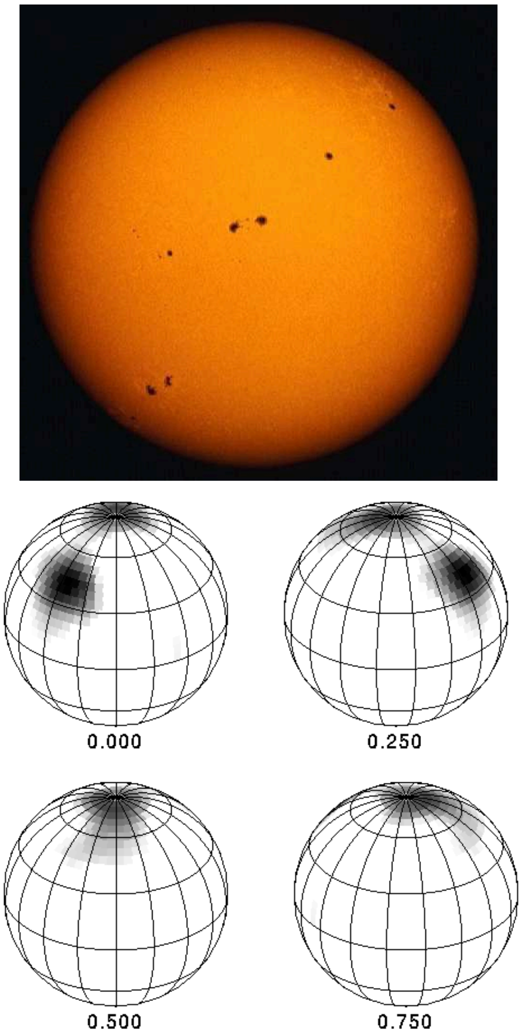

Figure 1.19: *Top*: group of sunspots. *Bottom*: starspot mapping on the surface of one component of a RS CVn binary as a function of the orbital phase as indicated below the simulations.

As an illustration, Fig. 1.20 shows simulations of the occulted and unocculted configurations where it is possible to observe how the presence of starspots contributes to the integrated stellar flux. Since these dark regions are cooler than the surrounding photosphere they induce a reduction in the stellar flux, regardless of the transiting planets, that depends on the temperature difference between the spot and the rest of the star but also on the relative size of the spot with respect to the stellar disc. The first factor introduces a chromatic effect that in principle depends on the difference of their spectra, i.e. two photospheres at different temperatures (see, e.g., Pont et al. 2008), thus the transit depth gains a colour dependence. The second one is a geometrical factor that may be dependent on the stellar magnetic activity level, usually referred to as *spot filling factor*,

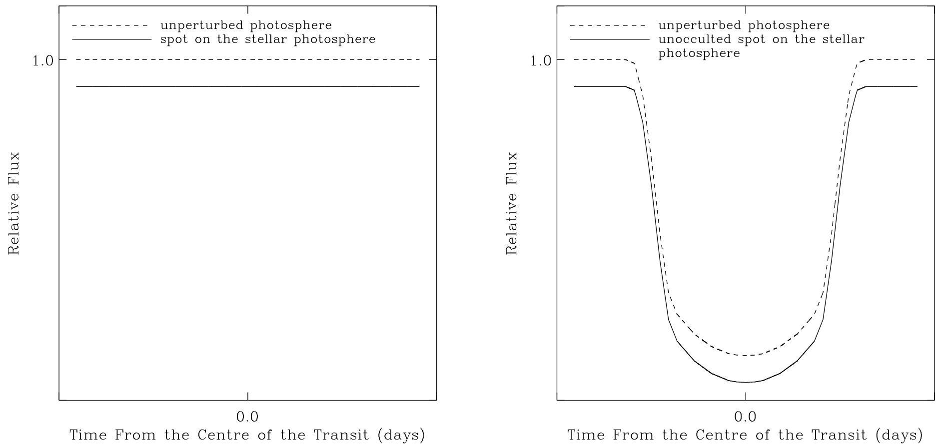

(a) With starspots but no planetary transit.

(b) With planetary transit and unocculted starspots.

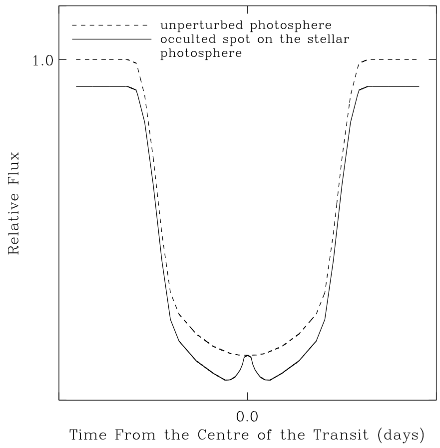

(c) With planetary transit and occulted starspots.

Figure 1.20: Simulated light curves. **(a)** In absence of a planetary transit. The dashed line refers to the stellar flux level in absence of starspots (unperturbed photosphere), the solid line refers to the stellar flux level in presence of one or more starspots. **(b)** In presence of a planetary transit and unocculted starspots. The dashed line refers to the unperturbed stellar flux during the transit, the solid line to the in-transit stellar flux in presence of unocculted starspots. **(c)** In presence of a planetary transit and occulted starspots. The dashed line is the same as before, the solid line refers to the stellar flux variations due to the transit of a planet which covers a starspot (or a group of starspots) located at the centre of the stellar disc where a flux bump is visible.

namely the fraction of the stellar disc covered by dark and cool spots. In addition, we have to take into account the wavelength dependence of the transmission planetary spectra, therefore disentangling all these effects becomes very crucial. The detection of anomalies in the transit light curve may be also used to estimate some stellar properties, e.g., the rotational period of the star (see, e.g., Silva-Valio 2008), and some orbital parameters, e.g., the spin-orbit misalignment[20] (see, e.g., Sanchis-Ojeda et al. 2011, Sanchis-Ojeda & Winn 2011).

Among the stellar parameters influenced by the activity there is the effective stellar temperature, $T_{\rm eff}$. As the Sun exhibits relative flux changes (still of about hundredths of percentage) in different wavelengths during its activity cycle (Krivova et al. 2006, Guillot & Havel 2011), these changes are expected in other solar-like active stars and are more critical for even more active stars. Thus $T_{\rm eff}$ estimates measured from spectroscopic analysis at different stellar activity phases may be sensibly affected by the presence of starspots or surface inhomogeneities in general and this introduces uncertainty in the derivation of the stellar $T_{\rm eff}$ (Guillot & Havel 2011). In this sense large error bars in the measure of $T_{\rm eff}$ may be considered as a useful tool to identify those uncertainties due to activity and starspots (Guillot & Havel 2011).

The starspots-induced variability effects are not limited only to the photometric measurements on the planetary transits but they influence also the radial velocity and astrometric determinations for extra-solar planets. For radial velocities further reading may be find in Saar & Donahue (1997), Queloz et al. (2001), Hatzes (2002), Bonfils et al. (2007), Dumusque et al. (2011), for astrometry further reading may be find in Lanza et al. (2008), Catanzarite et al. (2008), Makarov et al. (2010).

Stellar faculae

As in the case of the Sun (see Fig. 1.8), we expect that on the surface of other late-type stars, some bright regions appear. These inhomogeneities are analogous to the solar faculae and are extended regions which precede or follow starspots in longitude. Owing to the distances at stake we might only simulate their behaviour on the surface of the other stars by looking at that of the spots on the Sun where the amplitude of the solar flux variability induced by such events is about 10^{-3} at the maximum of the 11-yr cycle (Fröhlich & Lean 2004). Fig. 1.21 shows a simulation of the sunspots and faculae in order to understand their possible influence on the detection of Earth-like planet. As faculae are bright regions, their effective temperatures are higher than that of the rest of the photosphere (about

---

[20] This quantity refers to the angle between the sky projection of the angular momentum vector related to the stellar rotation and orbital motion. It may be revealed through the observation of a Doppler anomaly, the *Rossiter-McLaughlin effect* (RM), that occurs during the passage of a transiting planet in front of a starspot.

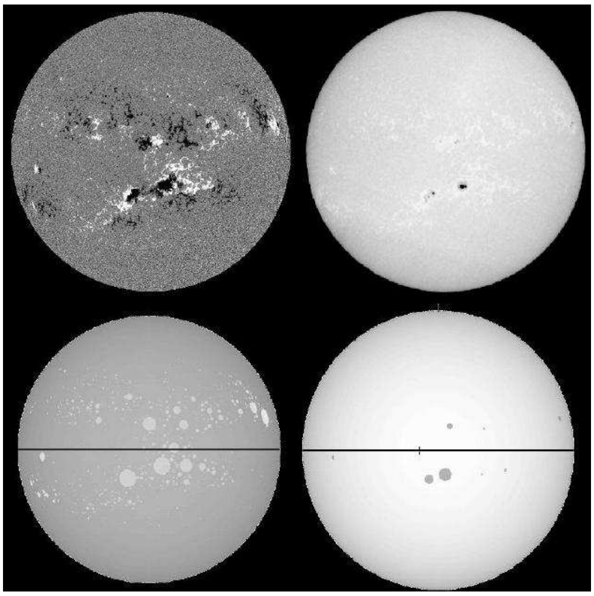

Figure 1.21: *Top panels*: MDI magnetogram of the Sun (*left*) and Meudon spectroheliogram (*right*). *Bottom panels*: simulated map showing faculae with a contrast of 10 with respect the photosphere (*left*) and spots from the USAF/NOAA data set.

100 K, see the simulations carried out by Lanza et al. 2006). Because of these temperature differences (named also *facular contrast*) their presence introduces a wavelength dependence discussed by Chapman & McGuire (1977) that show that the wavelength dependence of the facular contrast is proportional to λ^{-1}. Thus increasing wavelength means lowering the facular effect and if we want to reduce their contribution we have to use longer wavebands. In fact they are primarily visible in white light but their contrast decreases in the near-infrared bands (Solanki & Unruh 1998, Fröhlich & Lean 2004). In addition, this contrast depends also on their size and position on the star surface. The size dependence is so that, assuming the same facular contrast, the greater is the size of the bright region, the larger is its contribution to the stellar flux and in this respect it is useful to define the *facular filling factor*. In general we expect that this filling factor is larger than that of spots as can be observed on the Sun. As regards the position on the star surface (indicated by the quantity $\mu \equiv \cos\theta$, where θ is the angle between the normal to the stellar surface and the line of sight), faculae exhibit a centre-to-limb variation, namely they are more visible near the star disc edge (where $\mu = 0$) than at its centre (where $\mu = 1$), since the contrast is higher towards the limb and this behaviour is completely similar to that of the Sun. In presence of a transiting planet, we need to take into account of all these facular properties whose results are to alter the transit depth (in this case faculae tend to reduce this flux dimming) changing the overall level of the light curve (Czesla et al. 2009).

As in the case of the starspots, faculae may introduce some irregularities in other methods devoted to exoplanet detection, e.g., in the radial velocity and astrometric technique. For radial velocities estimation further related details may be found in Saar & Donahue (1997), Queloz et al. (2001), Hatzes (2002), Bonfils et al. (2007), Lockwood et al. (2007), Lagrange et al. (2010), Meunier et al. (2010), Dumusque et al. (2011); the influences of facular variability on astrometric measurements may be found in Eriksson & Lindegren (2007), Catanzarite et al. (2008), Lanza et al. (2008), Makarov et al. (2010).

Stellar limb-darkening

Limb-darkening effect is a wavelength-dependent decrease in the stellar specific intensity as a function of the position on the stellar disc. It may be expressed in terms of the quantity μ (i.e. the position on the star surface, $\mu \equiv \cos\theta$, see above) and may have several analytical laws. In the case of the Sun the limb-darkening formulation which gives quite good results is the linear law (Giménez 2006),

$$I(\lambda,\mu) = I(\lambda,1)[1 - u_\lambda(1-\mu)], \tag{1.10}$$

where $I(\lambda,\mu)$ is the specific intensity at a wavelength λ and position on the stellar disc μ, $I(\lambda,1)$ is the specific intensity at the centre of the stellar disc and u_λ is the linear LDC. This law gives quite good results if applied also to solar-like stars (Giménez 2006) but there exist more complicated formulations that may be applied in other cases and they are as follows:

- the quadratic law (Kopal 1950)

  $$I(\lambda,\mu) = I(\lambda,1)[1 - u_{1q\lambda}(1-\mu) - u_{2q\lambda}(1-\mu)^2], \tag{1.11}$$

  where $u_{1q\lambda}$ is the linear and $u_{2q\lambda}$ is the non-linear LDCs;

- the square root law (Diaz-Cordoves & Gimenez 1992)

  $$I(\lambda,\mu) = I(\lambda,1)[1 - u_{1s\lambda}(1-\mu) - u_{2s\lambda}(1-\sqrt{\mu})]; \tag{1.12}$$

- the logarithmic law (Klinglesmith & Sobieski 1970)

  $$I(\lambda,\mu) = I(\lambda,1)[1 - u_{1l\lambda}(1-\mu) - u_{2l\lambda}\mu ln\mu]; \tag{1.13}$$

- the cubic law (van't Veer 1960)

  $$I(\lambda,\mu) = I(\lambda,1)[1 - u_{1c\lambda}(1-\mu) - u_{2c\lambda}(1-\mu)^3]; \tag{1.14}$$

- a more general law (Claret 2000)

  $$I(\lambda,\mu) = I(\lambda,1)\left[1 - \sum_{k=1}^{4} a_k(1-\mu^{k/2})\right]. \tag{1.15}$$

These analytic formulations are very common in the analysis of the extra-solar planetary transit light curve and in principle the adopted method is to assume one of these “ad hoc” limb-darkening laws, with one or more coefficients, which will be optimized as part of the light curve fitting process (Howarth 2011). In turn the obtained coefficients may be used to test our knowledge in the stellar atmospheres thus furtherly improving it. However a precise description of the stellar atmosphere is crucial in the search for extra-solar planets through the photometric transit technique since this effect may introduce systematic transit profile variations leading to incorrect estimates of orbital parameters. Seager & Mallén-Ornelas (2003) outlined the limb-darkening effect on a planetary transit profile in the following three points:

1. variation in the depth of the transit light curve (ΔF) as a function of the impact parameter, b;
2. smoothing out the transit profile shortening the flat part of the light curve;
3. acting on the ingress/egress phase of the transit so as to blur the separation between these two phases and the central flat part of the transit.

This is effectively described in the Fig. 1.22, where the solid egress and ingress phases are only due to the changing in the star surface occulted by the planet as a function of time. Furthermore this figure clearly shows the wavelength dependence of limb-darkening effect and this behaviour clearly reflects on the shape of the transit profile. This is evident from the light curves of some transiting exoplanets: HD 209458 b, see Fig. 1.23 (Jha et al. 2000, Knutson et al. 2007b), HD 189733 b, see Fig. 1.24 (Pont et al. 2008) and CoRoT-2 b, see Fig. 1.25 (Czesla et al. 2009). All these behaviours may be explained as a colour dependence of the limb-darkened transit profiles. The longer the wavelength, the less will be the limb-darkening effect as predicted by atmospheric models (Claret 2004, Sing 2010, Claret & Bloemen 2011) and observed on the Sun (Pierce & Slaughter 1977). Thus near-infrared observations may help us to reduce this effect making it negligible (Richardson et al. 2006, Deming et al. 2007, Carter et al. 2008).

1.5. Goal and outline of the thesis

The aim of this thesis is to understand how stellar microvariabilities may affect the transit of an extra-solar planet in front of its star, in presence of starspots in particular.

In the light of what explained in the previous sections, the presence of starspots may alter the planetary transit depth producing a wavelength effect on the derivation of the planet radius (Sect. 1.4.2). An analogous colour dependence of the planetary radius is due to the presence of a planetary atmosphere

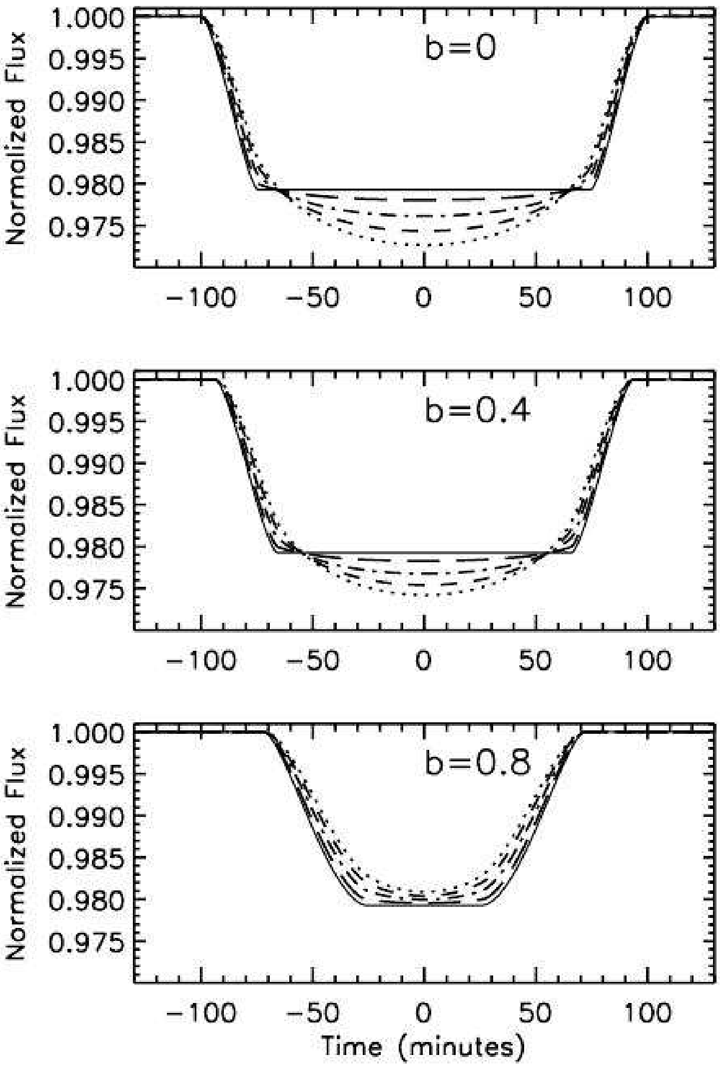

Figure 1.22: Solar limb-darkening dependence of a transit planet light curve. These theoretical profiles are derived for a system with $R_\mathrm{p} = 1.4\ R_\mathrm{J}$, $a = 0.05$ AU, $R_\star = 1\ R_\odot$, and $M_\star = 1\ M_\odot$. The solid curve is obtained neglecting the limb darkening. The other non-solid light curves are plotted with a solar limb darkening at the wavelengths of 3 (longer dashed), 0.8 (dot-dashed), 0.55 (dashed), 0.45 (dotted) μm. The three panels refer to different values of the impact parameter, reported on top of each graph (Seager & Mallén-Ornelas 2003).

(Sect. 1.4.1). To understand whether the apparent radius variations are due to molecular species in the planetary atmospheres or to stellar activity may be important. In this respect, the quantification of activity-induced variations, as functions of wavelength, may be crucial requirement for the transmission spectroscopy to help in the characterization of the planet atmosphere and composition.

- In Chap. 2 I will present the adopted method to model the starspot activ-

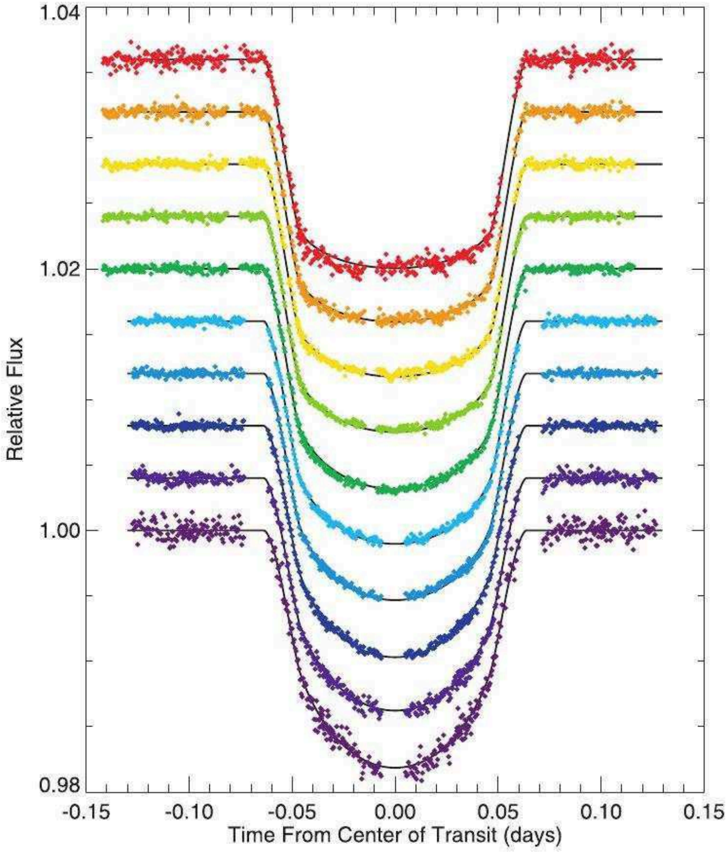

Figure 1.23: Normalized *HST*/STIS data of HD 209458b for 10 bandpasses from 293 (bottom) to 1019 (top) nm with theoretical transit curves (solid lines) and a four-parameters non-linear limb-darkening law overplotted. For clarity each light curve is shifted vertically of 0.004 (Knutson et al. 2007b).

ity. I will give an analytic formulation of the transit depth as a function of wavelength, of the position of starspots on the star surface and of the starspot filling factor. Moreover I will discuss the impact of starspots on the determination of orbital parameters. This analysis was carried out by using an IDL code, whose details are described in Appendix A.

- In Chap. 3 I will discuss the obtained results by analysing how the stellar activity influences the stellar colours and the characterization of a single light curve dip, how it contributes to the determination on planetary radius, and what are its effects on the determination of orbital and stellar parameters.
- In Chap. 4 I will present my conclusions.

The problem raised in the current work, i.e. the wavelength dependence of the starspots activity on the determination of planetary and stellar parameters,

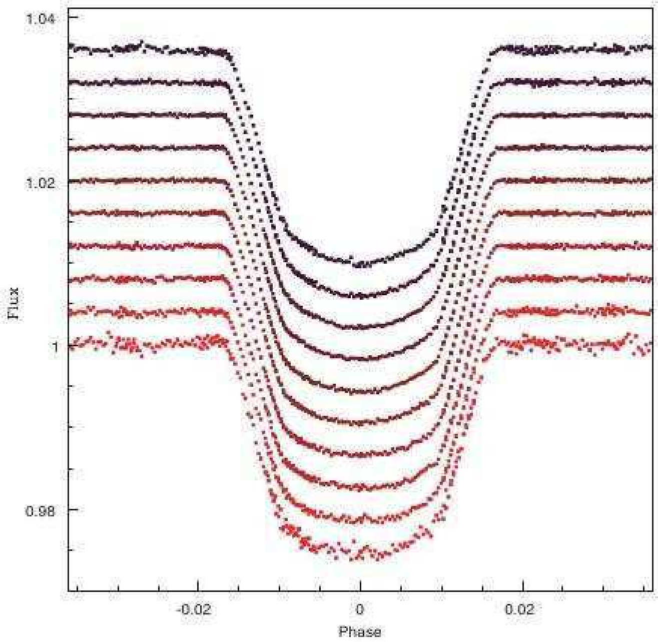

Figure 1.24: *HST*/ACS light curves for the transit of the planet HD 189733b in the 50-nm chromatic passband from 550 to 1050 nm, shifted vertically for visibility. The light curve are corrected for occulted and unocculted starspots. From the top to the bottom wavelengths increase (Pont et al. 2008).

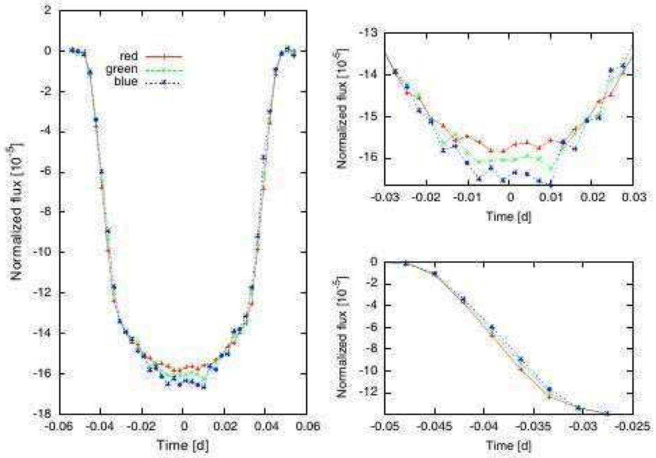

Figure 1.25: *Left panel*: Normalized *CoRoT* (COnvection, ROtation & planetary Transits) transit light curves for CoRoT-2b in three bandpasses: red, green and blue. *Top right*: an enlarged view of the transit centre. *Bottom panel*: an enlarged view of the ingress side of the transit (Czesla et al. 2009).

is an already analysed problem in the literature of extra-solar planets and in the following I will present three notable examples.

1.5.1. Three notable examples

The effects of activity are crucial above all for active stars, such as HD 189733 and CoRoT-2, but the issue rises even for less active stars, such as GJ 1214.

Since the discovery of its planetary companion (Bouchy et al. 2005), HD 189733 has been the subject of intense observations in both the optical bands (Bakos et al. 2006, Winn et al. 2007, Pont et al. 2007, 2008, Sing et al. 2011b) and the infrared wavebands (Beaulieu et al. 2008, Sing et al. 2009, Désert et al. 2011a). It is a K-type star with strong chromospheric activity (Wright et al. 2004). The underlying photospheric activity produces a quasi-periodic optical flux variation of $\sim$1.3% (Winn et al. 2007) due to the rotation of a spotted stellar surface. The first accurate determination of the planetary system parameters was carried out by Bakos et al. (2006) through BVRI photometry; neglecting the effects of stellar variability, their planet-to-star radius ratio (0.156 ± 0.004) was found to be smaller than that of Bouchy et al. 2005 (0.172 ± 0.003)[21]. Winn et al. (2007) obtained radius measurements compatible with those of Bakos et al. (2006), again neglecting the effects of stellar variability. Even Pont et al. (2007) obtained results compatible with those of Bakos et al. (2006), in this case taking into account the presence of stellar variability in their *HST*/ACS observations; these authors have detected the presence of occulted starspots that were cut away from the transit signal before fitting the observed light curve. Moreover, they expected that the starspots effect be reduced in the infrared because of a lower spot contrast. Through *HST*/NICMOS transit observations, correcting for the unocculted starspots, Sing et al. (2009) found a planet-to-star radius ratio of 0.15464 ± 0.00051 and 0.15496 ± 0.00028 at 1.66 and 1.87 μm, respectively, in agreement with the planet-to-star radius ratio of Bakos et al. (2006). Their corrections on the planet radius turn out fairly low since the relative planetary radius variation ($\Delta R_\mathrm{p}/R_\mathrm{p}$), calculated in these two wavelengths, results even an order of magnitude smaller than the uncertainty in the estimated planetary radius value (i.e. that of Bakos et al. 2006). In a multiwavelength set of *HST*/STIS optical transit light curves, Sing et al. (2011b) observed the typical signature of an occulted spot and, considering also the effects of unocculted spots, estimated a spot correction to the transmitted spectrum of about 0.00292 ± 0.00113 as a fraction of the transit depth in the $320 - 375$ nm passband, which is greater than in the $575 - 625$ nm passband where it is negligible. Moreover, they clearly demonstrated the dependence of the planet-to-star radius ratio on the out-of-

---

[21] Throughout this section, I present the results achieved in the literature by comparing the planet-to-star radius ratio of each source, so as to use quantities directly related to the observations, avoiding any inconsistency due to the use of different stellar radii. Where needed, I compute the $R_\mathrm{p}/R_\star$ ratio by using the stellar radius adopted in the relevant paper.

transit stellar flux showing that the transit is deeper when the star is fainter as expected as a consequence of unocculted spots present on the disc of the star during the transit (see Sect. 2.1.3). As a check, even in this case $\Delta R_{\rm p}/R_{\rm p}$ comes out to be small if compared with the uncertainty in the planetary radius value found by Bakos et al. (2006). In *Spitzer*/IRAC wavebands, both Beaulieu et al. (2008) and Désert et al. (2011a) detected variations in the planet-to-star radius ratio, then ascribed to the probable presence of starspots over the stellar surface during the observations. In fact none of these authors presented the planet-to-star radius ratio corrected by the starspots contribution. The former authors found that the infrared transit depth is smaller than in the optical (cf. Fig. 4 of Beaulieu et al. 2008) and that the effect of stellar spots is to increase this depth. By modelling this effect, they estimated that the transit depth is shallower by about 0.19%, at 3.6 μm, and 0.18%, at 5.8 μm. In the *Spitzer*/IRAC's 3.6 μm-band, the latter authors observed a greater $R_{\rm p}/R_{\star}$ ratio in low brightness periods because of the presence of starspots, implying that the apparent planet-to-star radius ratio varies with stellar brightness from $0.15566^{+0.00011}_{-0.00024}$ to 0.1545 ± 0.0003 (Désert et al. 2009) from low to high brightness periods, respectively.

A remarkable study of the starspot effects on the exoplanet sizes was carried out by Czesla et al. (2009) on the active star CoRoT-2 (Lanza et al. 2009, Huber et al. 2010). They pointed out the importance of the normalization of the transit profile to a common reference level to make different transits comparable with each other and show that the relative light loss during a transit is correlated significantly with the out-of-transit flux. The correlation is compatible with a distribution of starspots occulted during the transit that has a larger covering factor when the star is more active, i.e., when the out-of-transit flux is lower. A method for deriving the unperturbed transit profile is proposed by extrapolating the observed profiles towards their lower flux limit. A best fit to this profile gives a planet radius about 3% larger than that of Alonso et al. (2008), which is estimated without considering stellar activity in the CoRoT white bandpass ($350 - 1100$ nm).

An example of a less active M-type star that displays a rotational flux modulation of ~2% with a period of ~50 days is GJ 1214 (Charbonneau et al. 2009). Considering the error bars, the planet-to star radius ratio measurements through optical and near-infrared observations (Sada et al. 2010, Berta et al. 2011, Carter et al. 2011) are all consistent with the results of Charbonneau et al. 2009 (0.1162 ± 0.00067) obtained in the optical bands. Furthermore, Berta et al. (2011) detected variations in the planet-to-star radius ratio at different epochs and assessed the expected variation in this ratio due to stellar variability at optical wavelengths (see their Fig. 8). They stated that this effect may be neglected in *Spitzer*/IRAC bands. Croll et al. (2011) observed a deeper transit in the $\rm K_S$-band than in the J-band and, after taking into account the effects of the starspots, attributed this to a source of absorption in the $2.2 - 2.4$ μm range, possibly associated with methane (Miller-Ricci & Fortney 2010).

The above examples illustrate how stellar magnetic activity has a significant impact on the transit depth and in the consequent derivation of the planet radius and density, in both the optical and the infrared wavebands, thus leading in several cases to conflicting results. As shown, the study of stellar variability is limited to its detection during individual real observations, without any systematic theoretical treatment to characterize its impact through the analysis of stellar colours. This deficiency may lead to the development of “ad hoc” functional relations for each specific situation. For instance, Eq. (4) in Carter et al. (2011) represents the slight brightness increase due to the starspot occultation during a planetary transit and holds only when a circular spot, of the same planetary size, is considered. Thus a theoretical characterization of transit light curves may help the correct definition of planetary and stellar parameters.

Chapter 2

Starspots activity effects on stellar colours and exoplanetary transits

In this Chapter I will present a simple approach to estimate the spots contribution in the optical and infrared transit light curves, thus quantifying the flux variations induced by starspot magnetic activity as a function of the wavelength passband, and investigate the starspot effect on the colours of stars. Moreover, I will present a unified theoretical approach in order to better constrain the impact of both occulted and unocculted starspots on the determination of planetary, stellar, and orbital parameters. Therefore in the context of the transmission spectroscopy, I will examine the dependence of the apparent planetary radius on the magnetic activity level and wavelength.

2.1. Method description

My primary aim is to synthesize magnitudes and colour variations in solar-type stars when dark spots are on the visible hemisphere of the stellar surface, to understand the effect induced on the light curve of a planetary transit.

I use the standard BaSeL library of synthetic stellar spectra, worked out by Lejeune et al. (1997, 1998) and Westera et al. (2002), from which I take the stellar specific intensities to be integrated on the whole stellar disc. This library is based on the grids of model atmospheres spectra of Bessell et al. (1989, 1991), Fluks et al. (1994), and Kurucz (1995) and covers a wide range of parameters: effective temperature 2000 K $< T_{\rm eff} <$ 50000 K, gravity -1.02 $< \log g <$ +5.5, metallicity -5.0 $<$ [M/H] $<$ +1.0, and wavelength 9.1 nm $< \lambda <$ 160000 nm. Here I focus on the optical and infrared bands, in the Johnson-Cousins-Glass photometric system (UBVRIJHK bands) and in the *Spitzer*/IRAC wavebands centered at 3.6 μm, 4.5

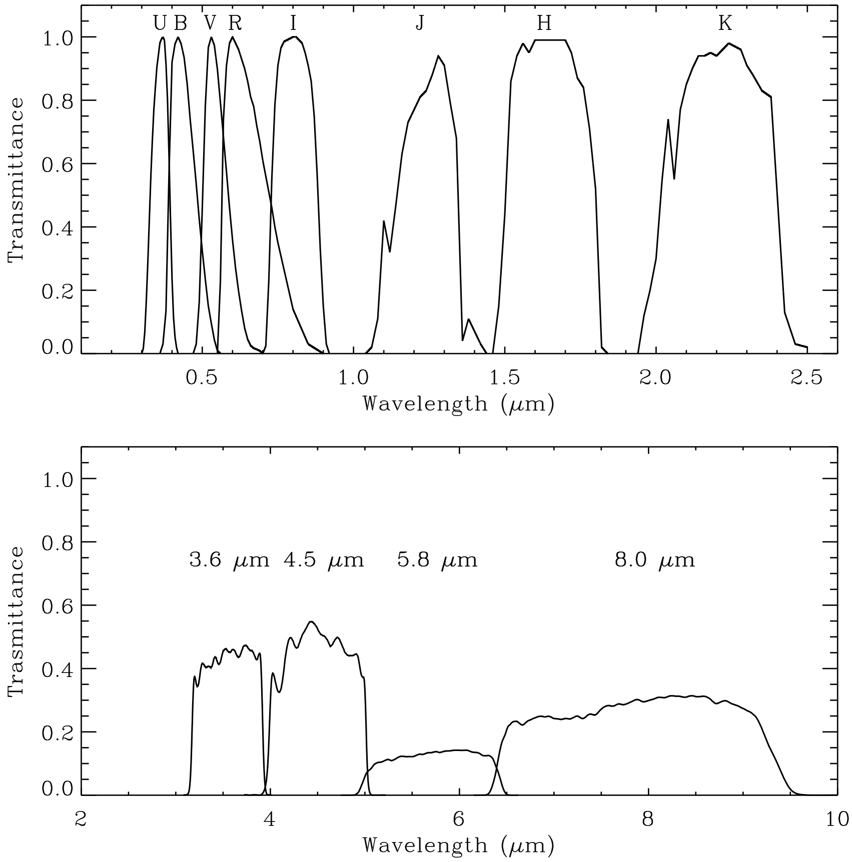

Figure 2.1: The transmittance of the filter set adopted in this work. *Top*: the Johnson-Cousins-Glass photometric system. *Bottom*: the *Spitzer*/IRAC passbands.

μm, 5.8 μm, and 8.0 μm, but the method may be generalized to any visible-NIR band. The stellar synthetic spectra have a wavelength resolution of 1 nm in the ultraviolet, 2 nm in the visible, $5-10$ nm in the near-infrared, and $20-40$ nm in the *Spitzer*/IRAC bands. To derive the stellar flux in the Johnson-Cousins-Glass photometric system and in the *Spitzer*/IRAC bands, I convolve the stellar flux distribution derived from the BaSeL libraries with the trasmission curves of the filters shown in Fig. 2.1. I choose as UBVRI filter passbands those adopted by Bessell (1990), as JHK filter passbands those adopted by Bessell & Brett (1988), and as *Spitzer*/IRAC filter passbands those reported at the *Spitzer Science Center* web site[1]. Both synthetic spectra and filter trasmission curves are interpolated in wavelength at the desired resolution.

---

[1] http://ssc.spitzer.caltech.edu/irac/calibrationfiles/spectralresponse/.

2.1.1. Modelling starspot activity

Considering a pattern of small spots uniformly distributed over the stellar disc, I assume a temperature difference between the star and the spot, $\Delta T = T_\star - T_\mathrm{s}$, where $T_\star$ and T_s represent the effective temperatures of the unperturbed photosphere of the star (i.e., with no stellar activity) and the spot, respectively. Following the same approach as Marino et al. (1999), the measured flux of the system "star + spots", $F_{\star+\mathrm{s}}$, corresponding to the specified temperature difference, is

$$F_{\star+\mathrm{s}}(\lambda) = (1-f)F_\star(\lambda) + fF_\mathrm{s}(\lambda), \tag{2.1}$$

where $F_\star$ and F_s are the unperturbed and the spotted photospheric fluxes, respectively, f is the spot filling factor (the fraction of the stellar disc covered by dark and cool spots), and λ the effective wavelength of one of the mentioned passband. The relative variation in the stellar flux produced by starspots with respect to the unperturbed photosphere is

$$\frac{\Delta F}{F} \equiv \frac{F_\star(\lambda) - F_{\star+\mathrm{s}}(\lambda)}{F_\star(\lambda)} = A_\lambda f, \tag{2.2}$$

where the contrast $A_\lambda \equiv 1 - F_\mathrm{s}(\lambda)/F_\star(\lambda)$ is a function of the passband. Similar approaches may be found in Désert et al. (2011a), Berta et al. (2011), and Carter et al. (2011).

In the computation of the stellar flux, I assume that the stellar and the spot intensities vary according to the same quadratic limb-darkening law, namely

$$I(\lambda,\mu) = I(\lambda,1)[1 - u_{1\lambda}(1-\mu) - u_{2\lambda}(1-\mu)^2], \tag{2.3}$$

which is totally analogous to Eq. (1.11), where $I(\lambda,\mu)$ and μ are already defined in Sect. 1.4.2, and $u_{1\lambda}$ and $u_{2\lambda}$ are the quadratic LDCs at the specified wavelength. Given the difference in the effective temperatures, the LDCs of the unperturbed and the spotted photospheres are actually different, but in the modelling of the stellar and solar light curves they are assumed to be the same in order to simplify the treatment (see, e.g., Lanza et al. 2003, 2004). For the current method, I have a maximum difference between the LDCs of ~30% in the U passband when considering main-sequence stars with an effective temperature in the range 3700−6000 K and spots with a temperature lowered by 1250 K. In view of the advantages of assuming the same limb-darkening profile and the other uncertainties present in the problem, I neglect such a difference (cf. Sect. 2.1.3).

The effect of the wavelength dependence of the limb darkening is shown in the case of CoRoT-2 by Czesla et al. (2009) using optical light curves at different wavelengths (see Fig. 1.25). The LDCs decrease from the U-band to the infrared giving a more flat-bottomed transit at longer wavelengths with shorter ingress and egress profiles (Seager & Mallén-Ornelas 2003, Richardson et al. 2006), see

Fig. 1.22, that can improve the determination of the transit parameters. Thus, even if I consider limb darkening in the derivation of the transit profiles, taking into account that it decreases towards longer wavelengths (see Table 1 in electronic form, Claret et al. 1995), its impact will not be so crucial, since this study is focused primarily on infrared passbands (see Deming et al. 2007, Carter et al. 2008, Berta et al. 2011), or rather, on understanding the difference in starspots effects between visible and infrared wavebands. Beyond this, the obtained contrast A_λ results to be independent from the limb-darkening wavelength dependence since, in its definition, the same limb-darkening law is present in both the numerator and denominator.

As already said in Sect. 1.4.2, the stellar microvariability may also be due to the presence of bright faculae. In the present study, I neglect their contribution since I am interested in the infrared bands where the facular effect may be considered less important. Moreover, the facular contribution to the optical flux variations seems to be negligible in the case of stars significantly more active than the Sun (cf., e.g., Lanza et al. 2009, and references therein).

2.1.2. Effects of starspots on stellar colours

I focus this analysis on star temperature values ranging from the solar one (∼5750 K) to that of an early M-type star and set the temperature difference between the star and the spot to 1250 K (see Berdyugina 2005). In order to examine the the colour dependences on activity I choose four stellar effective temperatures as references. These temperatures correspond to those of four real cases that will be analysed later on, in the Chap. 3. The properties of the reference systems, along with those of the related real ones, are summarized in Table 3.2. For the present application, I assume the presence of unocculted spots on stellar photospheres. The synthetic spectra, for both the unperturbed photosphere and the spots, were chosen for solar metallicity and gravity, i.e., $[M/H]_\odot = 0.0$ and $\log g_\odot = 4.44$.

The contrast coefficients A_λ, giving the spot-induced flux variations for each of the examined cases in the various wavebands (see Sect. 2.1.1), are reported in Table 2.1 and the spot filling factor of the out-of-transit spots, f_0, is assumed ranging from 0.01 to 0.5 of the stellar disc surface (Berdyugina 2005).

Fig. 2.2 presents the system flux vs. wavelength for all the cases, for a given filling factor of the out-of-transit spots. The solid curve represents the spectrum of the unperturbed photosphere and the dotted line the spectral distribution of the system “star + spots”. For all the systems, I plot a case with an extreme filling factor ($f_0 = 0.5$) to make the effect of the spots clearly evident. The spot perturbation decreases with increasing wavelength, although the details of the variation depends on the stellar effective temperature.

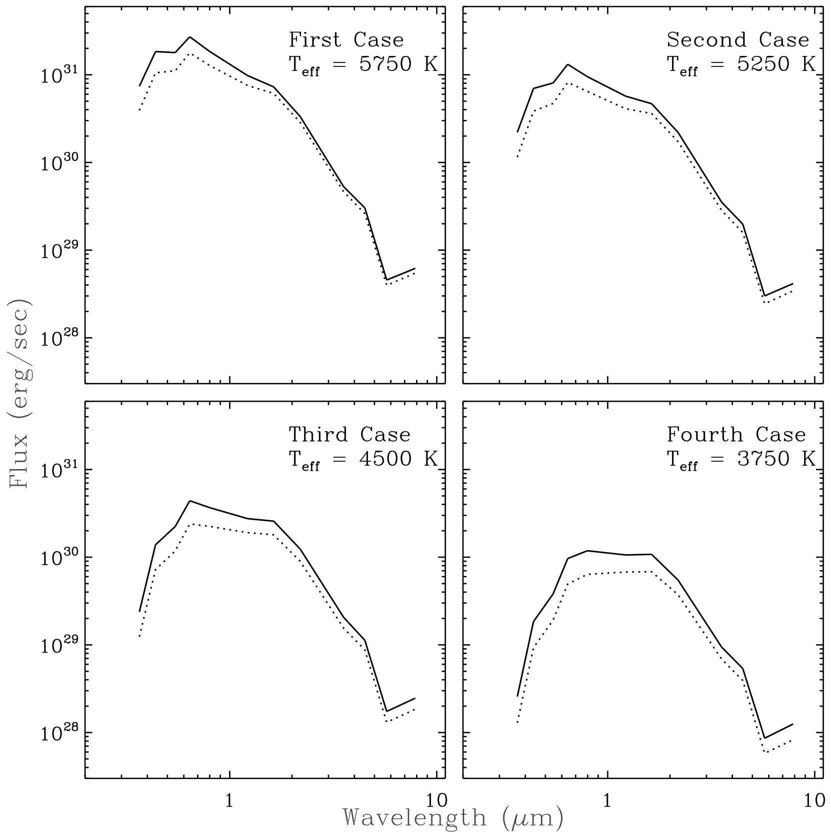

Figure 2.2: System Flux vs. Wavelength for all the reference cases present in Table 3.2. Solid lines plot the spectral distributions of the stellar unperturbed photospheres and dotted lines the spectral distributions of the star + spot systems with $f_0 = 0.5$. The *top left* panel presents the first case, the *top right* the second case, the *bottom left* the third case, and the *bottom right* the fourth case.

Fig. 2.3 reports the system fluxes, normalized to the unperturbed photosphere in each bands, vs. the filling factor values for the various bands. In this plot one can see how the flux of a similar system decreases as the filling factor increases since the spotted area and its corresponding contribution increase, and which wavelength passbands is less affected by spot effect in order to quantify its amount. The decreasing trend occurs in all the wavebands and for all the examined cases but in various extents. The less affected waveband depends on the particular parameter configuration and falls within the infrared passbands, the more affected one is always the blue passband (U-band). In particular for G and early-K stars, the minimum flux perturbation occurs in the 8.0 μm *Spitzer*/IRAC passband, while the maximum occurs in the U passband because the spot contrast increases monotonically towards shorter wavelengths. In the case of late-K and M stars, the minimum flux perturbation occurs in the 4.5 μm and 3.6 μm

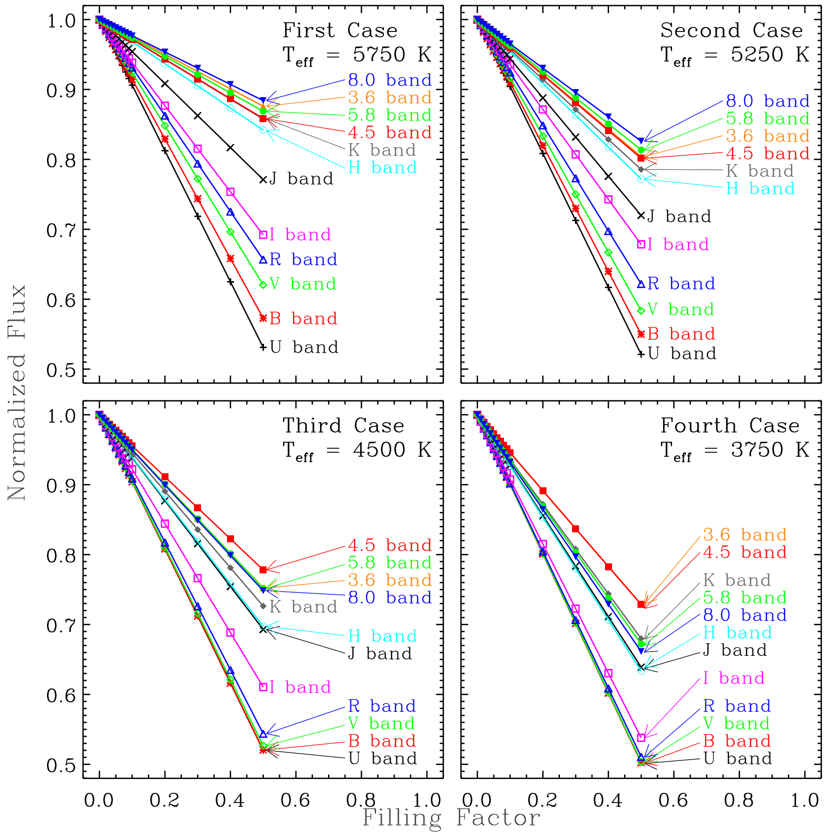

Figure 2.3: Flux Normalized with respect to the unperturbed stellar flux vs. Filling Factor in each passband, for the first case in *top left*, the second case in *top right*, the third case in *bottom left*, and the fourth case in *bottom right*. The different colors and symbols refer to the different passbands, as labelled.

Spitzer/IRAC passbands, respectively, due to molecular bands in the spectrum. These features are observed in the spectra of cooler stars, in both the optical and the infrared, and this results in a non-monotonous spectral variation in the correspondence of these bands. In this case, the unperturbed and spotted spectra do not behave as simply as power laws in the infrared domain as in the hotter cases.

Fig. 2.4 reports the variations in the normalized ratios $F_{\rm V}/F_{\rm band}$ vs. the filling factor f_0, where $F_{\rm band}$ is computed in three specified passbands (I, K, and 8.0 μm), with the purpose of understanding the extent to which the stellar magnetic activity may produce a variation in the colours of the star.

Both Figs. 2.3 and 2.4 suggest that the spots effect is more critical in the optical than in the infrared wavebands. Thus the effect of stellar activity on colours has to be taken into account if we want to analyse the photometric signals even of a moderately active star (comparable with or slightly more active than our

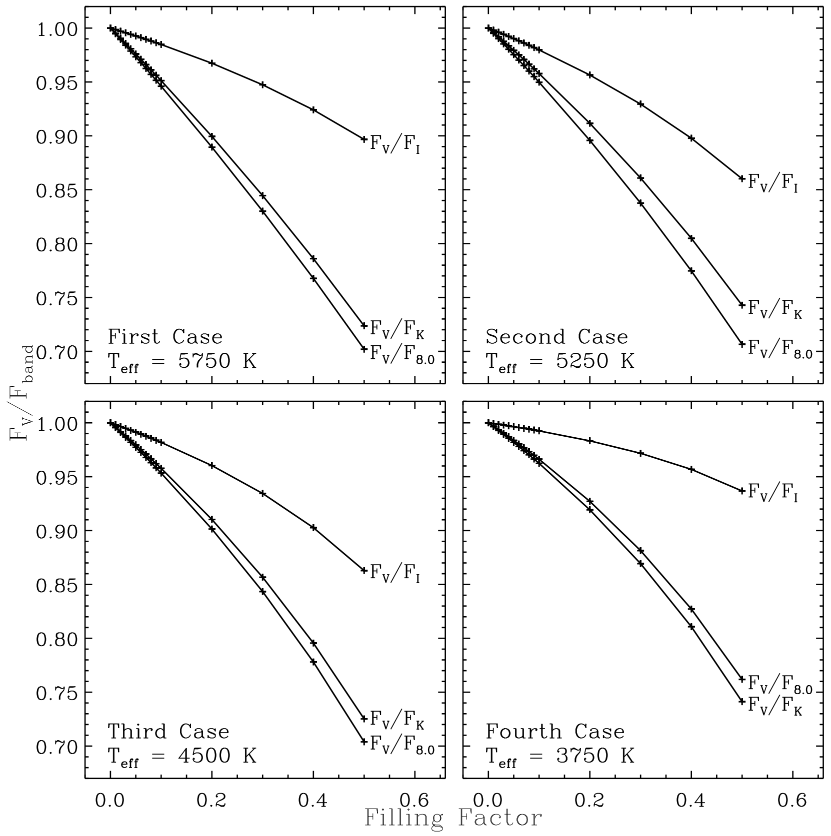

Figure 2.4: Normalized F_V/F_{band} vs. Filling Factor f_0 for all the reference cases present in Table 3.2 in the passbands I, K, and 8.0 μm. Different curves plot different ratios F_V/F_I, F_V/F_K, and $F_V/F_{8.0}$, as labelled. In the *top left*, the first case is reported, in the *top right* the second case, in the *bottom left* the third case, and in the *bottom right* the fourth case.

Sun). The effects are on both stellar colours (discussed in detail in Sect. 3.1), and the determination of the radius of the planet (discussed in detail in Sect. 3.2.1).

2.1.3. Effects of starspots on the apparent planetary radius

As said in Sect. 1.4.2, starspots affect in two ways the stellar flux variations in a transit light curve. Spots that are not occulted by the planet produce a decrease in the out-of-transit flux of the star F_{OOT}, which is the reference level to normalize the transit profile. Spots that are occulted during the transit produce a relative increase in the stellar flux because the flux blocked by the planetary disc is lower than in the case of the unperturbed photosphere. The occultation of a starspot is therefore associated with a bump in the transit profile whose duration, for a given planet disc size, depends on the spot size and whose height depends on the spot contrast (e.g., Pont et al. 2007, Sing et al. 2011b). Assuming the presence of unocculted spots on the visible stellar hemisphere and denoting the flux during the transit as F_{IT}, I have

$$F_{\mathrm{OOT}}(\lambda) = F_{\star}(\lambda) - \Delta F_{\mathrm{s}}(\lambda) \tag{2.4}$$

and

$$F_{\mathrm{IT}}(\lambda, \mu) = F_{\mathrm{OOT}}(\lambda) - \langle I(\lambda, \mu) \rangle \, \pi R_{\mathrm{p}}^2, \tag{2.5}$$

where $\Delta F_{\mathrm{s}} = A_{\lambda} f_0 F_{\star}$ is the flux decrease caused by the unocculted spots having a filling factor f_0 (cf. Eq. (2.2)), and $\langle I(\lambda, \mu) \rangle$ is the specific intensity averaged over the region of the stellar disc occulted by the planet of radius R_{p}. Considering the simultaneous presence of occulted spots and denoting the filling factor of the spots occulted during the transit when the planet's centre is at the disc position μ along the transit chord as f_{i}, then

$$\langle I(\lambda, \mu) \rangle = (1 - f_{\mathrm{i}}) \langle I_{\star}(\lambda, \mu) \rangle + f_{\mathrm{i}} \langle I_{\mathrm{s}}(\lambda, \mu) \rangle = \langle I_{\star}(\lambda, \mu) \rangle (1 - f_{\mathrm{i}} A_{\lambda}), \tag{2.6}$$

where $\langle I_{\star}(\lambda, \mu) \rangle$ is the average of the specific intensity of the unperturbed photosphere over the area occulted by the planet, and $\langle I_{\mathrm{s}}(\lambda, \mu) \rangle$ is the same quantity for the spotted photosphere. Eq. (2.6) is valid because I have assumed that the spotted and unspotted photospheres have the same LDCs. If I define the relative transit profile at wavelength λ as $D(\lambda, \mu) \equiv 1 - F_{\mathrm{IT}}(\lambda, \mu)/F_{\mathrm{OOT}}(\lambda)$, after some simple algebra I find that

$$D(\lambda, \mu) = \left(\frac{R_{\mathrm{p}}}{R_{\star}} \right)^2 G(\mu) \, \frac{1 - f_{\mathrm{i}} A_{\lambda}}{1 - f_0 A_{\lambda}}, \tag{2.7}$$

where $R_{\star}$ is the radius of the star, and $G(\mu)$ is a function of the limb-darkening coefficients and the disc position μ of the planet during the transit, but does not depend on the spot distribution and temperature. If I define the unperturbed transit profile as $D_0(\lambda, \mu) \equiv \left(\frac{R_{\mathrm{p}}}{R_{\star}} \right)^2 G(\mu)$, the profile in the presence of spots is

$$D(\lambda, \mu) = D_0(\lambda, \mu) \, \frac{1 - f_{\mathrm{i}} A_{\lambda}}{1 - f_0 A_{\lambda}}. \tag{2.8}$$

If the ratio $R_{\mathrm{p}}/R_{\star} \lesssim 0.1$, I can assume that $\langle I_{\star}(\lambda, \mu) \rangle \simeq I_{\star}(\lambda, \mu)$ (Mandel & Agol 2002) and the expression of the function $G(\mu)$ becomes particularly simple

$$G(\mu) = \frac{1 - u_{1\lambda}(1 - \mu) - u_{2\lambda}(1 - \mu)^2}{1 - \frac{u_{1\lambda}}{3} - \frac{u_{2\lambda}}{6}}. \tag{2.9}$$

In Eq. (2.7), the filling factor of the occulted spots f_{i} is in general a function of the position of the centre of the planetary disc along the transit chord, while the filling factor of the out-of-transit spots f_0 can be assumed to be constant because the visibility of those spots is modulated on timescales much longer than that of the transit, i.e., of the order of the stellar rotation period, which is generally several days. Moreover, when a geometric model is fitted to an observed transit profile, the bumps produced by occulted spots are excised from the data set to reduce their impact as much as possible. However, the capability of detecting the flux bump due to a particular spot depends on its size and contrast as well as on the accuracy and cadence of the photometry. If there is a more or less continuous background of spots along the transit chord, they cannot be individually resolved and the transit profile will appear to be symmetric and without any obvious indication of starspot perturbations. This is indeed the most dangerous case when fitting an observed transit profile. In this case, f_{i} can be assumed to be constant during a given transit because otherwise one would have detected the individual spot bumps. If I assume that both f_0 and f_{i} are much less than unity, I can develop the denominator of Eq. (2.7) into a series and neglecting the second order terms in the filling factors, I find

$$D(\lambda, \mu) \simeq \left(\frac{R_{\mathrm{p}}}{R_{\star}}\right)^2 G(\mu)\left[1 - A_{\lambda}(f_{\mathrm{i}} - f_0)\right]. \tag{2.10}$$

From Eq. (2.10), I see that the effects of the unocculted and occulted spots tend to compensate each other, although the filling factor of the occulted spots may generally be higher because starspots tend to appear at low or intermediate latitudes in Sun-like stars (see Sect. 1.2.1 and Fig. 1.7), being central transits (both θ and $b << 1$) more likely to be detected than the grazing ones ($\theta \sim 90$ and $b \approx 1$).

An alternative interpretation of Eqs. (2.8) and (2.10) is that spots change the apparent relative radius of the planet $(R_{\mathrm{p}}/R_{\star})_{\mathrm{app}}$ derived from the fitting of the transit profile (see Sect. 2.1.4) as

$$\left(\frac{R_{\mathrm{p}}}{R_{\star}}\right)_{\mathrm{app}} = \left(\frac{R_{\mathrm{p}}}{R_{\star}}\right)\sqrt{\frac{1 - f_{\mathrm{i}}A_{\lambda}}{1 - f_0 A_{\lambda}}} \simeq \left(\frac{R_{\mathrm{p}}}{R_{\star}}\right)\left[1 - \frac{1}{2}A_{\lambda}(f_{\mathrm{i}} - f_0)\right]. \tag{2.11}$$

Therefore, the apparent variation in the planetary radius is

$$\frac{\Delta R_{\mathrm{p}}(\lambda)}{R_{\mathrm{p}}} \simeq -\frac{1}{2}A_{\lambda}(f_{\mathrm{i}} - f_0). \tag{2.12}$$

When radius measurements are available in two different passbands λ_1 and λ_2, from Eq. (2.12) I have

$$\left(\frac{R_{\mathrm{p}}}{R_{\star}}\right)_{\mathrm{app}}(\lambda_1) - \left(\frac{R_{\mathrm{p}}}{R_{\star}}\right)_{\mathrm{app}}(\lambda_2) \simeq -\frac{1}{2}(A_{\lambda_1} - A_{\lambda_2})(f_{\mathrm{i}} - f_0). \tag{2.13}$$

If the spot temperature is known, this equation can be used to derive the effective filling factor $f \equiv f_\mathrm{i} - f_0$ from the apparent radius measurements in two well-separated passbands, e.g., in the U and the K passbands. If the spot temperature is not known, it can be derived when a third measurement is available in an additional passband, thereby removing the degeneracy between filling factors and contrast. However, the presence of a planetary atmosphere with a wavelength-dependent opacity can complicate the problem as we shall see in the final part of Sect. 3.2.1, in the case of HD 189733.

2.1.4. Effects of starspots on the determination of the orbital parameters

The perturbations in the transit profile due to starspots do not affect only the determination of the relative radius of the planet $R_\mathrm{p}/R_\star$ but also of the other geometrical parameters of the system (e.g., the relative semi-major axis, $a/R_\star$, the orbital plane inclination, i) and the limb-darkening coefficients. Most of the previous studies have considered only the radius variation (cf., e.g., Berta et al. 2011, Carter et al. 2011), but the impact on the other parameters can be significant. Czesla et al. (2009) explored the variation in the planetary radius and orbital inclination while fixing the semi-major axis of the orbit a, the stellar radius $R_\star$, and the limb-darkening coefficients u_1 and u_2 to the values of Alonso et al. (2008). In this way, they found that the radius of the planet is increased of $\sim$3% with respect of the value found by Alonso et al. (2008), by fitting the lower envelope of the transit profiles derived with their method[2]. On the other hand, they found no significant correction in the inclination i of the orbital plane of the planet to the plane of the sky.

A limitation of the approach by Czesla et al. (2009) is that by fixing the ratio $a/R_\star$, the duration of the transit t_T fixes the inclination because $t_\mathrm{T} = \sqrt{1-b^2}\ P_\mathrm{orb}/(\pi a/R_\star)$, where $b = a/R_\star \cos i$ is the impact parameter and P_orb the orbital period (see Sect. 1.4.1). Since the effects of the spots on the duration of the transit are generally small, the inclination is not changed by fitting the reference unperturbed transit profile. Therefore, to perform a proper estimate of the systematic effects produced by occulted and unocculted spots, we cannot fix any of the system parameters in fitting the transit profile.

The unperturbed transit profile $D_0(\lambda, \mu)$ can be derived from the lower envelope of the observed transit profiles if I can guess the minimum spot filling

---

[2] Assuming the presence of dark structures within every transit light curve of CoRoT-2, that always raises up the flux level in the light curve, Czesla et al. (2009) defined a lower envelope of the transit light curves as the reference undisturbed profile, required by the fitting procedure to obtain estimates of planetary parameters.

factor of the unocculted spots $f_{0\ \mathrm{min}}$ and of the spots occulted during transits $f_{\mathrm{i\ min}}$ since in principle the contribution of both occulted and unocculted spots cannot be excluded a priori from the lower envelope profile[3]. Thus from the lower envelope of the observed transits $D_{\mathrm{low}}(\lambda, \mu)$, I get an estimate of the unperturbed profile as

$$D_0(\lambda, \mu) = D_{\mathrm{low}}(\lambda, \mu) \frac{1 - A_\lambda f_{0\ \mathrm{min}}}{1 - A_\lambda f_{\mathrm{i\ min}}}. \tag{2.14}$$

Since $f_{\mathrm{i\ min}}$ is a constant, the unperturbed profile does not contain any bumps due to the occultation of individual spots and is symmetric with respect to the mid-point of the transit. Estimates of $f_{0\ \mathrm{min}}$ and $f_{\mathrm{i\ min}}$ may be inferred by monitoring as long as possible solar-like stars, e.g. by using *CoRoT* or *Kepler* space telescopes which may guarantee long continuous observations of targets (Hatzes 2003), in order to infer starspots behaviours as a function of spectral types. If this were the case, in principle from a statistical point of view we could draw some useful estimates of $f_{0\ \mathrm{min}}$ and $f_{\mathrm{i\ min}}$. This type of surveys is not yet available but it could prove to be extremely useful.

In order to deduce how the variations of transit profile caused by starspots can affect the determination of the orbital and stellar parameters of a planetary system, the starspot-corrected unperturbed profile $D_0(\lambda, \mu)$ may be fitted by using an analytical model for the transit, e.g., that of Pál (2008), as already described in Sect. 1.4.1. This has the advantage of providing analytic expressions for the derivatives of the transit profile D_0 with respect to the transit parameters allowing us an efficient application of the Levenberg-Marquardt method to minimize the χ^2 (Press et al. 1992). To minimize their mutual correlations, when running the best fitting procedure, I choose as free parameters $\zeta/R_\star \equiv (2\pi/P_{\mathrm{orb}})(a/R_\star)/\sqrt{1-b^2}$, b^2, $R_{\mathrm{p}}/R_\star$, and the limb-darkening parameters $u_+ \equiv u_1 + u_2$ and $u_- \equiv u_1 - u_2$ (see Pál 2008, Alonso et al. 2008, for a justification of the independence of this parameter set). The orbital period and the mid-transit epoch are kept fixed in the fitting because they can be derived from the observation of a sufficiently long sequence of transits. Specifically, the profile distortions due to resolved occulted spots may affect the timing of individual transits, but the spot perturbations can be assumed to be random so that they increase the statistical error in the timing. Therefore, a sufficiently long time series can be used to derive an accurate value of P_{orb}. I present an application of this method to estimate the impact of starspots on the fitting of the parameters ($a/R_\star$, i, and LDCs) of the system CoRoT-2 in Sect. 3.2.2.

---

[3] In periods of minimum activity our Sun does not exhibit any dark structures on its surface, thus $D_0(\lambda, \mu) \equiv D_{\mathrm{low}}(\lambda, \mu)$, but the same may not be true for different spectral type stars.

Table 2.1: Contrast coefficients A_λ for each reference system in the different passbands.

Case	A_U	A_B	A_V	A_R	A_I	A_J	A_H	A_K	$A_{3.6}$	$A_{4.5}$	$A_{5.8}$	$A_{8.0}$
1)	0.938	0.854	0.759	0.686	0.616	0.458	0.316	0.285	0.248	0.283	0.262	0.232
2)	0.958	0.901	0.833	0.756	0.643	0.560	0.456	0.429	0.392	0.397	0.373	0.348
3)	0.960	0.959	0.946	0.912	0.779	0.614	0.605	0.547	0.495	0.444	0.496	0.503
4)	0.994	0.995	0.992	0.978	0.924	0.722	0.733	0.640	0.542	0.543	0.656	0.677

Chapter 3

Photometric results analysis

In this Chapter the starspot variability effect will be estimated, allowing us to quantify the corresponding perturbations on the photometric transit depth. At first I will present the results of stellar colours analysis on the reference systems. Then I will discuss the application of the previous theoretical approach, proposed to analyse a synthetic photometric planetary transit in presence of starspots, to four real planetary systems.

3.1. Influence of stellar activity on stellar colours

By considering the first and the fourth case in Table 3.2 (i.e., the hottest and the coolest host stars) and by fixing the filling factor f_0 to 1% (i.e., larger than in the solar case, but comparable to those observed in late-type moderately active stars), I can compute the relative variation in the system flux ($\Delta F/F$) in the U and K-bands, to compare the influence of stellar activity in the optical and infrared passbands.

For the first case ($T_\star = 5750$ K, $\Delta T = 1250$ K), I derive the variations in the U-band and in the K-band, respectively, to be

$$\Delta F_U/F_U = 9 \cdot 10^{-3} \quad \text{and} \quad \Delta F_K/F_K = 3 \cdot 10^{-3}. \tag{3.1}$$

For the fourth case ($T_\star = 3750$ K, $\Delta T = 1250$ K), I derive the following values in the U-band and in the the K-band, respectively,

$$\Delta F_U/F_U = 1 \cdot 10^{-2} \quad \text{and} \quad \Delta F_K/F_K = 6 \cdot 10^{-3}. \tag{3.2}$$

The decrease in flux caused by a spot filling factor of 0.01 is comparable to the decrease produced by the transit of a Jupiter-sized planet in front of the stellar disc. I can compare the obtained reductions in flux of the systems due to stellar magnetic activity, using the information in Table 2.1, with the decrease in magnitude due to the transit of a planet, reported in Table 3.2.

Table 3.1: Variation in the colours of the system for all the cases. *Top*: computed for $f_0 = 0.1$. *Bottom*: computed for $f_0 = 0.01$.

$f_0 = 0.1$	$\Delta(\mathrm{F}_V/\mathrm{F}_I)$	$\Delta(\mathrm{F}_V/\mathrm{F}_K)$	$\Delta(\mathrm{F}_V/\mathrm{F}_{8.0})$
1)	1.5%	4.9%	5.4%
2)	2.0%	4.2%	5.0%
3)	1.8%	4.2%	4.7%
4)	0.7%	3.8%	3.4%
$f_0 = 0.01$	$\Delta(\mathrm{F}_V/\mathrm{F}_I)$	$\Delta(\mathrm{F}_V/\mathrm{F}_K)$	$\Delta(\mathrm{F}_V/\mathrm{F}_{8.0})$
1)	0.14%	0.48%	0.53%
2)	0.19%	0.41%	0.49%
3)	0.17%	0.40%	0.45%
4)	0.07%	0.35%	0.32%

The transit of a spot or a group of spots (or an active region in general) on the star surface induces a colour variation in the star. Since spots are cooler than the stellar photosphere, the colour indices are higher. In principle, we can infer the activity of a star by monitoring the variation in the colours for some specified wavebands. Star colours depend on the ratio of the fluxes in two selected passbands. For this purpose, I compute the ratio of the system fluxes in the optical and the infrared passbands, for all the four template cases, represented by $F_{\mathrm{V}}/F_{\mathrm{I}}$, $F_{\mathrm{V}}/F_{\mathrm{K}}$, and $F_{\mathrm{V}}/F_{8.0}$. Table 3.1 reports the variation in $F_{\mathrm{V}}/F_{\mathrm{band}}$ in the different bands, by fixing the filling factor f_0 to either 0.1 and to 0.01, respectively. The first column shows the filling factors and the enumeration of the cases, and the subsequent columns show the changes in $F_{\mathrm{V}}/F_{\mathrm{I}}$, in $F_{\mathrm{V}}/F_{\mathrm{K}}$, and in $F_{\mathrm{V}}/F_{8.0}$, respectively. The behaviour of the star flux ratios vs. spot filling factor of the unocculted spots are plotted in Fig. 2.4, where the ratios decrease as the spot filling factor increases.

3.1.1. Characterization of a single light curve dip

The transit of a planet without atmosphere induces a relative decrease in the stellar flux that depends on the mean wavelength of the passband owing to the wavelength dependence of the stellar limb darkening. For the present application, I consider the central transit ($b = 0$) of a small planet $(R_{\mathrm{p}}/R_\star) \lesssim 0.1$, with the quadratic limb-darkening law of Eq. (2.3). I derive the ratio $\mathcal{R}$ of the relative depths of the transit at the mean wavelengths of two different passbands, say U and K

$$\mathcal{R} \equiv \frac{\Delta F_U/F_U}{\Delta F_K/F_K} = \frac{1 - \frac{1}{3}u_{1K} - \frac{1}{6}u_{2K}}{1 - \frac{1}{3}u_{1U} - \frac{1}{6}u_{2U}}, \tag{3.3}$$

where u_{1U}, u_{2U}, u_{1K}, and u_{2K} are the limb-darkening coefficients in the U and K passbands, derived from, e.g., Diaz-Cordoves et al. (1995) and Claret et al. (1995), respectively. For the first case, $\mathcal{R} = 1.298$, whereas for the fourth case,

$\mathcal{R} = 1.197$. This is significantly smaller than expected in the case of the variations induced by dark spots (cf. Eqs. (3.1) and (3.2)). The flux in the K passband coming from the night-side of the planet during the transit is neglected because the planet temperature, even for the most strongly irradiated objects, is always lower than ∼2000 K, which is remarkably lower than the temperature of the starspots.

Considering Eq. (2.2), the ratio of the variations induced by starspots is

$$\mathcal{R}_{\mathrm{s}} = \frac{A_U}{A_K}. \tag{3.4}$$

For a stellar effective temperature of 5750 K, this is always significantly greater than 1.3, except for very cool spots, i.e. $\Delta T \geq 2100$ K. Spots so cool are generally not observed in active stars (see, e.g., Berdyugina 2005). For the Sun as a star, $\Delta T \simeq 500 - 600$ K because sunspot irradiance is dominated by the penumbral regions (cf., e.g., Lanza et al. 2004, and references therein). For a star with $T_\star = 3750$ K, a spot temperature deficit $\Delta T \geq 1500$ K is required to produce a $\mathcal{R}_{\mathrm{s}}$ that is comparable to that of a planetary transit, which is also unlikely for such a cool star (see, e.g., Berdyugina 2005, Zboril 2003).

In conclusion, even for an individual light curve dip, it is possible to compare the variation in the depths in the optical and infrared passbands to discriminate between an effect induced by spot activity and a planetary transit, because the ratio $\mathcal{R}$ is in the range $1.7 - 3.0$ in the former case (see the ratio of relations in Eqs. (3.1) and (3.2), for a typical $\Delta T = 1250$ K), while it is around $1.2 - 1.3$ in the latter case.

The photometric precision currently achievable from the ground in the near-infrared is generally sufficient for an application of the present method, provided that the photometric variations are at least $0.005 - 0.01$ mag. Croll et al. (2011) acquired photometry with a standard deviation of $\sigma \simeq 5 \times 10^{-3}$ mag in the J (1.25 μm) and the K (2.15 μm) bandpasses using the Wide-field InfraRed Camera (WIRCam) at the 3.5-m Canada France Hawaii Telescope (CFHT), while Tofflemire et al. (2011) reached a photometric stability of 3.9×10^{-3} mag in one hour and 5.1×10^{-3} mag in one night in the $\mathrm{K_s}$ passband at 2.224 μm observing stable M-type stars. However, the situation is remarkably different in the mid and far infrared passbands. From space, the *Warm Spitzer* mission has reached a statistical error of 450 ppm (parts per million) per minute, observing GJ 1214 for 12 sec at 3.6 μm (Gillon et al. 2011). However, the infrared observations are affected by systematic effects that may compromise the measurements because these effects induce flux variations comparable to the depth of a planetary transit. For example, the 3.6 and 4.5 μm *Spitzer*/IRAC channels (InSb detectors) are affected by the pixel-phase effect (see Sect. 1.4.1) which may cause a flux peak-to-peak amplitude of up to ∼1% (Beaulieu et al. 2008, Hébrard et al. 2010) or even higher (Désert et al. 2011b, Fressin et al. 2011), according to the exposure time. The light curves of the 5.8 and 8.0 μm channels (Si:As detectors) are affected by the ramp effect (see Sect. 1.4.1) which produce mmag level flux variations in photometry.

In order to apply the proposed method in the optical and the near-ultraviolet, the required photometric precision would be ~0.01 mag. The current space and ground missions allow us to reach this accuracy level. From space, the *CoRoT* and *Kepler* missions have been launched with the clear purpose of searching extra-solar planets via optical photometric transit light curves, thus they have been conceived to obtain precise photometric signals: *CoRoT* may reach 7.1×10^{-4} mag in one hour (Moutou & COROT/Exoplanet Team 2003), and *Kepler* is able to detect a photometric signal of 80 ppm on timescales up to ~2 days (Caldwell et al. 2010). The systematics in their data may be successful removed without affecting too much their high perfomances (see, e.g., Aigrain et al. (2009), Mazeh et al. (2009), for *CoRoT* systematics, and Caldwell et al. (2010), for *Kepler* systematics). The photometry in near-ultraviolet wavelengths can achieve the same level of accuracy. In fact, with *HST*/STIS ($290-1030$ nm), Knutson et al. (2007b) obtained a photometric accuracy comparable to that of Brown et al. (2001), i.e. 1.2×10^{4} mag for an integration time of 60 sec. With *HST*/STIS ($290-570$ nm) Sing et al. (2011b) managed to detect a $\sim 2-4$ mmag spot-like signature in the light curve of HD 189733 b; since no facular occultation was observed, the authors neglected its contribution in the light curve. Even ground-based observations in U-band allow high photometric accuracies, in fact Turner et al. (2012) analysed an observation of the transiting extra-solar planet TrES-3 b, made with the Steward Observatory 1.55-m Kuiper in Arizona, obtaining an average photometric precision of 3.7×10^{-3} mag with a photometric cadence of 68 sec.

3.2. Example applications to four real cases

In this section I apply my results to real observed cases, four systems with planets, i.e., CoRoT-12, with a transiting Jupiter-like planet orbiting around a G2V star (see Gillon et al. 2010), CoRoT-7, a K0V star hosting two Super-Earth planets, CoRoT-7 a and CoRoT-7 b (on which I am mainly interested) (Léger et al. 2009, Queloz et al. 2009), HAT-P-20, a K7V star with a transiting massive planet (Bakos et al. 2011), and GJ 436, a M2.5 dwarf star harbouring a transiting Neptune-mass planet (Butler et al. 2004). I list their properties, along with those of the related reference stellar systems, in Table 3.2, where I give, from left to right, the spectral type, the selected temperature for the quiet photosphere and spot for the reference stars, the difference between the photosphere and spot temperatures, the real system with the name of the star we use for comparison, the stellar spectral type, the planetary radius and mass, and the observed reduction in flux at mid planetary transit, expressed in magnitudes (obtained as the square of the ratio of the planet radius to the star radius), respectively.

3.2.1. Influence of stellar activity on planetary radius determination

I apply the formulae of Sect. 2.1.3 to evaluate the variation in the apparent planetary radius in the presence of starspots, assuming that the other parameters are not affected. The plots in Fig. 3.1, $\Delta R_\mathrm{p}/R_\mathrm{p}$ vs. wavelength, give the overestimate on R_p if the effect of unocculted starspots is neglected for the considered four reference cases. I find a relation both between $\Delta R_\mathrm{p}/R_\mathrm{p}$ and the wavelength and between $\Delta R_\mathrm{p}/R_\mathrm{p}$ and the stellar activity, i.e., increasing the filling factor of the out-of-transit spots f_0 the dashed curves shift upwards and the variation decreases towards longer wavelengths. The filled circles on the plots indicate the correction to the observed planetary radius that I have to apply to get the true radius of the planet for the examined spot temperature and filling factor value (see below).

The top left panel of Fig. 3.1 presents the results for CoRoT-12. I assumed a filling factor of $f_0 = 0.03$ (the solid line in the panel) by inferring the flux variation from the CoRoT light curve of Fig. 1 in Gillon et al. (2010) and then derived the contrast coefficients from the first row of Table 2.1.

The top right panel of Fig. 3.1 shows $\Delta R_\mathrm{p}/R_\mathrm{p}$ vs. wavelength for CoRoT-7. The spot filling factor value is $f_0 = 0.04$ by deducing it from the optical flux variability reported in Lanza et al. (2010).

For HAT-P-20, the outcomes are shown in the bottom left panel of Fig. 3.1. I set $f_0 = 0.01$ as derived by the magnitude variations in the stellar flux for the R-band shown in Fig. 1 in Bakos et al. (2011). The dependences of $\Delta R_\mathrm{p}/R_\mathrm{p}$ on both the wavelength and the stellar activity are also clearly visible for this planet too, even though the curves tend to become flat.

The bottom right panel of Fig. 3.1 shows the results for GJ 436. The star is a relatively quiet source showing photometric variations of the order of the millimag (Butler et al. 2004). Demory et al. (2007) found that the photometric irregularities in the light curve of GJ 436, detected with the EULER Telescope, are caused by an unocculted starspot and they computed a spot filling factor of 1%, which is compatible with the dispersion in the HARPS radial velocity. Thus, I set $f_0 = 0.01$.

Table 3.3 lists the obtained results taking into account the above filling factor values: from the left to the right, the planet name, $\Delta R_\mathrm{p}/R_\mathrm{p}$, and the relative variation in the radius uncertainty ΔErr, which is the ratio of the computed ΔR_p

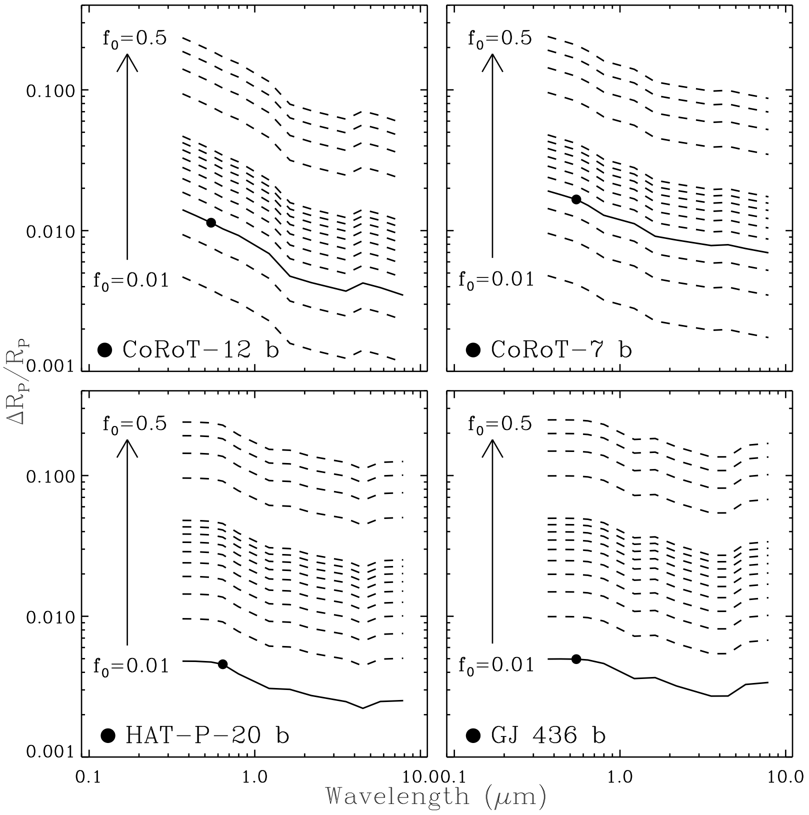

Figure 3.1: Relative variation in the apparent planetary radius vs. Wavelength for all the examined planetary systems. In the *top left*, we present the results for CoRoT-12 b, in the *top right* for CoRoT-7 b, in the *bottom left* for HAT-P-20 b, and in the *bottom right* for GJ 436 b, assuming various levels of activity. The dashed curves, from the bottom to the top, correspond to increasing filling factor values, as indicated on the left of each plot. The solid curves refer to the activity levels as actually estimated for the specified systems. The filled points indicate the position of the observed planets, as described in the text.

with respect to the uncertainties quoted in the literature[1] (see also Table 3.2). By a simple check, one note that the largest values of $\Delta R_{\rm p}/R_{\rm p}$ and ΔErr occur for the most active star within our sample, i.e. CoRoT-7 with $f_0 = 0.04$, while the lowest values are found for the coolest and less active stars, i.e. HAT-P-20 and GJ 436 with $f_0 = 0.01$ in both cases. For CoRoT-7 b, I compute an overestimate of the planetary radius, $\Delta R_{\rm p}$, of about 180 km at optical wavelengths (with a relative variation in the radius uncertainty of about 31%), while in the K-band it is about 92 km and even smaller at *Spitzer*/IRAC wavebands (at 3.6 μm, $\Delta R_{\rm p} \simeq 84$ km

---

[1] See site http://exoplanet.eu/index.php.

and at 8.0 μm $\Delta R_{\mathrm{p}} \simeq 75$ km). This decrease in ΔR_{p} as wavelength increases is exhibited by the other examined planetary systems and could be misinterpreted as evidence of a planetary atmosphere with a wavelength-dependent absorption. Since ΔR_{p} is proportional to the planetary radius, the largest ΔR_{p} is obtained for CoRoT-12 b ($\Delta R_{\mathrm{p}} \simeq 1180$ km at optical wavelengths) with a Jupiter-like planet and the lowest for GJ 436 b ($\Delta R_{\mathrm{p}} \simeq 130$ km in the optical) with its super-Earth planet. Nevertheless, all the radius increments calculated in this work fall inside the error bars quoted in the literature, thus no correction to the presently determined planetary parameters is required. Furthermore one can see that for each value of the filling factor, the curves seem to start nearly at the same level (i.e. $\Delta R_{\mathrm{p}}/R_{\mathrm{p}} \simeq 0.005$ for $f_0 = 0.01$ and $\Delta R_{\mathrm{p}}/R_{\mathrm{p}} \simeq 0.24$ for $f_0 = 0.5$), independently of the stellar photospheric temperature. Their trends remain monotonic but their slopes decrease towards cooler photospheric temperatures (cf. GJ 436, in the bottom right panel of Fig. 3.1). This indicates that the overestimate of the planetary radius depends on the wavelength, with the dependence being steeper for solar-type stars and flatter for later spectral types.

Specifically considering the *Spitzer* passbands, I apply the method described above to two of the most studied planetary systems: HD 209458 and HD 189733. These systems have been the objects of intense study at a wide range of wavelengths from the optical with the *HST* (Brown et al. 2001, Knutson et al. 2007b, Pont et al. 2007, Sing et al. 2011b) to the infrared with the *Spitzer* satellite (Richardson et al. 2006, Ehrenreich et al. 2007, Tinetti et al. 2007b, Beaulieu et al. 2008, 2010, Désert et al. 2011a), also as targets for transmission spectroscopy thanks to their brightness.

Table 3.4 reports the results and presents the corresponding ones for GJ 436 b for comparison. In all cases, I have considered two different filling factor values for the unocculted spots: one is that derived as described below, while the other one is given for comparison (indicated in parenthesis in the Table).

HD 209458 is an almost quiet solar-like G0V star and the calculations have been made considering the two configurations $f_0 = 0.004$ and $f_0 = 0.03$. The former f_0 value was estimated assuming a circular spot with an average radius of 4.5×10^4 km as in the model proposed by Silva (2003) to fit the distortion of a single transit of HD 209458 observed by *HST*. HD 189733 is an active early-K star with $f_0 = 0.03$ (Désert et al. 2011a). To derive the quantities, I interpolated the BaSeL spectra at temperatures corresponding to the stellar effective temperatures ($T_{\mathrm{eff}} = 6000$ K and $T_{\mathrm{eff}} = 5000$ K for HD 209458 and HD 189733, respectively) and assuming $\Delta T = 1250$ K for both cases. Table 3.4 also lists the measured planetary radius and the related uncertainty, as reported in the literature.

Fig. 3.2 shows the corrected planetary radii vs. wavelength, along with the uncertainties reported in the literature. The adopted stellar radii are $R_{\mathrm{HD\ 209458}} = 1.146\ R_{\odot}$ (Brown et al. 2001), $R_{\mathrm{HD\ 189733}} = 0.788\ R_{\odot}$ (Baines et al. 2008), $R_{\mathrm{GJ\ 436}}$

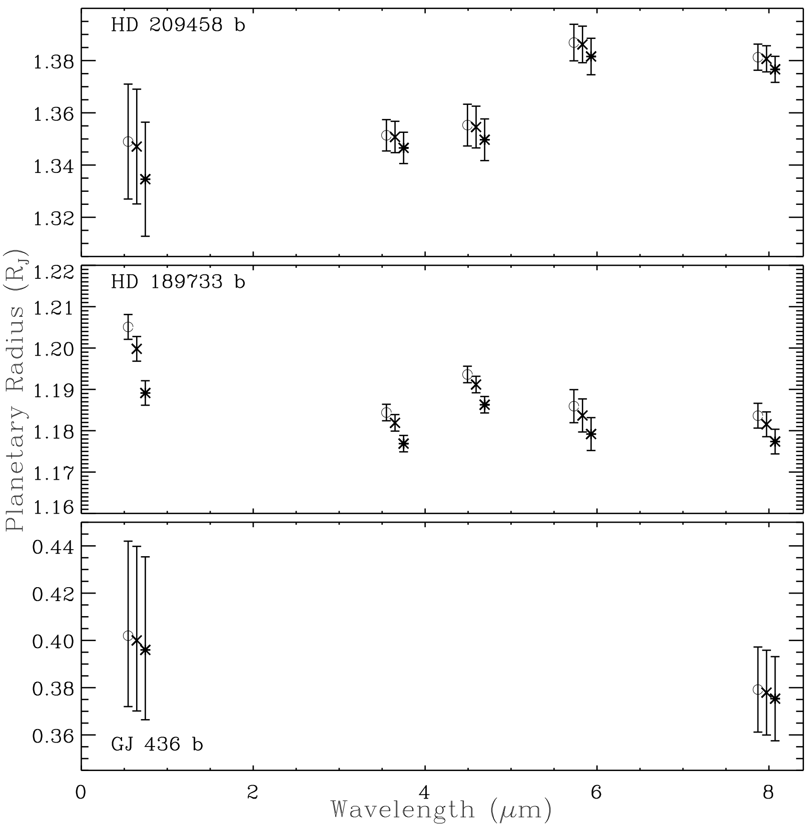

Figure 3.2: Corrected planetary radii vs. Wavelength. *Top panel*, HD 209458 b. *Middle panel*, HD 189733 b. *Bottom Panel*, GJ 436 b. The open circle $\circ$ indicates the planetary radius inferred from the literature, the cross $\times$ the corrected radius with $f_0 = 0.004$ for HD 209458 b and $f_0 = 0.01$ for HD 189733 b and GJ 436 b and the asterisk $*$ the corrected radius with $f_0 = 0.03$. The plotted points are shifted horizontally for an easier identification.

$= 0.464\ R_\odot$ (Torres 2007), respectively. The most active star (i.e., HD 189733) shows significant discrepancies between the planet radius inferred from the literature and the one determined here; this is an expected result since $\Delta R_\mathrm{p} \propto f$ (see Eq. (2.12) in Sect. 2.1.3) and may have interesting consequences if one wishes to characterize the planet atmosphere through transmission spectroscopy. Similarly, in the quiet cases, even though our corrections are within the error bars reported in the literature (of the order of the hundreth or of the thousandth, see Table 3.4), they may become significant for the determination of the physical properties of similar exoplanets. The wavelength dependence of the apparent radius of HD 189733 b in the optical passbands was observed by Sing et al. (2011b). They used an approach similar to that of Sect. 2.1.3 and concluded that the variation in $R_\mathrm{p}/R_\star$ vs. wavelength λ cannot be reproduced by an equation analogous to Eq. (2.13), thus providing evidence of the wavelength dependence of the planetary atmospheric absorption.

3.2.2. Effects of stellar activity on orbital parameters

To illustrate the impact of starspots on the determination of all the transit parameters, I considered the case of CoRoT-2 because it had been studied by Czesla et al. (2009) and its spot activity had been investigated in detail. Since my interest is in the systematic errors produced by starspots, I simulated a noiseless transit profile by adopting the time sampling and the parameters derived by Alonso et al. (2008), and applied Eq. (2.8) with spot filling factors estimated from Lanza et al. (2009) for the out-of-transit light curve and Silva-Valio et al. (2010) for the transit light curve, respectively. To derive the transit profile to be fitted with their model, Alonso et al. (2008) averaged all the transits observed by CoRoT. Therefore, I assumed that the spot perturbation corresponds to the average values of the filling factors f_0 and f_i as derived from the modelling of the out-of-transit and the transit light curves, respectively. By fitting the light curve of CoRoT-2 outside transits, Lanza et al. (2009) derived an average spot filling factor $f_0 = 0.07$ by adopting a spot contrast in the CoRoT white passband of $A_\mathrm{LANZA} = 0.665$. On the other hand, Silva-Valio et al. (2010) found an average filling factor of $f_\mathrm{i} = 0.15$ for a spot contrast of $A_\mathrm{SILVA} = 0.55$. Multiplying it by the ratio $A_\mathrm{LANZA}/A_\mathrm{SILVA}$, I converted it into the scale of Lanza et al. (2009), giving $f_\mathrm{i} = 0.18$. With those values of the filling factors and $A_\lambda = 0.665$, I computed the unperturbed transit profile D_0 from Eq. (2.8) and then fitted it with the Levenberg-Marquardt algorithm as implemented in the IDL procedure LMFIT. The unperturbed transit profile and its best fit are plotted in Fig. 3.3 together with the initial profile assumed to be perturbed by the effects of the spots. The best fit has a reduced $\chi^2 = 1.29$ computed by assuming a relative standard deviation of the simulated data of 1.09×10^{-4} as in the case of the CoRoT data analysed by Alonso et al. (2008). The best-fit parameters and their standard deviations derived from the covariance matrix with the above assumed data standard deviation (see Press et al. 1992, §15.4) are $a/R_\star = 6.76 \pm 0.03$, $R_\mathrm{p}/R_\star = 0.1726 \pm 0.00006$, $i = 88\overset{\circ}{.}44 \pm 0\overset{\circ}{.}18$, $u_1 = 0.40 \pm 0.04$, and $u_2 = 0.097 \pm 0.04$. The comparison between these estimates and those found by Alonso et al. (2008) is reported in Table 3.5.

I confirmed that the radius variation is close to that estimated with the simple approach of Sect. 2.1.3 because the depth of the profile at mid-transit gives the principal constraint on the relative radius. However, in contrast to the results of Czesla et al. (2009), I found that the relative semi-major axis $a/R_\star$ and the inclination i are also affected, with variations that exceed three standard deviations for both parameters (see Table 3.5). The transit duration t_T is the

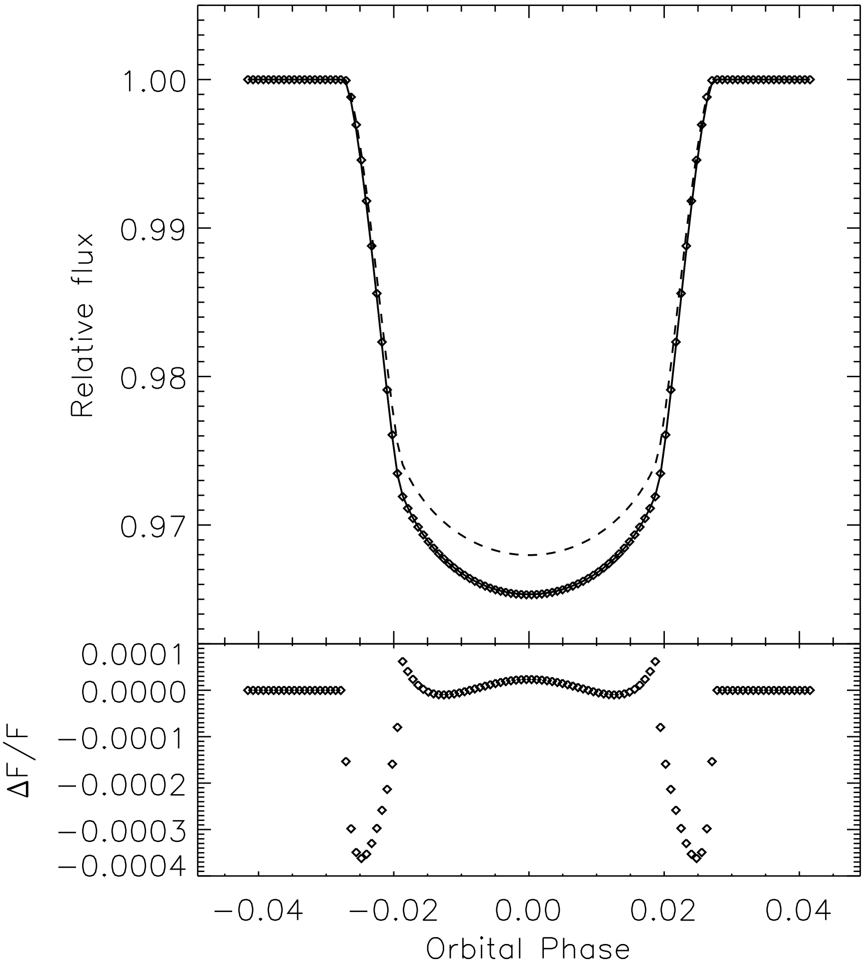

Figure 3.3: *Top panel*: the synthetic light curve of the transit of CoRoT-2 computed with the parameters in Table 1 of Alonso et al. (2008) (dashed line) together with the unperturbed profile obtained from Eq. (2.8) (diamonds) and the corresponding best fit (solid line). The flux is measured in units of the out-of-transit flux level in all the cases. *Bottom panel*: the residuals of the best fit to the unperturbed transit profile in relative flux units vs. the orbital phase.

same in the adopted model for both the unperturbed and the perturbed transit profiles. Therefore, the variations in $a/R_\star$ and i combine with each other to ensure that t_T remains practically constant (see Sect. 2.1.4). In addition, as already mentioned in Sect. 1.4.1, the variation in $a/R_\star$ has an impact on the measurement of the density of the star. Even if this application is beyond the scope of the present work, I conclude that starspot effects cannot be neglected in the derivation of the stellar density from the transit fitting in the case of active planetary hosts.

The limb-darkening parameters were not significantly affected by the stellar variability. The small systematic deviations in the ingress and egress of the profile do not lead to any significant adjustment of the limb darkening (cf. upper and lower panels of Fig. 3.3). In general, in the analysis of exoplanet transiting light curves, the limb-darkening effect is assumed as a matter of fact, but actually LDCs may show a dependence on the outcome of the transit fits (Sing 2010). This may provide a unique opportunity to make a comparison between the values obtained observationally and those obtained through stellar atmosphere models, even if such a correspondence is not so trivial. In this respect Howarth (2011) investigates the dependence of LDCs on impact parameter, b, and finds a correlation. The subtle dependence of LDCs from starspots would require the re-computation of LDCs once the correct value of the planetary radius is known (Sing 2010).

Other stellar parameters can be affected by starspots, notably the effective temperature $T_{\rm eff}$ and the stellar rotation period. The first problem was discussed in detail for CoRoT-2 by Guillot & Havel (2011) who found that the effect of spots is that of increasing the uncertainty in the determination of $T_{\rm eff}$ because of their changing covering factor along the activity cycle of the star. The second problem was analysed for CoRoT-2 by Silva-Valio et al. (2010) and Huber et al. (2010) by using the longitude shift of the same occulted starspot measured on two successive planetary transits but this kind of measurement might be significantly affected by the starspot evolution timescales for the considered system. I did not consider these aspects further because I focused on the parameters directly related to the modelling of multiwavelength observations of just one transit light curve.

Table 3.2: Examined cases and their related real planetary systems. In the synthesized models the metallicity and gravity values are the solar ones.

	Reference systems				*Real systems*					
Case	Spectral Type	$T_\star$ (K)	T_s (K)	ΔT (K)	Star name	Spectral Type	R_p (R_J)	M_p (M_J)	Δm	Refs.
1)	Early-G	5750	4500	1250	CoRoT-12	G2V	1.44 ± 0.13	0.917	0.018	(1)
2)	Early-K	5250	4000	1250	CoRoT-7	K0V	0.15 ± 0.008	0.0151	$3.14{\cdot}10^{-4}$	(2)
3)	Mid-K	4500	3250	1250	HAT-P-20	K7	0.867 ± 0.033	7.246	0.016	(3)
4)	Early-M	3750	2500	1250	GJ 436	M2.5	0.365 ± 0.02	0.0737	$6.53{\cdot}10^{-3}$	(4)

References: (1) Gillon et al. (2010); (2) Léger et al. (2009); (3) Bakos et al. (2011); (4) Torres (2007).

Table 3.3: The relative variation in planetary radius and radius uncertainty computed at the corresponding wavelengths for the analysed planetary systems, see text.

Planet Name	$\Delta R_p/R_p$	ΔErr
CoRoT-12 b	$1.14 \cdot 10^{-2}$	13%
CoRoT-7 b	$1.67 \cdot 10^{-2}$	31%
HAT-P-20 b	$0.46 \cdot 10^{-2}$	12%
GJ 436 b	$0.50 \cdot 10^{-2}$	10%

Table 3.4: Corrected planetary radii in the optical and *Spitzer* wavebands for three notable examples: HD 209458 b, HD 189733 b, and GJ 436 b.

Planetary systems	Bands	$R_{\rm corr}$ (R_J)	$R_{\rm corr}$ (R_J)	$R_{\rm lit}$ (R_J)	Ref.
		$f_0 = 0.004$	($f_0 = 0.03$)		
HD 209458 b	V	1.347	(1.335)	1.349±0.022	(1)
	3.6 μm	1.351	(1.347)	1.351±0.006	(2)
	4.5 μm	1.355	(1.350)	1.355±0.008	(2)
	5.8 μm	1.386	(1.382)	1.387±0.007	(2)
	8.0 μm	1.381	(1.377)	1.381±0.005	(2)
		($f_0 = 0.01$)	$f_0 = 0.03$		
HD 189733 b	V	(1.200)	1.189	1.205±0.003	(3)
	3.6 μm	(1.182)	1.177	1.184±0.002	(4)
	4.5 μm	(1.191)	1.186	1.194±0.002	(4)
	5.8 μm	(1.184)	1.179	1.186±0.004	(4)
	8.0 μm	(1.182)	1.177	1.184±0.003	(4)
		$f_0 = 0.01$	($f_0 = 0.03$)		
GJ 436 b	V	0.400	(0.396)	$0.402^{+0.036}_{-0.027}$	(5)
	8.0 μm	0.378	(0.375)	0.379±0.018	(6)

References: (1) Knutson et al. (2007b); (2) Beaulieu et al. (2010); (3) Pont et al. (2007); (4) Désert et al. (2009); (5) Bean et al. (2008); (6) Deming et al. (2007).

Table 3.5: Comparison between the CoRoT-2 parameter values obtained by Alonso et al. (2008) and those derived in this work.

Parameters	Alonso et al. (2008)	This work
$a/R_\star$	6.70±0.03	6.76±0.03
$R_p/R_\star$	0.1667±0.0006	0.1726±0.00006
i (deg)	87.84±0.10	88.84±0.18
u_1	0.41±0.03	0.40±0.04
u_2	0.06±0.03	0.097±0.04

Chapter 4

Conclusions

In the light of the previous results, in this Chapter I will present the final remarks. The fundamental conclusions are that the stellar magnetic activity is a source of noise in the search for extrasolar transiting planets, even for star with moderate level of activity, and that the colour dependence of stellar activity may significantly influence the characterization of planetary atmospheres through transmission spectroscopy.

4.1. On stellar colours

In Sect. 3.1, I analysed the photometric stellar variations due to starspots and compared them with the photometric stellar variations due to a transiting planet. As stated before, the first situation is colour dependent owing to the temperature differences between stellar photospheres and spots, whereas the second situation has to be considered colour independent. So if we had a broad-band monitoring of stars hosting planets, in principle by observing the variations of relative flux in different wavebands, we could discriminate whether the variations are due to the occurrence of starspots or of a transiting planet. Here I am assuming that the transiting planet night-side does not contribute in the integrated system fluxes being the planet temperature sufficiently low to be neglected in comparison with the spots temperatures. Thus under the same conditions, e.g., assuming that a starspot and a planet cover the same stellar chord with different timescales, by using from optical to infrared wavebands, we could distinguish their contribution to the system fluxes. Even in the case of a starspot occultation by the planet and thus the occurrence of a flux increase in the light curve (see the bump in the light curve in Fig. 1.20(c)), the flux difference between the bump peak level and the reference level should be the same in all wavebands and thus colour indipendent at the first order. However the detection of these effects depends on the available photometric accuracy.

These considerations, together with the results of Sect. 3.1, indicate that the stellar variability effects may be constrained by using broad-band observations and that it is easier to identify the transit of a Jupiter-like planet by analysing the light curve of the system in the infrared band (K-band), whereas it may be more problematic in the blue one (U-band). Instead the detection of a smaller planet is more challenging, in both the U and the K-band, since the photometric signal corresponding to the transit of such a planet is, as expected, smaller than the effect of the magnetic activity of its parent star. Fortunately, other properties of the variations, such as timescales or in fact colour dependences, may help in understanding the origin of the variations.

The timescales of the stellar flux variability and the transit are generally quite different, since the former may range from weeks to months as in the case of the Sun (Lanza et al. 2003, 2007), while the latter has a duration ranging from a few hours to a few tens of hours. However, there are situations in which the timescales can be comparable, e.g. for a young Sun-like star with a rotation period of, say, $1-2$ days transited by a planet at the distance of $\sim$1 AU, whose transit duration is of the order of $\sim 10-15$ hours. In this case, a discrimination of the origin of the light dip based on timescales is infeasible, while this approach is still applicable if simultaneous multiwavelength observations are available. The adopted method can be applied even to a single event and this can be very useful in the case of planets with orbital periods of several tens or hundreds of days.

4.1.1. On single light curve dip

In Sect. 3.1.1, I also proposed a simple method to characterize a single dip in a light curve, namely I demonstrated that the observation of moderately active stars simultaneously in the optical and the near-infrared passbands allows us to discriminate between planetary transits and activity-induced variations, unless starspots are $2000-2500$ K cooler than the unperturbed photosphere, which is generally not observed in main-sequence stars. It is possible to define the quantity $\mathcal{R}$, the ratio of the relative stellar flux variations in two widely separated wavebands, which assumes different numerical values in the two different configurations thus ensuring that we are not confusing the starspots noise and the exoplanet transiting signal, that is to say that $\mathcal{R}_{\rm s} > \mathcal{R}$ for the most extreme investigated cases, where $\mathcal{R}_{\rm s}$ and $\mathcal{R}$ are the ratios of the relative stellar flux variations due to starspots in U and K-band and due to a planetary transit, respectively. This approach has the advantage to be able to be applied to individual light-curve dips observed even with a signal-to-noise ratio of $\approx 10-15\%$ of the flux variations in two well-separated passbands, e.g. U and K, and does not require a characterization of the stellar microvariability timescales, which would require observations extended for at least $2-3$ stellar rotations in order to just remove the activity-induced effects.

To conclude, these results tend to emphasize the importance of a broad-band monitoring of stars hosting planets from the visible, at the shortest wavelength as possible, to IR. Such simultaneous observations of a significant sample of stars might themselves be a relevant tool for identifying and characterizing their stellar activity, allowing us to more clearly understand the role of stellar magnetic activity in the analysis of a transiting planet light curve by comparing the ratios $\mathcal{R}$ derived in Eqs. (3.3) and (3.4), as stated before, basically disentangling the stellar activity contribution from planetary transit signals.

4.2. On planetary radius determination

In Sect. 3.2.1, I pointed out that the relative variation in the apparent planetary radius is twofold dependent on stellar activity. The presence of starspots induces a wavelength and a filling factor dependence as shown in Eq. (2.12) and in Fig. 3.1. The results state that estimates of the planetary radii are more tentative for more active stars, i.e. the more active is the star, the more overestimated may be the inferred planetary radius. A deeper transit means giving the planet a larger radius (Jha et al. 2000, Désert et al. 2011b), resulting in wrong derivations of planetary quantities and ambiguous information concerning the presence of a planetary atmosphere. This effect may be constrained by monitoring the stellar colour variations in well-chosen passbands. For all examined cases (reported in Table 3.2 and Table 3.4) the planetary radii derived with the adopted method fall within the error bars in the literature but these estimations are still useful in the context of the spectroscopic characterization of a planetary atmosphere. In fact infrared observations are important for the derivation of the planetary radius and accordingly of the planetary density. The correction for the effects of starspots is necessary to avoid systematic errors in transmission spectroscopy, especially when comparing the planetary radii at optical (U or B-bands) and infrared passbands (J or K-bands). A correct determination of the planetary radius enables us to perform a more accurate study of the planetary atmosphere and its composition in the framework of transmission and reflection spectroscopy. In this sense I provided simple formulae, tabulations, and graphics useful to estimate the starspot perturbation for typical transiting systems.

4.3. On orbital parameters

In Sect. 3.2.2, I described that starspots may affect prominent orbital parameters, e.g., the relative semi-major axis $a/R_\star$ and the orbital inclination angle i, derived by the transit fitting procedure. As already suggested by Jha et al.

(2000) and Sozzetti et al. (2007), one deduces that the quantities directly derived from the light curve fit of a transiting planet may be crucial for the derivation of stellar radius and masses. This has a non-negligible impact on the determination of the stellar density especially when using optical light curves that are more perturbed by activity-induced effects. Near-infrared light curves are less affected, but the effect may still be significant for very active stars.

In conclusion, simultaneous broad-band photometric observation, from visible to infrared wavelengths are useful to derive relevant and accurate information about the primary parameters of the stars hosting planet providing tighter constraints on stellar evolutionary tracks and luminosities.

4.4. Future perspective

This thesis reports on the effects of stellar flux variabilities on the current capability of detecting photometrically a transiting planet. Currently I have developed an IDL code that allows me to combine synthetic stellar spectra to obtain a star+spot flux, on which observe wavelength effects due to the temperature differences between the unperturbed photosphere and the spotted one (see Chapter 2), by adopting the BaSeL stellar libraries as synthetic stellar spectra.

In this section I introduce some aspects that might be interesting in order to extend the adopted approach to the spectroscopic characterization of transiting planets.

The simultaneous photometric and spectroscopic analysis may be clearly useful to better constrain the features of stellar flux variations. On one hand, the performed photometric study is able to separate the activity-induced effects from the planetary transit signal by calculating the $\mathcal{R}$ parameter and comparing it with an analogous stellar flux ratio in two well-separated passbands, as explained in Chapter 3. On the other hand, a tentative spectroscopic study may lead to the identification of which molecular or atomic features are influenced by activity-induced effects, by changing their equivalent widths (EW) as a function of the temperature of lines formation and spot filling factor. In principle this may also help to provide a correlation between the EW perturbation and the spotted photosphere temperature. This approach might be performed by comparing several synthetic combined spectra (star+spot), by keeping fixed $T_\star$ and changing $T_{\rm spot}$ and the filling factor values, with observed stellar spectra.

By simulating the spectral resolution of observed spectra and fixing the wavelength range where one wants to investigate (with the minimum and maximum wavelength), the spectroscopic section of the IDL code would be significantly useful to compare synthetic and observed stellar spectra, thus providing a further instrument of investigating the effects induced by the magnetic stellar activity and, together with the photometric section, would give a more complete and global view of the activity-induced effects intervening in the research of photometric transit of extra-solar planets.

Appendix A

IDL code for photometric analysis of transit light curve

In the following I will present the details of the procedure outlined in Chap. 2, by describing each step within it. The approach adopted is now extended to include photometry of the desired stellar systems exploring a wider range of stellar and configuration parameters: $T_\star$, $T_{\rm spot}$, stellar libraries, filter passbands, and wavelength binning.

Fig. A.1 represents the flow chart of the whole tool. The code works as follows. An external user has to provide a data file containing all the stellar required parameters, indicated within the top rectangular area: the effective stellar temperature $T_\star$, the spot temperature $T_{\rm spot}$, the surface gravity expressed as log g, the metallicity [M/H] (labelled as *metal*, in the chart), and the desired wavelength binning (labelled as *dlam*, in the chart). The primary aim is to characterize photometrically one or several stellar systems. The Table A.1 reports an example of the input parameters file for a specified combination of parameters.

The photometric analysis requires a file with transmittance vs. wavelength of filters passbands (the second area in the chart). To make this procedure more flexible the external user may select among several possibilities: the standard procedure filter file with all the filter transmittances (those of the original proce-

Table A.1: An example of the input file format, *param.dat*, with the chosen stellar parameters for the photometric tool.

$T_\star$ (K)	$T_{\rm spot}$ (K)	log$g$	*metal*	*dlam* (Å)
5750	4500	4.5	+0.0	10.0
5250	4000	4.5	+0.0	10.0
4500	3250	4.5	+0.0	10.0
3750	2500	4.5	+0.0	10.0

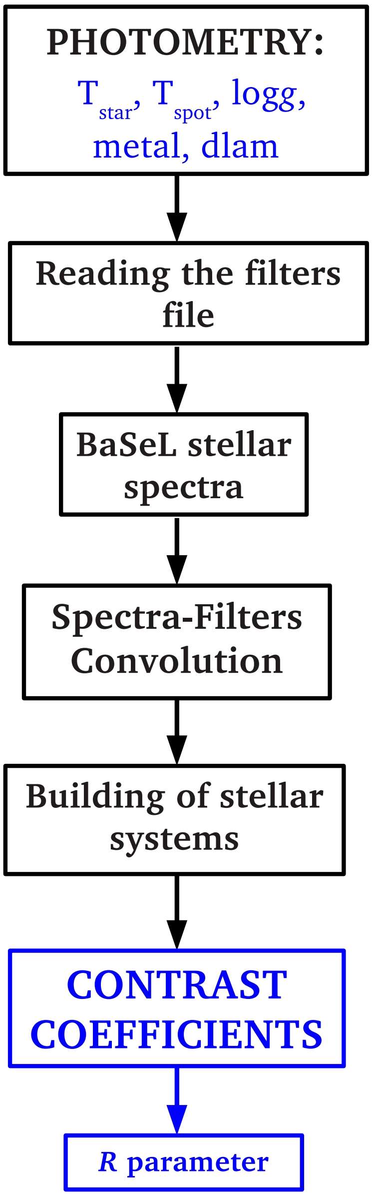

Figure A.1: Flow chart of the photometric tool with the needed stellar quantities.

dure), a combination of these fixed by the user, or an external transmittance file provided by the user himself. The first one is the set of filters passbands adopted in the analysis described in Sect. 2.1: the Johnson-Cousins-Glass photometric system (UBVRIJHK bands) and the *Spitzer*/IRAC wavebands (centered at 3.6 μm, 4.5 μm, 5.8 μm and 8.0 μm); the second possibility is a combination of the transmittance of filters decided by the user according to his aims; in the third case a specified file is provided by the user and may include whatever transmittance filters, as long as the related filters wavelengths fall within the wavelength interval

Table A.2: Example of a transmittance filters file for U and B-bands (Bessell 1990).

3000	0.000	3600	0.000
3050	0.016	3700	0.030
3100	0.068	3800	0.134
3150	0.167	3900	0.567
3200	0.287	4000	0.920
..	..	..	..
3900	0.625	5400	0.043
3950	0.423	5500	0.009
4000	0.238	5600	0.000
4050	0.114	*	*
4100	0.051	*	*
4150	0.019	*	*
4200	0.000	*	*

of stellar spectra. In these last case the filter file has to be written in a specified format, in order to run the procedure properly. An example of the file format is given in Table A.2, where only the U and B-bands are reported. The first two columns refer to U-band and the other two to B-band (the first column of each filter is the wavelengths, in Å, and the second column is the related transmittance values).

The next step is the selection of the stellar spectra with the specified parameters. The method outlined in Sect. 2.1 used the standard BaSeL libraries of synthetic spectra (Lejeune et al. 1997, 1998, Westera et al. 2002). It is a libraries of theoretical stellar spectra aimed to multiple synthetic photometry applications. Originally it was based on three original grids of model atmosphere by Bessell et al. (1989, 1991), Fluks et al. (1994), and Kurucz (1995), then in Lejeune et al. (1998) it was extended to include the M-dwarf model spectra of Allard & Hauschildt (1995), and finally, owing to its lack of robustness at low metallicities ([Fe/H] < -1), its colour calibration includes now non-solar metallicities (Westera et al. 2002). Since my primary aim was to analyse stellar system with solar-type stars (see the related parameters in Table 3.2), I used the BaSeL 2.2 version presented in Lejeune et al. (1998). In principle, the external user may enter stellar parameters needed for his research, in that case the allowed values of log g are -1.02, -0.7, -0.29, 0.0, 0.28, 0.5, 0.6, 1.0, 1.5, 2.0, 2.5, 3.0, 3.5, 4.0, 4.5, 5.0, 5.5, and the allowed values of [M/H] are -5.0, -4.5, -4.0, -3.5, -3.0, -2.5, -2.0, -1.5, -1.0, -0.5, -0.3, -0.2, -0.1, +0.0, +0.1, +0.2, +0.3, +0.5, +1.0. If some specified effective temperature values are required, this procedure allows to obtain the desired stellar spectra by interpolating the two adjacent spectra. Both the stellar spectra and the transmittance of the filters are interpolated in

Table A.3: Filling factor values considered in the proposed method.

0.00
0.01
0.02
0.03
0.04
0.05
0.06
0.07
0.08
0.09
0.1
0.2
0.3
0.4
0.5

wavelength through a wavelength grid obtained with the input *dlam* parameter. At this point, the procedure executes the convolution between the spectra and the filters in order to get the stellar flux densities for a specified passband (the fourth area in the chart). Then it builds the stellar system combining the star flux and the spot flux densities with the method described in Sect. 2.1.1, weighted by the filling factor values. These are provided by an ASCII file, containing only a column with the interesting values (see Table A.3). Since it is useful to observe how the stellar fluxes of a system star+spot change as a function of filling factor values, these values are held fixed throughout the procedure run.

Finally the procedure will produce a file containing all the results of the investigated systems. Fig. A.2 describes the actual results file obtained for a specified stellar system among those considered in Chap. 2. The first rows show the summary of the procedure run: the name of the stellar atmosphere and the number of used filters; then the chosen stellar system parameters, the vector containing the obtained contrast A_λ, already defined in Sect. 2.1.1, and the $\mathcal{R}_\mathrm{s}$ parameter computed for the specified star+spot system are listed.

```
CONTRAST RESULTS FROM THE TOOL
ADOPTED STELLAR LIBRARIES:  Basel
Filters Number:           12
----------------------------------------------
Contrast for the star+spot system:
Tstar (K):      5750.00
Tspot (K):      4500.00
Log g:      4.50000
metallicity:      0.00000
Wavelength Binning (angstrom):       10.000000
----------------------------------------------
0.93792605735025
0.85446669439646
0.75890663750266
0.68640604117786
0.61590343872952
0.45789441403870
0.31633760035559
0.28486927662964
0.24784950989413
0.28304525032536
0.26240609979999
0.23193059869904
----------------------------------------------
R = Au/Ak:       3.2924788
----------------------------------------------
```

Figure A.2: Example of the output results file for a specified star+spot system.

Appendix B

Transmission spectroscopy

The photometric transit technique allows to analyse an extra-solar planetary atmosphere and to determine its chemical composition through transmission spectroscopy, namely by measuring the planetary radius vs. wavelength. The observable quantity is thus $\mathcal{R}(\lambda)$, defined as the wavelength dependent ratio of the flux during a transit to that outside of transit (Brown 2001, Quirrenbach 2006)

$$\mathcal{R}(\lambda) \equiv \frac{\mathcal{F}_{\mathrm{transit}}(\lambda)}{\mathcal{F}_0(\lambda)}.$$

In presence of a transiting planet the observed stellar flux is essentially formed by two contributions, the stellar flux out of the planetary transit ($\mathcal{F}_0$), and the planetary contribution ($\delta\mathcal{F}$) depending on the orbital phase angle, φ (measured starting from the line of sight direction where $\varphi = 0$, and having the maximum value at the secondary eclipse where $\varphi = \pi$). Fig. B.1 gives an illustration of the geometry of a planetary orbit and the planet contribution to the system flux as a function of orbital phase. The relative change in stellar flux in presence of a transiting planet may be expressed as (Brown 2001, Quirrenbach 2006)

$$\mathcal{R}(\lambda) = \frac{\mathcal{F}_0(\lambda) + \delta\mathcal{F}(\lambda)}{\mathcal{F}_0(\lambda)}, \tag{B.1}$$

and, in its turn, $\delta\mathcal{F}$ is expressed as

$$\delta\mathcal{F} = \delta\mathcal{F}_{\mathrm{direct}} + \delta\mathcal{F}_{\mathrm{therm}} + \delta\mathcal{F}_{\mathrm{scat}}, \tag{B.2}$$

where the wavelength dependence is implicitly assumed. Thus three different factors contribute to the stellar flux density variations during the planetary orbit: $\delta\mathcal{F}_{\mathrm{direct}}$ is the variation in the stellar emission that reaches the observer directly, $\delta\mathcal{F}_{\mathrm{therm}}$ is the planet thermal emission contribution, and $\delta\mathcal{F}_{\mathrm{scat}}$ is the variation in the starlight radiation due to the planetary atmospheric reflection or scattering into the line of sight of the observer. The magnitude of the several terms in Eq. B.2 will be estimated as follows.

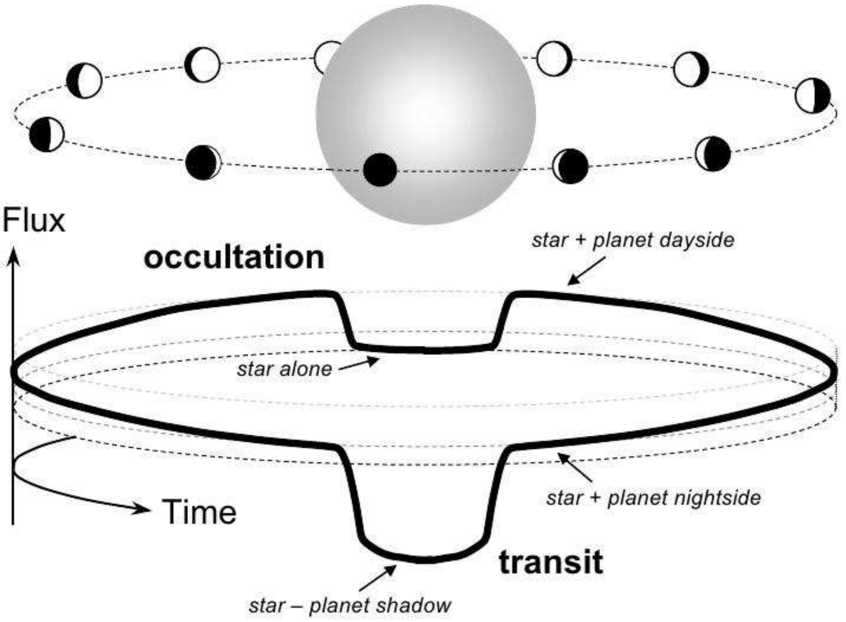

Figure B.1: Illustration of planetary transits and occultations with the combined star and planet flux at different phases of the orbit. The flux drops at two specific orbital phases: the transit and the occultation. In the first configuration, the planet hides a fraction of stellar radiation, in the second one the planet is occulted by its parent star. In intermediate phases the day-side and the night-side of the planet may be observed (Winn 2010).

The variation in the planet thermal flux as a function of orbital phase (the term $\delta\mathcal{F}_{\mathrm{therm}}$ vanishes at $\varphi = 180°$) implies to know the distribution of temperature across the surface area of the planet and thus the effectiveness of energy transport mechanisms between the night and day sides. According to the estimates of Brown (2001), for a planet having a mean temperature of 1400 K, a temperature difference of 200 K between the day and night side and considering the variations in projected area of the irradiated crescent when the orbital phase goes from 0° to 15°, then $\delta\mathcal{F}_{\mathrm{therm}}/\mathcal{F}_0$ results to be less than 10^{-4} for $\lambda \gtrsim 25$ μm. It is even smaller at shorter wavelengths.

Brown (2001) estimates the variation in scattered or reflected light as a function of orbital phase as well. At $\varphi = 0°$ and at $\varphi = 180°$, no scattered/reflected light has to be considered, since at the first orbital position only the dark side of the planet is observable, whereas at the occultation phase the planet disappears behind the star. At $\varphi = 15°$ only a thin illuminated slice is observable (see Fig. B.1). The relative scattered contribution may be expressed as (Sobolev 1975)

$$\frac{\delta\mathcal{F}_{\mathrm{scat}}}{\mathcal{F}_0} \simeq \frac{\alpha\pi R_{\mathrm{p}}^2(1 - cos\ \varphi)}{2\pi a^2},$$

where α is the planet's geometric albedo[1]. Assuming a Jupiter-like planet with $R_{\mathrm{p}} = R_{\mathrm{J}}$, $a = a_{\mathrm{J}}$, $\varphi = 15°$, and $\alpha = 1$, we obtain $\delta\mathcal{F}_{\mathrm{scat}}/\mathcal{F}_0 \simeq 10^{-7}$, thus the scattered contribution results negligible for almost all wavelengths.

The direct flux (i.e. the term $\delta\mathcal{F}_{\mathrm{direct}}$) may undergo changes due to intrinsic stellar variabilities or the occultation of a fraction of the star at the primary eclipse, thus vanishing at the secondary eclipse position (i.e., when $\varphi = 180°$). The activity-induced changes have been discussed in details in the preceding chapters where I pointed out that it is possible to separate the planetary transit signal from that of starspots, here I am focusing on the wavelength dependence of the star obscuration by a transiting planet. Planetary transit signals contain a Doppler imprint in the sense that the shape of spectral stellar lines changes during a transit since the planet obscures radiation coming from different parts of the stellar disc (Quirrenbach 2006) resulting in a center-to-limb dependence of the stellar spectrum lines (Brown 2001). This may derive from several factors: different lines may be formed at different depths in the stellar atmosphere, anisotropies in the photosphere, and the bulk rotation of the star. During the first half of a central transit, the planet blocks the approaching side of the star red-shifting the spectral lines, whereas, during the second half, the planet passes in front of the receding side of the star thus blue-shifting the spectral lines. This selective occultation produces an anomaly in the wings of spectral lines that may be problematic for the determination of radial velocity, whose shape and amplitude depend on stellar rotation velocity and transit geometry. This effect is known as the *Rossiter-McLaughlin effect* and it is observed in several planetary systems, such as HD 209458 (Queloz et al. 2000), WASP-4 (Sanchis-Ojeda et al. 2011), and HAT-P-11 (Sanchis-Ojeda & Winn 2011). Such distortions may be avoided if we consider the spectral region away from the prominent stellar lines (Quirrenbach 2006). Anyway, because of the presence of the transiting planet, the term $\delta\mathcal{F}_{\mathrm{direct}}$ may be decomposed in two contributions: $\delta\mathcal{F}_{\mathrm{solid}}$ and $\delta\mathcal{F}_{\mathrm{atm}}$. The first component refers to the fact that within a certain planetary radius, R_{p}, the planet seems to be totally opaque to radiations whatever (Cassen et al. 2006) (this occurs at the solid surface for a terrestrial planet, for a gaseous planet the opaque surface depends on wavelength, Tinetti et al. 2012). Assuming to have the radius R_{p}, the relative stellar flux density variation due to the opaque planet is given by the ratio of occulted stellar surface and the stellar surface itself

$$\frac{\delta\mathcal{F}_{\mathrm{solid}}}{\mathcal{F}_0} = \frac{\pi R_{\mathrm{p}}^2}{\pi R_\star^2},$$

---

[1] The geometric albedo, α, is the ratio of brightness at zero phase angle to that of a fully reflecting diffusively scattering flat disk (Lambertian sphere) with the same cross-section (Perryman 2011).

where $R_\star$ is the stellar radius. The $\delta F_{\rm atm}$ term refers to the starlight occultation due to the atmospheric absorption. During the primary transit a fraction of the stellar radiation goes through the annular region which indicates the planetary atmosphere (called also the *terminator* region of the atmosphere), whose profile we observe projected on the plane of the sky. The starlight is filtered by the atmosphere and this induces the presence of spectral features in transmission not observed in other orbital phases, which provide significant information about the chemical composition of the atmopshere (Tinetti et al. 2012). These spectral features are due to absorption and scattering from molecules and atoms filling the planetary atmosphere. At particular wavelengths, corresponding to strong atomic and molecular transitions, the atmosphere appears opaque to the radiation, the relative flux variation results higher and the effective profile of the planet larger (Winn 2010); this is illustrated in Fig. 1.18.

For wavelengths shorter than the planet's Planck-curve maximum (~2.5 μm) and avoiding the regions of prominent spectral lines in the stellar spectrum, $\delta F_{\rm atm}$ is the most relevant wavelength-dependent term able to modify the observed flux of the star/planet system (Brown 2001). In order to analyse this term, we need to describe how the atmospheric transmission spectra are originated by carrying out a model. The stellar radiation interacts with molecules and atoms in the atmosphere being attenuated and this may be expressed through the Beer-Bouguer-Lambert law (Tinetti et al. 2012)

$$I(\lambda, z) = I_0 \; e^{-\tau(\lambda,z)}, \tag{B.3}$$

where I_0 is the radiation intensity incident at the top of the planetary atmosphere, $I(\lambda, z)$ is the transmitted radiation from the atmosphere at a specified wavelength and height, z is the spatial coordinate above $R_{\rm p}$ assuming a plane-parallel geometry, and τ is the optical path. I am assuming that at the planetary atmosphere is totally opaque at some radius $R_{\rm p}$ for all λ. The optical path is defined as the sum of the optical thickness related to the different molecular species present in the atmopshere, i.e. $\tau(\lambda, z) = \sum_i \tau_{\rm i}(\lambda, z)$, where i is the type of the molecule. To estimate the radiation intensity outcoming from the atmosphere it is required to compute the optical path following one of the paths illustrated in Fig. B.2, at a particular altitude z, for the i-th molecular species and this is expressed as

$$\tau_{\rm i}(\lambda, z) = 2 \int_0^{l(z)} \alpha_{\rm i}(z^{'}) \; dl = 2 \int_0^{l(z)} \rho(z^{'}) \; \chi_i(z^{'}) \; \kappa_i(\lambda, T) \; dl,$$

where $l(z)$ is the half of the considered geometrical length, $\rho(z)$ is the molecular density, $\kappa_i(\lambda, T)$ is the absorption coefficient for the i-th molecule at wavelength λ and temperature T, and $\chi(z)$ is the mixing ratio of the i-th molecule at altitude z, defined as the relative abundance of one component with respect to the total

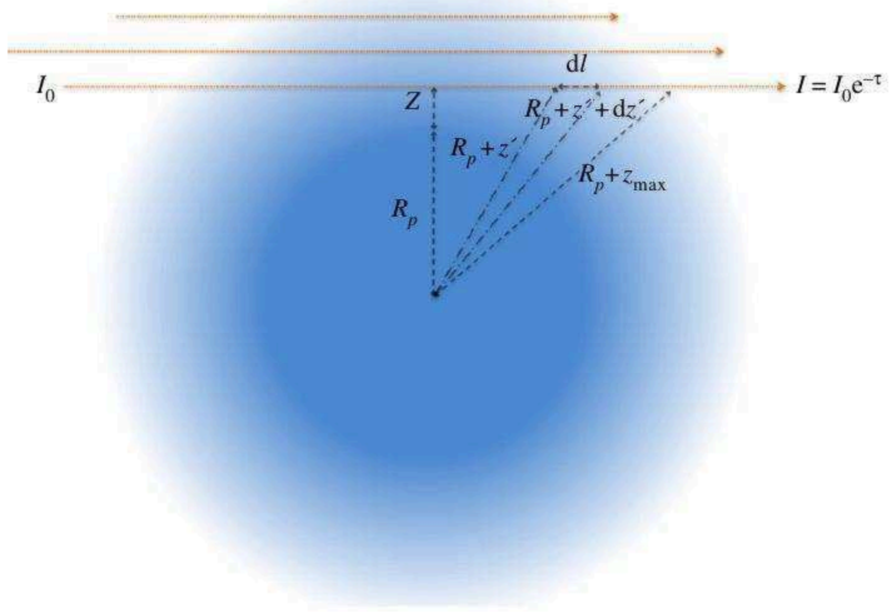

Figure B.2: Geometry of transit observation: the stellar photons are filtered through the planet atmosphere (Tinetti et al. 2012).

abundance ($\chi = n_\mathrm{i}/n_\mathrm{tot}$). From geometrical considerations, the path traversed by stellar photons is calculated as follows (Tinetti et al. 2012):

$$dl = \sqrt{(R_\mathrm{p} + z' + dz')^2 - (R_\mathrm{p} + z)^2} - \sqrt{(R_\mathrm{p} + z')^2 - (R_\mathrm{p} + z)^2}$$

$$l(z) = \int dl = \sqrt{(R_\mathrm{p} + z_\mathrm{max})^2 - (R_\mathrm{p} + z)^2}$$

Thus taking into account the transparency of the planetary atmosphere, the whole transit depth as a function of λ can be expressed as

$$\frac{\delta\mathcal{F}_\mathrm{direct}(\lambda)}{\mathcal{F}_0} = \frac{R_\mathrm{p}^2 + 2\int_0^{z_\mathrm{max}}(R_\mathrm{p} + z)(1 - e^{\tau(z,\lambda)})dz}{R_\star^2}.$$

From Eq. B.3 one can derive the effective area δA_eff which contributes to the occultation of the star and thus to the flux variation during the transit. If the atmosphere was able to block the radiation completely ($\tau = \infty$) we would have $\delta A_\mathrm{eff} = \pi(z_\mathrm{max}^2 - R_\mathrm{p}^2)$. Actually, if I_0 is the incident radiation intensity, a given fraction $I_0\ (1 - e^{-\tau(\lambda,z)})$ is able to traverse each of the infinitesimal annular regions $2\pi z\ dz$ forming the projected image of the atmosphere, thus we have

$$\delta A_\mathrm{eff}(\lambda) = \int_{R_\mathrm{p}}^{z_\mathrm{max}} 2\pi z\ (1 - e^{-\tau(\lambda,z)})\ dz.$$

where z_max is the highest altitude beyond which the atmosphere appears transparent, thus molecular and atomic extinctions result to be null, and may be arbitrarily chosen, for instance we could choose the altitude where the optical depth is much smaller than the unity. An alternative expression of the relative density flux variation due to planetary atmosphere is given by

$$\frac{\delta\mathcal{F}_{\mathrm{atm}}(\lambda)}{\mathcal{F}_0} = \frac{\delta A_{\mathrm{eff}}(\lambda)}{\pi R_\star^2}.$$

For what will follow it is useful to define a reference quantity which is given as the ratio of the annular region associated to the planet δA_{H}, related to the length scale of the atmosphere, H^2, and the stellar area $A_\star$:

$$\left(\frac{\delta A_{\mathrm{H}}}{A_\star}\right)_{\mathrm{atm}} = \frac{2\pi R_{\mathrm{p}} H}{\pi R_\star^2}. \tag{B.4}$$

As example, for an atmosphere of molecular hydrogen, with $g = 10^3$ cm/sec^2, $T = 1400$ K, $R_{\mathrm{p}} = 1.4\ R_{\mathrm{J}}$, and $R_\star = R_\odot$, we get $\delta A/A = 2.4{\cdot}10^{-4}$ (Quirrenbach 2006).

Under specified approximations it is possible to make a simple estimate of the flux density variations at two different wavelengths, assuming that most of the opacity sources are uniformly distributed in the atmosphere. We suppose that σ_1 and σ_2 indicate the opacity per gram of material at wavelengths λ_1 and λ_2, respectively, and that the densities of the species creating opacity decrease exponentially with height. The raylight 1 and 2 will achieve the same optical depth at different altitudes, $\tau_1(\lambda_1, z_1) = \tau_2(\lambda_2, z_2)$, where $z_1 > z_2$, and $\delta z = z_1 - z_2$. Thus these raylights are separated by

$$\frac{\delta z}{H} \approx ln\ \left[\frac{\sigma_1(z_1)}{\sigma_2(z_2)}\right].$$

The difference between the obscured flux measured at two wavelengths is given by the following expression (Brown 2001)

$$\left(\frac{\delta\mathcal{F}}{\mathcal{F}_0}\right)_{\lambda_1} - \left(\frac{\delta\mathcal{F}}{\mathcal{F}_0}\right)_{\lambda_2} \approx \frac{\delta z}{H}\left(\frac{\delta A_{\mathrm{H}}}{A_\star}\right)_{\mathrm{atm}} = \frac{2\pi R_{\mathrm{p}}\delta z}{R_\star^2},$$

$$\left(\frac{\delta\mathcal{F}}{\mathcal{F}_0}\right)_{\lambda_1} - \left(\frac{\delta\mathcal{F}}{\mathcal{F}_0}\right)_{\lambda_2} \approx \frac{\delta A_{\mathrm{H}}}{A_\star}\, ln \left[\frac{\sigma_1(z_1)}{\sigma_2(z_2)}\right].$$

In strong atomic and molecular absorption lines the ratio of line opacity to that of the adjacent continuum is about 10^4. This means that the altitude difference between the line optical depth along a raylight and the continuum optical depth along another raylight is about 10H and the observed line depth is about $2{\cdot}10^{-3}$ with respect to the total stellar flux.

---

[2] The quantity $H = \frac{kT(z)}{\mu g}$ is the length scale height and defines the atmospheric altitude where the pressure is reduced by a factor of the order of e, with k the Boltzmann constant, $T(z)$ the temperature at altitude z, μ the mean molecular mass, and g the planetary surface gravity.

Appendix C

Acronyms and abbreviations

ACS: Advanced Camera for Surveys
AU: Astronomical Unit

BaSeL: Basel Stellar Library

CEGP: Close-in Extra-solar Giant Planets

CFHT: Canada France Hawaii Telescope

CoRoT: COnvection, ROtation & planetary Transits

EChO: Exoplanet Characterization Observatory

ESA: European Space Agency

EUV: Extreme UltraViolet

EW: Equivalent Width

FINESSE: Fast Infrared Exoplanet Spectroscopy Survey Explorer

FOV: Field Of View

FUSE: Far Ultraviolet Spectroscopic Explorer

GJ: Gliese-Jahreiss

HARPS: High Accuracy Radial velocity Planet Searcher

HAT: Hungarian Automated Telescope network

HD: Henry Draper (catalogue)

HR: Hertzsprung–Russell diagram

HST: Hubble Space Telescope

JWST: James Webb Space Telescope

IAU: International Astronomical Union

IDL: Interactive Data Language

IUE: Internations Ultraviolet Explorer

IR: InfraRed

IRAC: InfraRed Array Camera

LASP: Laboratory for Atmospheric and Space Physics

LDC: Limb Darkening Coefficient

LTE: Local Thermodynamic Equilibrium

MDI: Michelson Doppler Imager

MIRI: Mid-InfraRed Instrument

NASA: National Aeronautics and Space Administration

NICMOS: Near Infrared Camera and Multi-Object Spectrometer

NIR: Near InfraRed

NIRCam: Near InfraRed Camera

NIRSpec: Near InfraRed Spectrograph

NOAA: National Oceanic and Atmospheric Administration

NSF: National Science Foundation

OGLE: Optical Gravitational Lensing Experiment

PPM: Parts Per Milion

PSPT: Precision Solar Photometric Telescope

RM: Rossiter-McLaughlin

SST: Spitzer Space Telescope

STIS: Space Telescope Imaging Spectrograph

TFI: Tunable Filter Imager

TrES: Transatlantic Exoplanet Survey

USAF: United State Air Force

UV: UltraViolet

WASP: Wide Angle Search for Planets

WIRCam: Wide-field InfraRed Camera

Bibliography

Agol, E., Cowan, N. B., Knutson, H. A., Deming, D., Steffen, J. H., Henry, G. W., & Charbonneau, D. 2010, ApJ, 721, 1861

Aigrain, S. & Irwin, M. 2004, MNRAS, 350, 331

Aigrain, S., Pont, F., Fressin, F., Alapini, A., Alonso, R., Auvergne, M., Barbieri, M., Barge, P., Bordé, P., Bouchy, F., Deeg, H., de La Reza, R., Deleuil, M., Dvorak, R., Erikson, A., Fridlund, M., Gondoin, P., Guterman, P., Jorda, L., Lammer, H., Léger, A., Llebaria, A., Magain, P., Mazeh, T., Moutou, C., Ollivier, M., Pätzold, M., Queloz, D., Rauer, H., Rouan, D., Schneider, J., Wuchter, G., & Zucker, S. 2009, A&A, 506, 425

Allard, F. & Hauschildt, P. H. 1995, ApJ, 445, 433

Alonso, R., Auvergne, M., Baglin, A., Ollivier, M., Moutou, C., Rouan, D., Deeg, H. J., Aigrain, S., Almenara, J. M., Barbieri, M., Barge, P., Benz, W., Bordé, P., Bouchy, F., de La Reza, R., Deleuil, M., Dvorak, R., Erikson, A., Fridlund, M., Gillon, M., Gondoin, P., Guillot, T., Hatzes, A., Hébrard, G., Kabath, P., Jorda, L., Lammer, H., Léger, A., Llebaria, A., Loeillet, B., Magain, P., Mayor, M., Mazeh, T., Pätzold, M., Pepe, F., Pont, F., Queloz, D., Rauer, H., Shporer, A., Schneider, J., Stecklum, B., Udry, S., & Wuchterl, G. 2008, A&A, 482, L21

Ayres, T. R., Fleming, T. A., Simon, T., Haisch, B. M., Brown, A., Lenz, D., Wamsteker, W., de Martino, D., Gonzalez, C., Bonnell, J., Mas-Hesse, J. M., Rosso, C., Schmitt, J. H. M. M., Truemper, J., Voges, W., Pye, J., Dempsey, R. C., Linsky, J. L., Guinan, E. F., Harper, G. M., Jordan, C., Montesinos, B. M., Pagano, I., & Rodono, M. 1995, ApJS, 96, 223

Babcock, H. W. 1961, ApJ, 133, 572

Baines, E. K., McAlister, H. A., ten Brummelaar, T. A., Turner, N. H., Sturmann, J., Sturmann, L., Goldfinger, P. J., & Ridgway, S. T. 2008, ApJ, 680, 728

Bakos, G. Á., Hartman, J., Torres, G., Latham, D. W., Kovács, G., Noyes, R. W., Fischer, D. A., Johnson, J. A., Marcy, G. W., Howard, A. W., Kipping, D., Esquerdo, G. A., Shporer, A., Béky, B., Buchhave, L. A., Perumpilly, G., Everett, M., Sasselov, D. D., Stefanik, R. P., Lázár, J., Papp, I., & Sári, P. 2011, ApJ, 742, 116

Bakos, G. Á., Knutson, H., Pont, F., Moutou, C., Charbonneau, D., Shporer, A., Bouchy, F., Everett, M., Hergenrother, C., Latham, D. W., Mayor, M., Mazeh, T., Noyes, R. W., Queloz, D., Pál, A., & Udry, S. 2006, ApJ, 650, 1160

Bakos, G. Á., Shporer, A., Pál, A., Torres, G., Kovács, G., Latham, D. W., Mazeh, T., Ofir, A., Noyes, R. W., Sasselov, D. D., Bouchy, F., Pont, F., Queloz, D., Udry, S., Esquerdo, G., Sipőcz, B., Kovács, G., Stefanik, R., Lázár, J., Papp, I., & Sári, P. 2007, ApJ, 671, L173

Baliunas, S., Sokoloff, D., & Soon, W. 1996, ApJ, 457, L99

Baliunas, S. L., Donahue, R. A., Soon, W. H., Horne, J. H., Frazer, J., Woodard-Eklund, L., Bradford, M., Rao, L. M., Wilson, O. C., Zhang, Q., Bennett, W., Briggs, J., Carroll, S. M., Duncan, D. K., Figueroa, D., Lanning, H. H., Misch, T., Mueller, J., Noyes, R. W., Poppe, D., Porter, A. C., Robinson, C. R., Russell, J., Shelton, J. C., Soyumer, T., Vaughan, A. H., & Whitney, J. H. 1995, ApJ, 438, 269

Ballerini, P., Micela, G., Lanza, A. F., & Pagano, I. 2012, A&A, 539, A140

Barman, T. 2007, ApJ, 661, L191

Bean, J. L., Benedict, G. F., Charbonneau, D., Homeier, D., Taylor, D. C., McArthur, B., Seifahrt, A., Dreizler, S., & Reiners, A. 2008, A&A, 486, 1039

Beaulieu, J. P., Carey, S., Ribas, I., & Tinetti, G. 2008, ApJ, 677, 1343

Beaulieu, J. P., Kipping, D. M., Batista, V., Tinetti, G., Ribas, I., Carey, S., Noriega-Crespo, J. A., Griffith, C. A., Campanella, G., Dong, S., Tennyson, J., Barber, R. J., Deroo, P., Fossey, S. J., Liang, D., Swain, M. R., Yung, Y., & Allard, N. 2010, MNRAS, 409, 963

Berdyugina, S. V. 2005, Living Reviews in Solar Physics, 2, 8

Berta, Z. K., Charbonneau, D., Bean, J., Irwin, J., Burke, C. J., Désert, J.-M., Nutzman, P., & Falco, E. E. 2011, ApJ, 736, 12

Bessell, M. S. 1990, PASP, 102, 1181

Bessell, M. S. & Brett, J. M. 1988, PASP, 100, 1134

Bessell, M. S., Brett, J. M., Scholz, M., & Wood, P. R. 1991, A&AS, 89, 335

Bessell, M. S., Brett, J. M., Wood, P. R., & Scholz, M. 1989, A&AS, 77, 1

Bonfils, X., Mayor, M., Delfosse, X., Forveille, T., Gillon, M., Perrier, C., Udry, S., Bouchy, F., Lovis, C., Pepe, F., Queloz, D., Santos, N. C., & Bertaux, J.-L. 2007, A&A, 474, 293

Bonomo, A. S., Aigrain, S., Bordé, P., & Lanza, A. F. 2009, A&A, 495, 647

Bonomo, A. S. & Lanza, A. F. 2008, A&A, 482, 341

Bouchy, F., Udry, S., Mayor, M., Moutou, C., Pont, F., Iribarne, N., da Silva, R., Ilovaisky, S., Queloz, D., Santos, N. C., Ségransan, D., & Zucker, S. 2005, A&A, 444, L15

Brandenburg, A. & Subramanian, K. 2005, Phys. Rep., 417, 1

Brown, T. M. 2001, ApJ, 553, 1006

—. 2003, ApJ, 593, L125

Brown, T. M. 2008, in Extrasolar Planets, ed. H. Deeg, J. A. Belmonte, & A. Aparicio, 65

Brown, T. M., Charbonneau, D., Gilliland, R. L., Noyes, R. W., & Burrows, A. 2001, ApJ, 552, 699

Brown, T. M., Libbrecht, K. G., & Charbonneau, D. 2002, PASP, 114, 826

Burrows, A., Hubeny, I., Budaj, J., Knutson, H. A., & Charbonneau, D. 2007, ApJ, 668, L171

Butler, R. P., Vogt, S. S., Marcy, G. W., Fischer, D. A., Wright, J. T., Henry, G. W., Laughlin, G., & Lissauer, J. J. 2004, ApJ, 617, 580

Caldwell, D. A., Kolodziejczak, J. J., Van Cleve, J. E., Jenkins, J. M., Gazis, P. R., Argabright, V. S., Bachtell, E. E., Dunham, E. W., Geary, J. C., Gilliland, R. L., Chandrasekaran, H., Li, J., Tenenbaum, P., Wu, H., Borucki, W. J., Bryson, S. T., Dotson, J. L., Haas, M. R., & Koch, D. G. 2010, ApJ, 713, L92

Cameron, A. C., Horne, K., Penny, A., & James, D. 1999, Nature, 402, 751

Carter, J. A., Winn, J. N., Holman, M. J., Fabrycky, D., Berta, Z. K., Burke, C. J., & Nutzman, P. 2011, ApJ, 730, 82

Carter, J. A., Yee, J. C., Eastman, J., Gaudi, B. S., & Winn, J. N. 2008, ApJ, 689, 499

Cassen, P., Guillot, T., & Quirrenbach, A. 2006, Extrasolar Planets: Saas Fee Advanced Course 31, 451

Catanzarite, J., Law, N., & Shao, M. 2008, in Society of Photo-Optical Instrumentation Engineers (SPIE) Conference Series, Vol. 7013, Society of Photo-Optical Instrumentation Engineers (SPIE) Conference Series

Chapman, G. A. & McGuire, T. E. 1977, ApJ, 217, 657

Charbonneau, D., Allen, L. E., Megeath, S. T., Torres, G., Alonso, R., Brown, T. M., Gilliland, R. L., Latham, D. W., Mandushev, G., O'Donovan, F. T., & Sozzetti, A. 2005, ApJ, 626, 523

Charbonneau, D., Berta, Z. K., Irwin, J., Burke, C. J., Nutzman, P., Buchhave, L. A., Lovis, C., Bonfils, X., Latham, D. W., Udry, S., Murray-Clay, R. A., Holman, M. J., Falco, E. E., Winn, J. N., Queloz, D., Pepe, F., Mayor, M., Delfosse, X., & Forveille, T. 2009, Nature, 462, 891

Charbonneau, D., Brown, T. M., Latham, D. W., & Mayor, M. 2000, ApJ, 529, L45

Charbonneau, D., Brown, T. M., Noyes, R. W., & Gilliland, R. L. 2002, ApJ, 568, 377

Charbonneau, D., Noyes, R. W., Korzennik, S. G., Nisenson, P., Jha, S., Vogt, S. S., & Kibrick, R. I. 1999, ApJ, 522, L145

Charbonneau, P. 2010, Living Reviews in Solar Physics, 7, 3

Charbonneau, P., Schrijver, C. J., & MacGregor, K. B. 1997, in Cosmic Winds and the Heliosphere, ed. J. R. Jokipii, C. P. Sonett, & M. S. Giampapa, 677

Choudhuri, A. R. 2007, in American Institute of Physics Conference Series, Vol. 919, Kodai School on Solar Physics, ed. S. S. Hasan & D. Banerjee, 49–73

Christensen-Dalsgaard, J., Gough, D. O., & Thompson, M. J. 1991, ApJ, 378, 413

Claret, A. 2000, A&A, 363, 1081

—. 2004, A&A, 428, 1001

Claret, A. & Bloemen, S. 2011, A&A, 529, A75

Claret, A., Diaz-Cordoves, J., & Gimenez, A. 1995, A&AS, 114, 247

Cox, A. N. 2000, Allen's astrophysical quantities

Croll, B., Albert, L., Jayawardhana, R., Miller-Ricci Kempton, E., Fortney, J. J., Murray, N., & Neilson, H. 2011, ApJ, 736, 78

Czesla, S., Huber, K. F., Wolter, U., Schröter, S., & Schmitt, J. H. M. M. 2009, A&A, 505, 1277

Deming, D. 2009, in IAU Symposium, Vol. 253, IAU Symposium, 197–207

Deming, D., Agol, E., Ford, E., Fortney, J., Greene, T., Holman, M., Knutson, H., Latham, D., Laughlin, G., Sasselov, D., Seager, S., Street, R., & Showman, A. 2009, in Astronomy, Vol. 2010, astro2010: The Astronomy and Astrophysics Decadal Survey, 63–+

Deming, D., Brown, T. M., Charbonneau, D., Harrington, J., & Richardson, L. J. 2005, ApJ, 622, 1149

Deming, D., Harrington, J., Laughlin, G., Seager, S., Navarro, S. B., Bowman, W. C., & Horning, K. 2007, ApJ, 667, L199

Deming, D., Harrington, J., Seager, S., & Richardson, L. J. 2006, ApJ, 644, 560

Demory, B., Gillon, M., Barman, T., Bonfils, X., Mayor, M., Mazeh, T., Queloz, D., Udry, S., Bouchy, F., Delfosse, X., Forveille, T., Mallmann, F., Pepe, F., & Perrier, C. 2007, A&A, 475, 1125

Désert, J., Lecavelier des Etangs, A., Hébrard, G., Sing, D. K., Ehrenreich, D., Ferlet, R., & Vidal-Madjar, A. 2009, ApJ, 699, 478

Désert, J., Sing, D., Vidal-Madjar, A., Hébrard, G., Ehrenreich, D., Lecavelier Des Etangs, A., Parmentier, V., Ferlet, R., & Henry, G. W. 2011a, A&A, 526, A12+

Désert, J.-M., Bean, J., Miller-Ricci Kempton, E., Berta, Z. K., Charbonneau, D., Irwin, J., Fortney, J., Burke, C. J., & Nutzman, P. 2011b, ApJ, 731, L40+

Diaz-Cordoves, J., Claret, A., & Gimenez, A. 1995, A&AS, 110, 329

Diaz-Cordoves, J. & Gimenez, A. 1992, A&A, 259, 227

Doyle, L. R. 2008, in Extrasolar Planets, ed. H. Deeg, J. A. Belmonte, & A. Aparicio, 1

Dumusque, X., Santos, N. C., Udry, S., Lovis, C., & Bonfils, X. 2011, A&A, 527, A82

Eason, E. L. E., Giampapa, M. S., Radick, R. R., Worden, S. P., & Hege, E. K. 1992, AJ, 104, 1161

Eggenberger, A. & Udry, S. 2010, in EAS Publications Series, Vol. 41, EAS Publications Series, ed. T. Montmerle, D. Ehrenreich, & A.-M. Lagrange, 27–75

Ehrenreich, D., Hébrard, G., Lecavelier des Etangs, A., Sing, D. K., Désert, J., Bouchy, F., Ferlet, R., & Vidal-Madjar, A. 2007, ApJ, 668, L179

Eriksson, U. & Lindegren, L. 2007, A&A, 476, 1389

Finn, L. S. 1992, Phys. Rev. D, 46, 5236

Fluks, M. A., Plez, B., The, P. S., de Winter, D., Westerlund, B. E., & Steenman, H. C. 1994, A&AS, 105, 311

Foukal, P. 1990, Solar astrophysics

Foukal, P., Fröhlich, C., Spruit, H., & Wigley, T. M. L. 2006, Nature, 443, 161

Fressin, F., Torres, G., Desert, J.-M., Charbonneau, D., Batalha, N. M., Fortney, J. J., Rowe, J. F., Allen, C., Borucki, W. J., Brown, T. M., Bryson, S. T., Ciardi, D. R., Cochran, W. D., Deming, D., Dunham, E. W., Fabrycky, D. C., Gautier, III, T. N., Gilliland, R. L., Henze, C. E., Holman, M. J., Howell, S. B., Jenkins, J. M., Kinemuchi, K., Knutson, H., Koch, D. G., Latham, D. W., Lissauer, J. J., Marcy, G. W., Ragozzine, D., Sasselov, D. D., Still, M., Tenenbaum, P., & Uddin, K. 2011, ArXiv e-prints

Fröhlich, C. & Lean, J. 2004, A&A Rev., 12, 273

García, R. A., Turck-Chièze, S., Jiménez-Reyes, S. J., Ballot, J., Pallé, P. L., Eff-Darwich, A., Mathur, S., & Provost, J. 2007, Science, 316, 1591

Gardner, J. P., Mather, J. C., Clampin, M., Doyon, R., Greenhouse, M. A., Hammel, H. B., Hutchings, J. B., Jakobsen, P., Lilly, S. J., Long, K. S., Lunine, J. I., McCaughrean, M. J., Mountain, M., Nella, J., Rieke, G. H., Rieke, M. J., Rix, H., Smith, E. P., Sonneborn, G., Stiavelli, M., Stockman, H. S., Windhorst, R. A., & Wright, G. S. 2006, Space Sci. Rev., 123, 485

Gibson, N. P., Pont, F., & Aigrain, S. 2011, MNRAS, 411, 2199

Gillon, M., Bonfils, X., Demory, B.-O., Seager, S., Deming, D., & Triaud, A. H. M. J. 2011, A&A, 525, A32+

Gillon, M., Hatzes, A., Csizmadia, S., Fridlund, M., Deleuil, M., Aigrain, S., Alonso, R., Auvergne, M., Baglin, A., Barge, P., Barnes, S. I., Bonomo, A. S., Bordé, P., Bouchy, F., Bruntt, H., Cabrera, J., Carone, L., Carpano, S., Cochran, W. D., Deeg, H. J., Dvorak, R., Endl, M., Erikson, A., Ferraz-Mello, S., Gandolfi, D., Gazzano, J. C., Guenther, E., Guillot, T., Havel, M., Hébrard, G., Jorda, L., Léger, A., Llebaria, A., Lammer, H., Lovis, C., Mayor, M., Mazeh, T., Montalbán, J., Moutou, C., Ofir, A., Ollivier, M., Pätzold, M., Pepe, F., Queloz, D., Rauer, H., Rouan, D., Samuel, B., Santerne, A., Schneider, J., Tingley, B., Udry, S., Weingrill, J., & Wuchterl, G. 2010, A&A, 520, A97+

Giménez, A. 2006, A&A, 450, 1231

Golub, L. & Pasachoff, J. M. 1997, The Solar Corona

Gray, D. F. 2005, The Observation and Analysis of Stellar Photospheres

Güdel, M. 2007, Living Reviews in Solar Physics, 4, 3

Guillot, T. & Havel, M. 2011, A&A, 527, A20+

Hatzes, A. P. 2002, Astronomische Nachrichten, 323, 392

Hatzes, A. P. 2003, in Astronomical Society of the Pacific Conference Series, Vol. 294, Scientific Frontiers in Research on Extrasolar Planets, ed. D. Deming & S. Seager, 523–528

Hébrard, G., Désert, J.-M., Díaz, R. F., Boisse, I., Bouchy, F., Lecavelier Des Etangs, A., Moutou, C., Ehrenreich, D., Arnold, L., Bonfils, X., Delfosse, X., Desort, M., Eggenberger, A., Forveille, T., Gregorio, J., Lagrange, A.-M., Lovis, C., Pepe, F., Perrier, C., Pont, F., Queloz, D., Santerne, A., Santos, N. C., Ségransan, D., Sing, D. K., Udry, S., & Vidal-Madjar, A. 2010, A&A, 516, A95+

Henry, G. W., Marcy, G. W., Butler, R. P., & Vogt, S. S. 2000, ApJ, 529, L41

Henry, T. J., Soderblom, D. R., Donahue, R. A., & Baliunas, S. L. 1996, AJ, 111, 439

Howarth, I. D. 2011, ArXiv e-prints

Hubbard, W. B., Fortney, J. J., Lunine, J. I., Burrows, A., Sudarsky, D., & Pinto, P. 2001, ApJ, 560, 413

Huber, K. F., Czesla, S., Wolter, U., & Schmitt, J. H. M. M. 2010, A&A, 514, A39+

Irwin, P. G. J. 2008, Detection Methods and Properties of Known Exoplanets, ed. J. Mason, 1–20

Jha, S., Charbonneau, D., Garnavich, P. M., Sullivan, D. J., Sullivan, T., Brown, T. M., & Tonry, J. L. 2000, ApJ, 540, L45

Karttunen, H., Kroeger, P., Oja, H., Poutanen, M., & Donner, K. J. 2003, Fundamental astronomy

Keller, C. U., Schüssler, M., Vögler, A., & Zakharov, V. 2004, ApJ, 607, L59

Kirkpatrick, J. D., Kelly, D. M., Rieke, G. H., Liebert, J., Allard, F., & Wehrse, R. 1993, ApJ, 402, 643

Klinglesmith, D. A. & Sobieski, S. 1970, AJ, 75, 175

Knutson, H. A., Charbonneau, D., Allen, L. E., Burrows, A., & Megeath, S. T. 2008, ApJ, 673, 526

Knutson, H. A., Charbonneau, D., Allen, L. E., Fortney, J. J., Agol, E., Cowan, N. B., Showman, A. P., Cooper, C. S., & Megeath, S. T. 2007a, Nature, 447, 183

Knutson, H. A., Charbonneau, D., Noyes, R. W., Brown, T. M., & Gilliland, R. L. 2007b, ApJ, 655, 564

Kopal, Z. 1950, Harvard College Observatory Circular, 454, 1

Krivova, N. A., Solanki, S. K., & Floyd, L. 2006, A&A, 452, 631

Kurucz, R. 1995, CD-ROM, private communication

Lagrange, A.-M., Desort, M., & Meunier, N. 2010, A&A, 512, A38

Lanza, A. F., Bonomo, A. S., Moutou, C., Pagano, I., Messina, S., Leto, G., Cutispoto, G., Aigrain, S., Alonso, R., Barge, P., Deleuil, M., Auvergne, M., Baglin, A., & Collier Cameron, A. 2010, A&A, 520, A53+

Lanza, A. F., Bonomo, A. S., & Rodonò, M. 2007, A&A, 464, 741

Lanza, A. F., De Martino, C., & Rodonò, M. 2008, New Astronomy, 13, 77

Lanza, A. F., Messina, S., Pagano, I., & Rodonò, M. 2006, Astronomische Nachrichten, 327, 21

Lanza, A. F., Pagano, I., Leto, G., Messina, S., Aigrain, S., Alonso, R., Auvergne, M., Baglin, A., Barge, P., Bonomo, A. S., Boumier, P., Collier Cameron, A., Comparato, M., Cutispoto, G., de Medeiros, J. R., Foing, B., Kaiser, A., Moutou, C., Parihar, P. S., Silva-Valio, A., & Weiss, W. W. 2009, A&A, 493, 193

Lanza, A. F., Rodonò, M., & Pagano, I. 2004, A&A, 425, 707

Lanza, A. F., Rodonò, M., Pagano, I., Barge, P., & Llebaria, A. 2003, A&A, 403, 1135

Leger, A., Mariotti, J. M., Mennesson, B., Ollivier, M., Puget, J. L., Rouan, D., & Schneider, J. 1996, Icarus, 123, 249

Léger, A., Rouan, D., Schneider, J., Barge, P., Fridlund, M., Samuel, B., Ollivier, M., Guenther, E., Deleuil, M., Deeg, H. J., Auvergne, M., Alonso, R., Aigrain, S., Alapini, A., Almenara, J. M., Baglin, A., Barbieri, M., Bruntt, H., Bordé, P., Bouchy, F., Cabrera, J., Catala, C., Carone, L., Carpano, S., Csizmadia, S., Dvorak, R., Erikson, A., Ferraz-Mello, S., Foing, B., Fressin, F., Gandolfi, D., Gillon, M., Gondoin, P., Grasset, O., Guillot, T., Hatzes, A., Hébrard, G., Jorda, L., Lammer, H., Llebaria, A., Loeillet, B., Mayor, M., Mazeh, T., Moutou, C., Pätzold, M., Pont, F., Queloz, D., Rauer, H., Renner, S., Samadi, R., Shporer, A., Sotin, C., Tingley, B., Wuchterl, G., Adda, M., Agogu, P., Appourchaux, T., Ballans, H., Baron, P., Beaufort, T., Bellenger, R., Berlin, R., Bernardi, P., Blouin, D., Baudin, F., Bodin, P., Boisnard, L., Boit, L., Bonneau, F., Borzeix, S., Briet, R., Buey, J., Butler, B., Cailleau, D., Cautain, R., Chabaud, P., Chaintreuil, S., Chiavassa, F., Costes, V., Cuna Parrho, V., de Oliveira Fialho, F., Decaudin, M., Defise, J., Djalal, S., Epstein, G., Exil, G., Fauré, C., Fenouillet, T., Gaboriaud, A., Gallic, A., Gamet, P., Gavalda, P., Grolleau, E., Gruneisen, R., Gueguen, L., Guis, V., Guivarc'h, V., Guterman, P., Hallouard, D., Hasiba, J., Heuripeau, F., Huntzinger, G., Hustaix, H., Imad, C., Imbert, C., Johlander, B., Jouret, M., Journoud, P., Karioty, F., Kerjean, L., Lafaille, V., Lafond, L., Lam-Trong, T., Landiech, P., Lapeyrere, V., Larqué, T., Laudet, P., Lautier, N., Lecann, H., Lefevre, L., Leruyet, B., Levacher, P., Magnan, A., Mazy, E., Mertens, F., Mesnager, J., Meunier, J., Michel, J., Monjoin, W., Naudet, D., Nguyen-Kim, K., Orcesi, J., Ottacher, H., Perez, R., Peter, G., Plasson, P., Plesseria, J., Pontet, B., Pradines, A., Quentin, C., Reynaud, J., Rolland, G., Rollenhagen, F., Romagnan, R., Russ, N., Schmidt, R., Schwartz, N., Sebbag, I., Sedes, G., Smit, H., Steller, M. B., Sunter, W., Surace, C., Tello, M., Tiphène, D., Toulouse, P., Ulmer, B., Vandermarcq, O., Vergnault, E., Vuillemin, A., & Zanatta, P. 2009, A&A, 506, 287

Lejeune, T., Cuisinier, F., & Buser, R. 1997, A&AS, 125, 229

—. 1998, A&AS, 130, 65

Lépine, S. & Gaidos, E. 2011, AJ, 142, 138

Lockwood, G. W., Skiff, B. A., Henry, G. W., Henry, S., Radick, R. R., Baliunas, S. L., Donahue, R. A., & Soon, W. 2007, ApJS, 171, 260

Machalek, P., McCullough, P. R., Burke, C. J., Valenti, J. A., Burrows, A., & Hora, J. L. 2008, ApJ, 684, 1427

Makarov, V. V., Parker, D., & Ulrich, R. K. 2010, ApJ, 717, 1202

Mandel, K. & Agol, E. 2002, ApJ, 580, L171

Marino, G., Rodonó, M., Leto, G., & Cutispoto, G. 1999, A&A, 352, 189

Mason, J. W. 2008, Exoplanets (Exoplanets, Springer Praxis Books. ISBN 978-3-540-74007-0. Praxis Publishing Ltd, Chichester, UK, 2008)

Mayor, M. & Queloz, D. 1995, Nature, 378, 355

Mazeh, T., Guterman, P., Aigrain, S., Zucker, S., Grinberg, N., Alapini, A., Alonso, R., Auvergne, M., Barbieri, M., Barge, P., Bordé, P., Bouchy, F., Deeg, H., de La Reza, R., Deleuil, M., Dvorak, R., Erikson, A., Fridlund, M., Gondoin, P., Jorda, L., Lammer, H., Léger, A., Llebaria, A., Magain, P., Moutou, C., Ollivier, M., Pätzold, M., Pont, F., Queloz, D., Rauer, H., Rouan, D., Sabo, R., Schneider, J., & Wuchterl, G. 2009, A&A, 506, 431

Mazeh, T., Naef, D., Torres, G., Latham, D. W., Mayor, M., Beuzit, J.-L., Brown, T. M., Buchhave, L., Burnet, M., Carney, B. W., Charbonneau, D., Drukier, G. A., Laird, J. B., Pepe, F., Perrier, C., Queloz, D., Santos, N. C., Sivan, J.-P., Udry, S., & Zucker, S. 2000, ApJ, 532, L55

Mehltretter, J. P. 1974, Sol. Phys., 38, 43

Melikian, N. D., Tamazian, V. S., & Samsonyan, A. L. 2011, Astrophysics, 54, 469

Meunier, N., Desort, M., & Lagrange, A.-M. 2010, A&A, 512, A39

Middelkoop, F. 1982, A&A, 113, 1

Miller-Ricci, E. & Fortney, J. J. 2010, ApJ, 716, L74

Montes, D., López-Santiago, J., Gálvez, M. C., Fernández-Figueroa, M. J., De Castro, E., & Cornide, M. 2001, MNRAS, 328, 45

Morales-Calderón, M., Stauffer, J. R., Kirkpatrick, J. D., Carey, S., Gelino, C. R., Barrado y Navascués, D., Rebull, L., Lowrance, P., Marley, M. S., Charbonneau, D., Patten, B. M., Megeath, S. T., & Buzasi, D. 2006, ApJ, 653, 1454

Moutou, C. & COROT/Exoplanet Team. 2003, in Astronomical Society of the Pacific Conference Series, Vol. 294, Scientific Frontiers in Research on Extrasolar Planets, ed. D. Deming & S. Seager, 423–426

Moutou, C., Pont, F., Barge, P., Aigrain, S., Auvergne, M., Blouin, D., Cautain, R., Erikson, A. R., Guis, V., Guterman, P., Irwin, M., Lanza, A. F., Queloz, D., Rauer, H., Voss, H., & Zucker, S. 2005, A&A, 437, 355

Muller, R. & Keil, S. L. 1983, Sol. Phys., 87, 243

Nordlund, Å., Stein, R. F., & Asplund, M. 2009, Living Reviews in Solar Physics, 6, 2

Noyes, R. W. 1982, The sun, our star (Cambridge, MA, Harvard University Press)

Noyes, R. W., Hartmann, L. W., Baliunas, S. L., Duncan, D. K., & Vaughan, A. H. 1984, ApJ, 279, 763

Nutzman, P. & Charbonneau, D. 2008, PASP, 120, 317

Ollivier, M., Roques, F., Casoli, F., Encrenaz, T., & Selsis, F. 2009, Planetary Systems (Springer Berlin Heidelberg)

Pál, A. 2008, MNRAS, 390, 281

Pallé, E., Zapatero Osorio, M. R., & García Muñoz, A. 2011, ApJ, 728, 19

Percy, J. R. 1978, JRASC, 72, 162

Perryman, M. 2011, The Exoplanet Handbook (Cambridge University Press)

Perryman, M. A. C. 2000, Reports on Progress in Physics, 63, 1209

Petrov, P. P. 2003, Astrophysics, 46, 506

Pierce, A. K. & Slaughter, C. D. 1977, Sol. Phys., 51, 25

Pizzolato, N., Maggio, A., Micela, G., Sciortino, S., & Ventura, P. 2003, A&A, 397, 147

Pont, F., Gilliland, R. L., Moutou, C., Charbonneau, D., Bouchy, F., Brown, T. M., Mayor, M., Queloz, D., Santos, N., & Udry, S. 2007, A&A, 476, 1347

Pont, F., Knutson, H., Gilliland, R. L., Moutou, C., & Charbonneau, D. 2008, MNRAS, 385, 109

Press, W. H., Teukolsky, S. A., Vetterling, W. T., & Flannery, B. P. 1992, Numerical recipes in FORTRAN. The art of scientific computing (Cambridge: University Press)

Queloz, D., Bouchy, F., Moutou, C., Hatzes, A., Hébrard, G., Alonso, R., Auvergne, M., Baglin, A., Barbieri, M., Barge, P., Benz, W., Bordé, P., Deeg, H. J., Deleuil, M., Dvorak, R., Erikson, A., Ferraz Mello, S., Fridlund, M., Gandolfi, D., Gillon, M., Guenther, E., Guillot, T., Jorda, L., Hartmann, M., Lammer, H., Léger, A., Llebaria, A., Lovis, C., Magain, P., Mayor, M., Mazeh, T., Ollivier, M., Pätzold, M., Pepe, F., Rauer, H., Rouan, D., Schneider, J., Segransan, D., Udry, S., & Wuchterl, G. 2009, A&A, 506, 303

Queloz, D., Eggenberger, A., Mayor, M., Perrier, C., Beuzit, J. L., Naef, D., Sivan, J. P., & Udry, S. 2000, A&A, 359, L13

Queloz, D., Henry, G. W., Sivan, J. P., Baliunas, S. L., Beuzit, J. L., Donahue, R. A., Mayor, M., Naef, D., Perrier, C., & Udry, S. 2001, A&A, 379, 279

Quirrenbach, A. 2006, in Saas-Fee Advanced Course 31: Extrasolar planets, ed. D. Queloz, S. Udry, M. Mayor, W. Benz, P. Cassen, T. Guillot, & A. Quirrenbach, 1–242

Reach, W. T., Megeath, S. T., Cohen, M., Hora, J., Carey, S., Surace, J., Willner, S. P., Barmby, P., Wilson, G., Glaccum, W., Lowrance, P., Marengo, M., & Fazio, G. G. 2005, PASP, 117, 978

Richardson, L. J., Deming, D., & Seager, S. 2003a, ApJ, 597, 581

Richardson, L. J., Deming, D., Wiedemann, G., Goukenleuque, C., Steyert, D., Harrington, J., & Esposito, L. W. 2003b, ApJ, 584, 1053

Richardson, L. J., Harrington, J., Seager, S., & Deming, D. 2006, ApJ, 649, 1043

Rosner, R. & Weiss, N. O. 1992, in Astronomical Society of the Pacific Conference Series, Vol. 27, The Solar Cycle, ed. K. L. Harvey, 511

Saar, S. H. & Donahue, R. A. 1997, ApJ, 485, 319

Sada, P. V., Deming, D., Jackson, B., Jennings, D. E., Peterson, S. W., Haase, F., Bays, K., O'Gorman, E., & Lundsford, A. 2010, ApJ, 720, L215

Sanchis-Ojeda, R. & Winn, J. N. 2011, ArXiv e-prints

Sanchis-Ojeda, R., Winn, J. N., Holman, M. J., Carter, J. A., Osip, D. J., & Fuentes, C. I. 2011, ApJ, 733, 127

Schrijver, C. J. & Zwaan, C. 2000, Solar and Stellar Magnetic Activity (Cambridge University Press)

Seager, S. & Deming, D. 2010, ARA&A, 48, 631

Seager, S. & Mallén-Ornelas, G. 2003, ApJ, 585, 1038

Seager, S. & Sasselov, D. D. 2000, ApJ, 537, 916

Silva, A. V. R. 2003, ApJ, 585, L147

Silva-Valio, A. 2008, ApJ, 683, L179

Silva-Valio, A., Lanza, A. F., Alonso, R., & Barge, P. 2010, A&A, 510, A25+

Simon, T., Ayres, T. R., Redfield, S., & Linsky, J. L. 2002, ApJ, 579, 800

Sing, D. K. 2010, A&A, 510, A21+

Sing, D. K., Désert, J.-M., Fortney, J. J., Lecavelier Des Etangs, A., Ballester, G. E., Cepa, J., Ehrenreich, D., López-Morales, M., Pont, F., Shabram, M., & Vidal-Madjar, A. 2011a, A&A, 527, A73+

Sing, D. K., Désert, J.-M., Lecavelier Des Etangs, A., Ballester, G. E., Vidal-Madjar, A., Parmentier, V., Hebrard, G., & Henry, G. W. 2009, A&A, 505, 891

Sing, D. K., Pont, F., Aigrain, S., Charbonneau, D., Désert, J.-M., Gibson, N., Gilliland, R., Hayek, W., Henry, G., Knutson, H., Lecavelier Des Etangs, A., Mazeh, T., & Shporer, A. 2011b, MNRAS, 416, 1443

Skumanich, A. 1972, ApJ, 171, 565

Sobolev, V. V. 1975, Light scattering in planetary atmospheres, 6213

Solanki, S. K. & Unruh, Y. C. 1998, A&A, 329, 747

Sozzetti, A., Torres, G., Charbonneau, D., Latham, D. W., Holman, M. J., Winn, J. N., Laird, J. B., & O'Donovan, F. T. 2007, ApJ, 664, 1190

Spruit, H. C. 1976, Sol. Phys., 50, 269

Steiner, O., Bruls, J., & Hauschildt, P. H. 2001, in Astronomical Society of the Pacific Conference Series, Vol. 236, Advanced Solar Polarimetry – Theory, Observation, and Instrumentation, ed. M. Sigwarth, 453

Stix, M. 1989, The Sun. an Introduction (Springer-Verlag Berlin Heidelberg New York)

—. 2002, The sun: an introduction (Springer)

Swain, M. 2012a, in EGU General Assembly Conference Abstracts, Vol. 14, EGU General Assembly Conference Abstracts, ed. A. Abbasi & N. Giesen, 13409

Swain, M. R. 2012b, in American Astronomical Society Meeting Abstracts, Vol. 220, American Astronomical Society Meeting Abstracts, 505.05

Swain, M. R., Vasisht, G., & Tinetti, G. 2008, Nature, 452, 329

Tarter, J. C., Backus, P. R., Mancinelli, R. L., Aurnou, J. M., Backman, D. E., Basri, G. S., Boss, A. P., Clarke, A., Deming, D., Doyle, L. R., Feigelson, E. D., Freund, F., Grinspoon, D. H., Haberle, R. M., Hauck, II, S. A., Heath, M. J., Henry, T. J., Hollingsworth, J. L., Joshi, M. M., Kilston, S., Liu, M. C., Meikle, E., Reid, I. N., Rothschild, L. J., Scalo, J., Segura, A., Tang, C. M., Tiedje, J. M., Turnbull, M. C., Walkowicz, L. M., Weber, A. L., & Young, R. E. 2007, Astrobiology, 7, 30

Tayler, R. J. 1997, The Sun as a star (Cambridge University Press)

Tessenyi, M. 2010, in AAS/Division for Planetary Sciences Meeting Abstracts, Vol. 42, AAS/Division for Planetary Sciences Meeting Abstracts #42, #27.33–+

Thompson, M. J. 2004, Astronomy and Geophysics, 45, 040000

Tinetti, G., Beaulieu, J. P., Henning, T., Meyer, M., Micela, G., Ribas, I., Stam, D., Swain, M., Krause, O., Ollivier, M., Pace, E., Swinyard, B., Aylward, A., van Boekel, R., Coradini, A., Encrenaz, T., Snellen, I., Zapatero-Osorio, M. R., Bouwman, J., Y-K. Cho, J., Coudé du Foresto, V., Guillot, T., Lopez-Morales, M., Mueller-Wodarg, I., Palle, E., Selsis, F., Sozzetti, A., Ade, P. A. R., Achilleos, N., Adriani, A., Agnor, C. B., Afonso, C., Allende Prieto, C., Bakos, G., Barber, R. J., Barlow, M., Bernath, P., Bezard, B., Bordé, P., Brown, L. R., Cassan, A., Cavarroc, C., Ciaravella, A., Cockell, C. O. U., Coustenis, A., Danielski, C., Decin, L., De Kok, R., Demangeon, O., Deroo, P., Doel, P., Drossart, P., Fletcher, L. N., Focardi, M., Forget, F., Fossey, S., Fouqué, P., Frith, J., Galand, M., Gaulme, P., González Hernández, J. I., Grasset, O., Grassi, D., Grenfell, J. L., Griffin, M. J., Griffith, C. A., Grözinger, U., Guedel, M., Guio, P., Hainaut, O., Hargreaves, R., Hauschildt, P. H., Heng, K., Heyrovsky, D., Hueso, R., Irwin, P., Kaltenegger, L., Kervella, P., Kipping, D., Koskinen, T. T., Kovács, G., La Barbera, A., Lammer, H., Lellouch, E., Leto, G., Lopez Morales, M., Lopez Valverde, M. A., Lopez-Puertas, M., Lovis, C., Maggio, A., Maillard, J. P., Maldonado Prado, J., Marquette, J. B., Martin-Torres, F. J., Maxted, P., Miller, S., Molinari, S., Montes, D., Moro-Martin, A., Moses, J. I., Mousis, O., Nguyen Tuong, N., Nelson, R., Orton, G. S., Pantin, E., Pascale, E., Pezzuto, S., Pinfield, D., Poretti, E., Prinja, R., Prisinzano, L., Rees, J. M., Reiners, A., Samuel, B., Sanchez-Lavega, A., Sanz Forcada, J., Sasselov, D., Savini, G., Sicardy, B., Smith, A., Stixrude, L., Strazzulla, G., Tennyson, J., Tessenyi, M., Vasisht, G., Vinatier, S., Viti, S., Waldmann, I., White, G. J., Widemann, T., Wordsworth, R., Yelle, R., Yung, Y., & Yurchenko, S. N. 2011, ArXiv e-prints

Tinetti, G., Liang, M., Vidal-Madjar, A., Ehrenreich, D., Lecavelier des Etangs, A., & Yung, Y. L. 2007a, ApJ, 654, L99

Tinetti, G., Tennyson, J., Griffith, C., & Waldmann, I. 2012, Philosophical Transaction of the Royal Society, 370, 2749

Tinetti, G., Vidal-Madjar, A., Liang, M., Beaulieu, J., Yung, Y., Carey, S., Barber, R. J., Tennyson, J., Ribas, I., Allard, N., Ballester, G. E., Sing, D. K., & Selsis, F. 2007b, Nature, 448, 169

Tobias, S. M. 2002, Royal Society of London Philosophical Transactions Series A, 360, 2741

Tofflemire, B. M., Wisniewski, J. P., Kowalski, A. F., Schmidt, S. J., Kundurthy, P., Hilton, E. J., Holtzman, J. A., & Hawley, S. L. 2011, ArXiv e-prints

Torres, G. 2007, ApJ, 671, L65

Turner, J. D., Smart, B. M., Hardegree-Ullman, K. K., Carleton, T. M., Walker-LaFollette, A. M., Crawford, B. E., Smith, C.-T. W., McGraw, A. M., Small, L. C., Rocchetto, M., Cunningham, K. I., Towner, A. P. M., Zellem, R., Robertson, A. N., Guvenen, B. C., Schwarz, K. R., Hardegree-Ullman, E. E., Collura, D., Henz, T. N., Lejoly, C., Richardson, L. L., Weinand, M. A., Taylor, J. M., Daugherty, M. J., Wilson, A. A., & Austin, C. L. 2012, MNRAS, 48

Udalski, A. 2003, Acta Astronomica, 53, 291

Udalski, A., Paczynski, B., Zebrun, K., Szymanski, M., Kubiak, M., Soszynski, I., Szewczyk, O., Wyrzykowski, L., & Pietrzynski, G. 2002a, Acta Astronomica, 52, 1

Udalski, A., Szewczyk, O., Zebrun, K., Pietrzynski, G., Szymanski, M., Kubiak, M., Soszynski, I., & Wyrzykowski, L. 2002b, Acta Astronomica, 52, 317

Udalski, A., Zebrun, K., Szymanski, M., Kubiak, M., Soszynski, I., Szewczyk, O., Wyrzykowski, L., & Pietrzynski, G. 2002c, Acta Astronomica, 52, 115

van't Veer, F. 1960, L'assombrissement centre-bord des etoiles. (Drukkerij Schotanus)

Vidal-Madjar, A., Désert, J.-M., Lecavelier des Etangs, A., Hébrard, G., Ballester, G. E., Ehrenreich, D., Ferlet, R., McConnell, J. C., Mayor, M., & Parkinson, C. D. 2004, ApJ, 604, L69

Vidal-Madjar, A., Lecavelier des Etangs, A., Désert, J.-M., Ballester, G. E., Ferlet, R., Hébrard, G., & Mayor, M. 2003, Nature, 422, 143

Vogt, S. S. 1975, ApJ, 199, 418

Warner, B. 1966, The Observatory, 86, 82

—. 1968, The Observatory, 88, 217

Westera, P., Lejeune, T., Buser, R., Cuisinier, F., & Bruzual, G. 2002, A&A, 381, 524

Wilson, O. C. 1966, ApJ, 144, 695

—. 1976, ApJ, 205, 823

Winn, J. N. 2010, ArXiv e-prints

Winn, J. N., Holman, M. J., Henry, G. W., Roussanova, A., Enya, K., Yoshii, Y., Shporer, A., Mazeh, T., Johnson, J. A., Narita, N., & Suto, Y. 2007, AJ, 133, 1828

Wolszczan, A. & Frail, D. A. 1992, Nature, 355, 145

Wright, J. T., Marcy, G. W., Butler, R. P., & Vogt, S. S. 2004, ApJS, 152, 261

Yang, S. H., Zhang, J., Jin, C. L., Li, L. P., & Duan, H. Y. 2009, A&A, 501, 745

Zboril, M. 2003, Astronomische Nachrichten, 324, 527

Zirin, H. 1988, Astrophysics of the sun (Cambridge University Press)